



UNIVERSITÀ
DEGLI STUDI
DI PADOVA

Università degli Studi di Padova
Dipartimento di Scienze Chimiche

Corso di dottorato di ricerca in:
Scienza e ingegneria dei materiali e delle nanostrutture
Ciclo XXXV

Tuning the phonon contribution to control thermal expansion

Coordinatore: Ch.mo Prof. Giovanni Mattei

Supervisore: Ch.mo Prof. Andrea Sanson

Dottorando : Alessandro Venier

Abstract

Thermal expansion is a ubiquitous phenomenon that represents an issue in engineering design contexts. Even if its control is of paramount importance and has been pursued for a long time, it is still an open problem with only particular solutions, mainly involving composite materials or components with a shape designed to counteract the thermal expansion.

The existence of materials with anomalous thermal expansion properties has been acknowledged long ago; recently it was found that there are compounds with values of the coefficient of thermal expansion with absolute value at least large as those of common metals, but negative in sign. This sparked great scientific interest, leading to the discovery that the coefficient of thermal expansion can radically change when the atoms occupying specific crystal sites are substituted, even going from negative to positive.

An outstanding application of this anomalous behavior could be that of tuning the thermal expansion. This would be achieved by preparing single phase materials with a coefficient of thermal expansion tailored to a particular engineering setting. However, it was also found that the intercalation of small chemical species into certain framework structured compounds turns their thermal expansion from negative to positive or almost zero.

Further, in materials displaying order to disorder phase transitions, a close relationship is observed between the phase transition and anomalous thermal expansion. Other aspects of materials design (e.g. nanostructuration, valence state change) have been found to be relevant in this respect.

It is expected that a variety of microscopic mechanisms are necessary to describe them. In this work we will focus on the vibrational contribution to thermal expansion: EXAFS spectroscopy offers extraordinary insight on the local dynamics of atomic pairs. This is due to the EXAFS sensitivity to the atomic species and to the correlation of the motions of atoms: the former allows to independently study the local neighborhoods of different atoms, while the latter, combined with diffraction measurements, can give information on the anisotropy of thermal vibrations.

We have obtained information on the local dynamics of some analogues of the Prussian blue with brute formula $MM'(CN)_6$. Intercalating these compounds with small chemical species can turn thermal expansion from negative to positive. EXAFS spectroscopy has been employed to ascertain a suppression of the transverse vibrations has been observed upon intercalation, with a predominant role of the vibrations of M-N atomic pairs.

We have also studied a series of zirconium alloys of brute formula Zr_2M ($M=Fe, Co, Ni$) with body tetragonal crystal structure. The relation between the thermal expansion coefficient along the c -axis, with values ranging from largely negative to positive and the anisotropy of thermal expansion of Zr-M atomic pairs; a negative correlation between the anisotropy and both the average atomic volume and the c -axis lattice parameter is found.

EXAFS studies of analogues of copper pyrophosphate $Cu_2P_2O_7$, inexpensive and facile to synthesize, are a challenging subject. Substituting copper with zinc and/or phosphorus with vanadium has striking effects on the crystal structure, on the thermal expansion and on the local dynamics of atomic pairs. Our analysis corroborates the microscopic mechanism of hindering of vibrations transverse to bonds in correspondence to suppression of negative thermal expansion.

Classical molecular dynamics simulations of spherical gold nanoparticles have been performed. Molecular dynamics can study the vibrational dynamics in solids and is thus complementary to EXAFS analysis. The spherical gold nanoparticles of different diameters that have been investigated are simple yet non-trivial systems, a case study of the effect of nanostructuring on the phonon contribution to thermal expansion.

Contents

Introduction	1
List of publications from this PhD thesis	3
Chapter 1: Negative Thermal Expansion	4
1.1 Rigid Unit Modes.....	7
1.2 Classification of NTE materials.....	12
1.2.1 Chemical composition and crystal structure	13
1.2.2 Phase transitions.....	13
1.2.3 Microscopic excitations.....	14
1.3 Tuning thermal expansion	16
Bibliography	19
Chapter 2: Experimental methods	22
2.1 Storage rings and synchrotron light.....	22
2.2 X-ray Absorption Fine Structure	24
2.2.1 The EXAFS equation	26
2.2.2 EXAFS dependence on local vibrational dynamics.....	28
2.3 Sample preparation	29
2.4 Data acquisition	30
2.5 Data analysis procedure.....	31
2.5.1 Preprocessing.....	32
2.5.2 Model building and fitting.....	33
2.6 Results elaboration	34
Bibliography	36
Chapter 3: Local dynamics and intercalation effects in Prussian Blue Analogues	38
3.1 Prussian blue analogues.....	38
3.2 $\text{TiCo}(\text{CN})_6 \cdot 2\text{H}_2\text{O}$	39
3.3 $\text{LuFe}(\text{CN})_6$	44
3.4 Discussion and conclusions.....	47
Bibliography	49
Chapter 4: Thermal expansion and local dynamics of zirconium alloys	51
4.1 Stoichiometric Zr_2M alloys	51
4.2 Zr_2Fe	53
4.3 Zr_2Co	57

4.4 Zr ₂ Ni	61
4.5 Discussion and conclusions.....	64
Bibliography	67
Chapter 5: Chemical substitution and local dynamics of copper pyrophosphate analogues	68
5.1 Copper pyrophosphate analogues.....	68
5.2 Cu ₂ V ₂ O ₇	70
5.3 Cu _{1.25} Zn _{0.75} P ₂ O ₇	75
5.4 Discussion and conclusions.....	78
Bibliography	81
Chapter 6: Nanosize effects on thermal expansion: a molecular dynamics study	82
6.1 EXAFS spectroscopy and molecular dynamics.....	82
6.2 Physical quantities	85
6.3 Test in gold bulk.....	86
6.4 Gold nanoparticles.....	89
6.5 Conclusions	95
Bibliography	96
Conclusions	98

Introduction

Thermal expansion is a ubiquitous phenomenon that represents an issue in engineering design contexts. Even if its control is of paramount importance and has been pursued for a long time, it is still an open problem with only particular solutions, mainly involving composite materials or components with a shape designed to counteract the thermal expansion.

The existence of materials with anomalous thermal expansion properties has been acknowledged long ago with the discovery of the iron-nickel Invar alloy that gained Guillaume a Nobel prize in Physics and which displays a near zero thermal expansion around room temperature. Simple materials as crystalline silicon and germanium show mildly negative thermal expansion (NTE, i.e. contraction with increasing temperature) at cryogenic temperatures and also water contracts with increasing temperature in a narrow range of temperature slightly above its freezing point at atmospheric pressure.

Recently it was found that there are compounds with values of the coefficient of thermal expansion with absolute value at least large as those of common metals (i.e. of order of magnitude $1\text{E-}5\cdot\text{K}^{-1}$), but negative in sign. This sparked great scientific interest, leading to the discovery that the coefficient of thermal expansion can radically change when the atoms occupying specific crystal sites are substituted, even going from negative to positive, encompassing the intermediate values with partial substitution.

An outstanding application of this anomalous behavior could be that of tuning the thermal expansion. This would be achieved by preparing single phase materials with a coefficient of thermal expansion tailored to a particular engineering setting, for example to minimize shocks due to thermal expansion mismatch or to reduce the effect of temperature fluctuations on high precision instrumentation. However, it was also found that the intercalation of small chemical species into certain framework structured compounds turns their thermal expansion from negative to positive or almost zero.

Further, in materials displaying order to disorder phase transitions (e.g. ferroelectric, ferromagnetic) a close relationship is observed between the phase transition and anomalous thermal expansion (e.g. the thermal expansion coefficient behaves normally in the disordered phase). Other aspects of materials design (e.g. nanostructuring, valence state change) have been found to be relevant in this respect.

Given the wide array of compounds displaying these unusual properties, it is expected that a variety of microscopic mechanisms are necessary to describe them. In this work we will focus on the vibrational contribution to thermal expansion: in this regard, EXAFS spectroscopy offers extraordinary insight on the local dynamics of selected atomic pairs. This opportunity stems from the EXAFS sensitivity to the atomic species and to the correlation of the motions of atoms: the former allows to independently study the local neighborhoods of different atoms, while the latter, combined with diffraction measurements, can give information on the anisotropy of thermal vibrations.

This thesis is composed of six chapters, organized as follows: Chapter 1 contains a presentation of the topic of negative thermal expansion the relevant literature and an outline of the main avenues of description and classification of anomalous thermal expansion properties.

Chapter 2 displays a brief but self-contained exposition of EXAFS spectroscopy, the main experimental technique employed in this work, with a focus on the information that it can provide regarding the local dynamics and the vibrational anisotropy of atomic pairs.

After the contextualization of the systems at study and of the experimental technique used to investigate them, the following chapters present the results of this work, which traverse the main routes to tune thermal expansion. The selection of the samples has been performed to study the effect on thermal expansion of intercalation and chemical substitution, in collaboration with the research group of Prof. Jun Chen (Department of Physical Chemistry, University of Science and Technology Beijing), which has provided the samples.

Intercalation of small chemical species in framework structured compounds is the focus of Chapter 3; investigations on the chemical substitution are reported in Chapters 4 and 5; the effect of nanostructuring on thermal expansion is explored in Chapter 6.

Chapter 3 reports on the findings regarding the local dynamics of some analogues of the Prussian blue, that are metal coordination polymers of cyanide displaying important crystal voids. Intercalating these compounds with small chemical species can turn thermal expansion from negative to positive. EXAFS spectroscopy has been employed to ascertain how this modifies the local dynamics of the local atomic neighborhood of the two types of metal atoms present in the compound.

Chapter 4 regards a series of zirconium alloys of brute formula Zr_2M ($M=Fe, Co, Ni$) with body tetragonal crystal structure. The relations between the thermal expansion coefficient along the c -axis, with values ranging from largely negative to positive, the anisotropy of thermal expansion of Zr-M atomic pairs and the average atomic volume are investigated. These zirconium alloys represented

an opportunity to start the study of a novel class of NTE materials with an anisotropic crystal structure.

Chapter 5 presents the EXAFS study of analogues of copper pyrophosphate $\text{Cu}_2\text{P}_2\text{O}_7$, inexpensive and facile to synthesize. Substituting copper with zinc and/or phosphorus with vanadium has striking effects on the crystal structure, on the thermal expansion and on the local dynamics of atomic pairs. In Chapter 6, the last one, the results of classical molecular dynamics simulations of spherical gold nanoparticles of various diameters are reported. Molecular dynamics is particularly well suited to study the vibrational dynamics in solids and is thus complementary to EXAFS analysis in the atomic description of materials vibrations. Spherical gold nanoparticles are simple yet non-trivial systems, a case study of the effect of nanostructuring on the phonon contribution to thermal expansion. A final section follows that summarizes the obtained results, draws conclusions and indicates perspectives of future research.

List of publications from this PhD thesis

1. N. Shi, A. Sanson, A. Venier, L. Fan, C. Sun, X. Xing and J. Chen, Negative and zero thermal expansion in $\alpha\text{-(Cu}_{2-x}\text{Zn}_x\text{)V}_2\text{O}_7$ solid solutions, *Chem. Commun.* (2020). (DOI:10.1039/d0cc04505e)
2. Q. Gao, X. Shi, A. Venier, A. Carnera, Q. Huang, J. Chen, A. Sanson, E. Liang, The Effect of H_2O Molecules on Thermal Expansion of TiCo(CN)_6 , *Inorg. Chem.* **59**, 20, 14852–14855 (2020).
3. N. Shi, A. Sanson, Q. Sun, L. Fan, A. Venier, D. Oliveira de Souza, X. Xing, J. Chen, Strong Negative Thermal Expansion of Cu_2PVO_7 in a Wide Temperature Range, *Chem. Mater.* **33**, 4, 1321–1329 (2021).
4. Q. Gao, Q. Sun, A. Venier, A. Sanson, Q. Huang, Y. Jia, E. Liang, J. Chen, The role of Average Atomic Volume in Predicting Negative Thermal Expansion: the case of REFe(CN)_6 , *Science China Materials* **65**, 553–557 (2022).
5. N. Shi, A. Sanson, A. Venier, L. Fan, Y. Ren, D. Oliveira de Souza, L. Olivi, Y. Song, X. Xing, J. Chen, Tuning Thermal Expansion from Strong Negative to Zero to Positive in $\text{Cu}_{2-x}\text{Zn}_x\text{P}_2\text{O}_7$, *Scripta Materialia*. (DOI: 10.2139/ssrn.3854490)

Chapter 1

Negative Thermal Expansion

Thermal expansion is a ubiquitous phenomenon, the control of which impacts on engineering and materials design and has been the focus of plenty of research. In recent times, the discovery that several compounds display anomalous (i.e. negative in sign and large in magnitude) thermal expansion has given the possibility of tuning the thermal expansion coefficient. However, a lot remains unclear on the various underlying mechanisms responsible for this anomalous property, giving both a scientific challenge and opportunities in the design of materials.

Negative thermal expansion (NTE) is an unusual property of solid materials: contraction is observed with increasing temperature, in contrast with the usual trend for most materials, which expand upon heating (positive thermal expansion, PTE) [1], [2], [3], [4]. An NTE material contracts at least in one direction, but there may be directions along which the material expands, as in the case of PbTiO_3 in its tetragonal phase, for which the c -axis contracts, while the a -axis expands [5]. However, isotropic NTE has been reported, for example in $\text{Zr}_2\text{W}_2\text{O}_8$, a compound with a cubic crystalline structure and NTE from 0.3K to its temperature of decomposition, around 1050K [6], [7]. The physical quantities of relevance to the description of this phenomenon are the coefficients of thermal expansion (CTE), which are in general components of a symmetric rank two tensor, each component representing the corresponding component of strain due to a change in temperature at constant pressure per unit of temperature variation. The trace of this tensor is the volumetric expansion coefficient: these considerations make it especially interesting, both as a relevant quantity in the perspective of applications and as a way to compare the thermal expansion of materials with a different crystal symmetry.

The coefficient of thermal expansion may be defined in slightly different ways, although in most practical cases they don't differ significantly, given the fact that the thermal expansion itself is usually quite small compared to the absolute value of the lengths or volumes: sometimes it is defined as

$$\alpha_{x,T_0} = \frac{1}{x_0} \frac{dx}{dT}(T), \quad (1.1)$$

where x is any of the dimensions (lattice constants in a crystal or volume) of the system and x_0 is the value of the dimension at an arbitrary temperature T_0 , while in a more rigorous sense it is

defined as

$$\alpha_x(T) = \frac{d(\ln(x))}{dT}(T). \quad (1.2)$$

During their usage, most technological components undergo temperature changes that are mostly detrimental to the durability and performance quality of instrumentation: mismatches in thermal expansion of components that are joined or in contact are often associated with thermal shocks, but even in and of itself thermal expansion may lead to dimensional instability and thus to errors intolerable for certain technological precision devices.

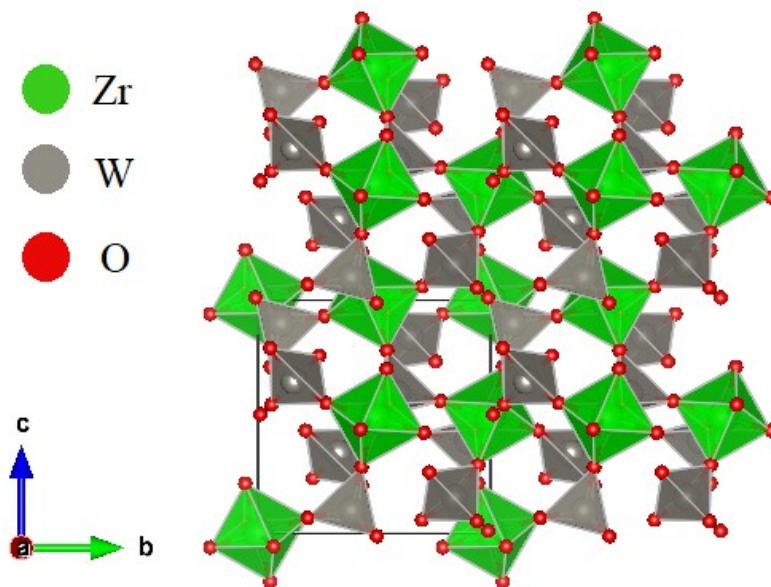


Figure 1.1: Crystal structure of ZrW_2O_8 with the polyhedral quasi-rigid subunits ZrO_6 and WO_4 highlighted. A unit cell is reported in the lower left corner

Many workarounds have been developed to counter these unfavourable effects: particularly shaped components are able to accommodate for thermal expansion (e.g. expansion joints or loops), composite materials (often made of metals with a different thermal expansion coefficient) have widely been employed in devices (e.g. compensated rods to keep under control the swinging period of pendulum clocks) and more sophisticated examples are invented still nowadays as new technologies emerge (e.g. components to keep the focus of infrared optical systems stable against thermal fluctuations).

Another possibility, although recent and less explored, is to build composite systems exploiting the lateral contraction under tension of carefully matched and shaped parts. While these concepts might be useful in many contexts where performance quality and simplicity of design may be less important than other engineering variables, the possibility of having single phase materials with the required thermal properties is nonetheless exciting and promising. A classic case of anomalous thermal expansion is that of the iron-nickel alloys, which (near room temperature) generically display a coefficient of thermal expansion well below that predicted by the law of mixtures. In particular, a minimum is found at a stoichiometry characterized by a 36% Ni atomic content (also known as invar), with a CTE at room temperature an order of magnitude smaller than both those of iron and nickel (and of most usual metals) in their pure form at room temperature. This phenomenon is usually indicated with the term zero thermal expansion (ZTE). Since the discovery of these facts by Guillaume (which earned him the Nobel prize for Physics in 1920) a certain number of applications in horology, land-surveying practices, television technologies (CRT shadow masks) and liquid natural gas transportation have been developed [8]. In the last decades, NTE has been discovered in classes of chemical compounds exhibiting a framework crystal structure [9]. One of the most famous examples is $Zr_2W_2O_8$: being an example of material displaying a large isotropic NTE in a wide temperature range, investigations about it highlighted the important role that a class of vibrational modes (known as rigid unit modes, RUM, or sometimes quasi-rigid unit modes) could play in large NTE (where “large” is intended as “large in absolute value as for usual materials”): this name is due to the fact that these normal modes consist in vibrations in which some subsets of atoms move in a rigid fashion. However, NTE appears also in simpler and more usual materials: silicon and germanium are examples of elemental materials displaying a tetrahedrally coordinated crystal structure which display NTE at cryogenic temperatures, while silver monoxide maintains NTE up to room temperature and beyond [10], [11], [12], [13]. In search of this intriguing property a variety of compounds have been investigated: among these there are oxides [14], fluorides [15], nitrides [16], cyanides [17], [18], metallic alloys [19]; in some of these cases (quasi-)rigid unit modes seem to be absent or to have little to no significance for NTE and, even when they have, their role and the descriptive accuracy of the so-called “tension effect” theory is difficult to fully ascertain. This is true both because not just one or two normal modes contribute to the CTE, but the whole phonon dispersion, and because the

description of lattice dynamics is mostly qualitative or only partially quantitative at the current level of theoretical calculations, even if in some relevant cases reliable and thorough results have been obtained [20], [21], [22], [23].

An important attempt to formulate a theory relating thermal expansion to other experimentally accessible physical quantities and also potentially to a microscopic picture of matter has been due to Grüneisen in the 1920's and may be summarized in the simple and powerful relation:

$$\alpha = \gamma \frac{c_{V,m} \cdot \rho}{k_T}, \quad (1.3)$$

where α is the thermal expansion coefficient, where k_T is the bulk thermal compressibility, $c_{V,m}$ is the specific heat per unit mass at constant volume, ρ is the density of the material and γ is the Grüneisen parameter, which for many simple solids (e.g. elemental metals) is weakly dependent on temperature and can be approximately considered an intrinsic property of the material [24].

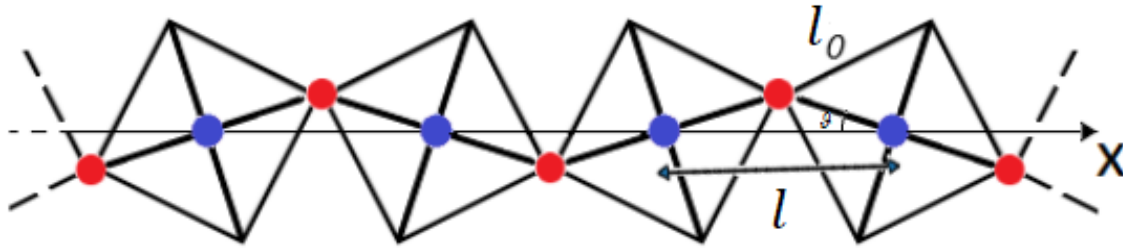


Figure 1.2: Conceptual description of a framework structured chain of atoms. The polygons are reported to hint at a framework structure in the other directions.

1.1 Rigid Unit Modes

As mentioned before, RUMs are an important building block of models describing NTE in a wide array of materials. The underlying physical principles may be based on observation of a simple model, that of a periodically repeating chain of atoms linked rigidly, which is represented in Figure 1.2, where red and blue circles represent different atomic species. Extending this structure by cubic symmetry about the blue sites, a perovskite type crystal is obtained, as ScF_3 and ReO_3 . Let us consider the case in which the “blue” atoms may slide along the crystal axis, but with their vertical coordinates fixed, “red” atoms instead are constrained to move along the vertical direction and, furthermore, the nearest neighbors’ distance (l_0) between the blue and red atoms is constant and is referred to as the bond length. Defining θ the angle of the vector difference of the positions of nearest neighbors red

and blue atoms with the crystal axis X, we have that the distance between two nearest blue atoms is $l(\theta) = 2l_0 \cos(\theta)$.

The relevant quantity for our discussion is the lattice constant which in this case is the distance between the equilibrium positions of two nearest blue atoms, i.e. the thermal average $\langle l \rangle_T$. Here the thermal average is intended as

$$\langle l \rangle_T = \int d\theta l(\theta) e^{-\beta E(\theta)} / \int d\theta e^{-\beta E(\theta)}, \quad (1.4)$$

with $\beta = 1/(k_B T)$, k_B the usual Boltzmann's constant and $E(\vartheta)$ a deformation potential energy, i.e. the energy required to deform the equilibrium configuration(s) into the configuration with angle θ [25], .

Considering the particular case of small fluctuations around an equilibrium configuration at $\theta = 0$, the potential energy due to this normal mode may be approximated as $E(\theta) \approx b\theta^2/2$, $k > 0$ and $\cos(\theta) \approx 1 - \theta^2/2$. With these assumptions one obtains the relation [26]:

$$b\langle \theta^2 \rangle_T / 2 = k_B T / 2. \quad (1.5)$$

This implies that, at least at low enough temperatures, the coefficient of thermal expansion is negative and also that it doesn't depend on third order force constants, as instead is usual for stretching modes.

In the case in which the potential displays a minimum at $\theta_0 \neq 0$, for low enough temperatures the expression of the thermal expansion can again be significantly simplified obtaining ($\delta l := l - 2l_0 \cos(\theta_0)$):

$$\begin{aligned} \langle \delta l \rangle_{lowT} &= \int_{\mathbb{R}} d\theta 2l_0 \cos(\theta) \cdot e^{-\beta E(\theta)} / \int_{\mathbb{R}} d\theta e^{-\beta E(\theta)} \\ &\approx 2l_0 \left(E'''(\theta_0) \cdot \sin(\theta_0) - \frac{\cos(\theta_0)}{2E''(\theta_0)} \right) k_B T \end{aligned} \quad (1.6)$$

Thus, in the case of phase transitions related to flexural instabilities it can be expected the CTE to change sign between the phases. A particular case is the one in which $E(\theta) = b \cdot \theta^2 + c \cdot \theta^4$, $b < 0, c > 0$. The sign of the thermal expansion is independent from which side the flexural instability occurs (i.e. it is invariant by inversion $\theta_0 \rightarrow -\theta_0$). Also, in the limit $\theta_0 \rightarrow 0$ the previous case is recovered.

In the particular instance in which $b = 0$, the potential is the quartic one $E(\theta) = c \cdot \theta^4$, which, always in the low temperature regime, yields:

$$\langle \delta l \rangle_{lowT} \approx -(\beta c)^{-1/2} \int_{\mathbb{R}} d\theta l_0 (\beta c)^{1/2} \theta^2 \cdot e^{-\beta c \theta^4} / \int_{\mathbb{R}} d\theta e^{-\beta c \theta^4} \quad (1.7)$$

thus,

$$\langle \delta l \rangle_{lowT} = -S \cdot l_0 \frac{(k_B T)^{1/2}}{c^{1/2}} \Rightarrow \alpha_{lowT} = -S \frac{k_B^{1/2}}{2T^{1/2} c^{1/2}}, \quad (1.8)$$

with S a (positive) numeric constant that can be found comparing Eqs. (1.7) and (1.8). This case is interesting due to the divergence of the thermal expansion coefficient for $T \rightarrow 0^+$, which might be of interest in the description of systems near a structural phase transition. Even if quantum effects (which will make the CTE go to zero for $T \rightarrow 0^+$) have to be considered to properly describe the thermal properties at very low temperatures, the negative thermal expansion is expected to be enhanced at low temperatures.

A more thorough and rigorous analysis that doesn't assume anything on the angular range of the fluctuations might be performed considering the fact that the linear thermal expansion coefficient sign is the same of $\frac{d\langle l \rangle_T}{dT}$, which is the same of

$$\int d\theta E(\theta) \cos(\theta) e^{-\beta E(\theta)} \cdot \int d\theta e^{-\beta E(\theta)} - \int d\theta \cos(\theta) e^{-\beta E(\theta)} \cdot \int d\theta E(\theta) e^{-\beta E(\theta)} \quad (1.9)$$

In the case $E(\theta) = \alpha \theta^2, \alpha > 0$ with the approximation $\cos(\theta) \approx 1 - \theta^2/2$ the sign of the thermal expansion is that of the quantity

$$\left[- \int d\theta \theta^4 e^{-\beta \alpha \theta^2} \cdot \int d\theta e^{-\beta \alpha \theta^2} + \left(\int d\theta \theta^2 e^{-\beta \alpha \theta^2} \right)^2 \right] \quad (1.10)$$

which is negative due to the Cauchy-Schwarz inequality, applied to the functions $e^{-\beta \alpha \theta^2/2}$ and $\theta^2 e^{-\beta \alpha \theta^2/2}$.

More generally, the quantity in Eq. ((1.9) is negative if $E(\theta)$ is taken symmetric with respect to $\theta = 0$, increasing for positive values of θ and temperature is low enough to guarantee that $E(\theta) e^{-\beta E(\theta)}$ is an increasing function for all angle values, as can be seen considering the following inequalities:

$$\begin{aligned} & \int d\theta E(\theta) \cos(\theta) e^{-\beta E(\theta)} \cdot \int d\theta e^{-\beta E(\theta)} \\ & \leq \left(\int d\theta E(\theta) e^{-\beta E(\theta)} \cdot \int d\theta \cos(\theta) \cdot \int d\theta e^{-\beta E(\theta)} \right) / \Delta\theta \\ & \leq \int d\theta E(\theta) e^{-\beta E(\theta)} \cdot \int d\theta \cos(\theta) e^{-\beta E(\theta)}, \end{aligned} \quad (1.11)$$

where $\Delta\theta$ is the angle range width and the inequalities are particular cases of the integral Chebyshev inequality, which requires that $E(\theta)$ is positive and increasing for positive values of θ .

These models, clearly strong simplifications, lack several aspects which are necessary for description of real materials: a realistic model must account for the fact that the normal modes usually aren't RUMs and thus there are contributions due to bond stretching, it must incorporate quantum effects (especially at very low temperatures); also, the lattice motion occurs in three dimensions.

A simple toy model follows that illustrates what happens if the rigidity constraint is removed: the situation of Figure 1.2 immediately becomes complicated by the presence of the phonon dispersion, but the main results are formally correct even when treating the lattice dynamics in a very simplified way, i.e. considering atomic pairs bound to their lattice sites, but with vibrations decoupled from each other. The deformation energy of a nearest neighbours' atomic pair is expanded up to third order in the deformations, removing the rigidity constraint, i.e. adding the possibility of stretching the bonds between nearest neighbour atoms:

$$E(\epsilon_{\parallel}, \epsilon_{\perp}) \approx k_{\parallel} \epsilon_{\parallel}^2 / 2 + k_{\perp} \epsilon_{\perp}^2 / 2 + \mu \epsilon_{\parallel}^3 + \eta \epsilon_{\parallel} \epsilon_{\perp}^2 \quad (1.12)$$

with ϵ_{\parallel} the stretching deformation of the bond length, that satisfies

$$\epsilon_{\parallel}^2 \approx x^2 + x \epsilon_{\perp}^2 / l_0 + x^3 / l_0, \quad (1.13)$$

while $y := \epsilon_{\perp}$ is the relative vertical displacement of the red and blue type atoms, l_0 is the equilibrium bond length and x is the relative displacement of nearest neighboring atoms projected along the equilibrium lattice direction, while y is the vertical displacement of the red atom. The k_{\parallel} and k_{\perp} quantities have a role similar to that of effective force constants, although this nomenclature is to be understood as only indicative. The absence of terms linear and cubic in ϵ_{\perp} is justified by the symmetry of the system upon the inversion $\epsilon_{\perp} \rightarrow -\epsilon_{\perp}$. In this case the thermal expansion of a nearest neighbors' atomic pair is, at first order in the temperature T :

$$\begin{aligned} \langle x \rangle_{T, lowT} &\approx \frac{\int_{\mathbb{R}^2} dx dy \frac{\left(\tilde{\mu} x^4 + \eta x^2 y^2 + \frac{k_{\parallel} x^2 y^2}{2l_0} \right)}{k_B T} e^{-\beta(k_{\parallel} x^2 + k_{\perp} y^2)/2}}{\int_{\mathbb{R}^2} dx dy e^{-\beta(k_{\parallel} x^2 + k_{\perp} y^2)/2}} \\ &= -\left(\left(\frac{3\tilde{\mu}}{k_{\parallel}} + \frac{\eta}{k_{\perp}} \right) \frac{1}{k_{\parallel}} + \frac{1}{2l_0 k_{\perp}} \right) k_B T, \end{aligned} \quad (1.14)$$

with $\tilde{\mu} = \mu + \frac{k_{\parallel}}{2l_0}$. A flexural instability analogous to buckling arises upon application of a pressure high enough: informally speaking, if ϵ_{\parallel} is negative enough, i.e. if the bond is shrunk enough, the effective transverse frequency becomes imaginary and a crystal structure transition occurs. In that case, the calculation follows the one made in the case of asymmetric equilibrium state seen before.

The extreme case of rigid unit motions is obtained by taking the limit $k_{\parallel} \rightarrow +\infty$. We see that what controls the sign of the thermal expansion is in fact the ratio between the longitudinal and transverse force constants, as can be checked inspecting the sign of the expression in Eq. (1.14) when $\mu < 0$, as generically is.

Although this calculation exemplifies how the tension effect arises from atomic motions, it must be generalized to describe the lattice dynamics correctly, also considering its three-dimensional nature: a complete treatment is obtained by formulating the relative displacements in terms of normal modes and correctly representing the total deformation potential energy of the lattice. For the RUMs seen before b can be expressed as $I\omega_{\text{RUM}}^2$ in Eq. (1.5), where I is the moment of inertia of the Rigid Unit along the axis about which it rotates in the RUM.

We can outline the strategy when considering the complete dispersion of lattice vibrations, also all those with no particular longitudinal or transverse characteristic. As a starting point, the deformation energy might be expanded to third order in deformations of atomic pairs; the deformations can then be further expressed in terms of the displacements, giving rise, among others, to the same type of third order terms (giving negative contributions to the CTE) seen before. The lattice thermal expansion will be expressed as the thermal average of a suitable sum of those displacements and the calculations that follow are analogous to those presented above.

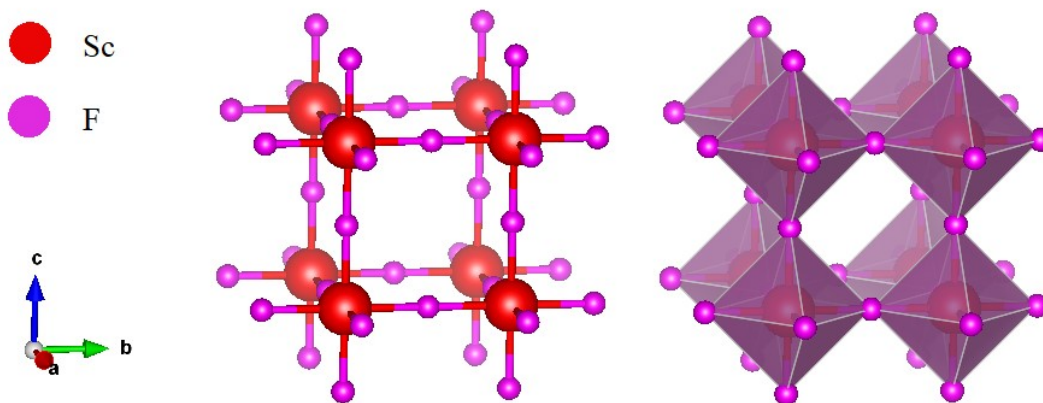


Figure 1.3: Crystal structure of ScF_3 both presented as a ball and stick model (left) and with the polyhedral quasi-rigid subunits highlighted (right).

As for the importance of quantum effects, it is usually well estimated by considering the ratios $h\nu/k_B T$ for the various frequencies ν , where h is the Planck constant: if the ratio is small enough the classical model can be reliably employed, as the states might be considered equipartitioned. The

main quantum effect is that, in accordance with the third law of thermodynamics, the thermal expansion coefficient tends to zero at $T \rightarrow 0^+$.

The integral averages must be changed into traces over a basis of states: using the virial theorem we obtain

$$\frac{\langle \theta^2 \rangle}{2} = \frac{\langle E \rangle}{2\alpha} = \frac{\hbar\nu}{2\alpha} \left(\frac{1}{2} + \frac{1}{e^{\hbar\nu/k_B T} - 1} \right), \quad (1.15)$$

which leads to a zero CTE at $T = 0K$ and the correct classical limit $\frac{\langle \theta^2 \rangle}{2} \approx \frac{k_B T}{2\alpha}$ at high T. Considering the case of ScF_3 , for which the M -mode ($\vec{k} = [0.5, 0.5, 0]$) has energy 2.8 meV at $T = 0K$ [27], corresponding to an effective temperature of around $30K$, so in this case due to the “softness” of the RUMs the non-quantum models are reliable even at temperatures significantly lower than room temperature. This whole analysis highlights two points: symmetry plays a crucial role in the NTE due to phonons, as evidenced by the simple cases of RUMs with symmetric and non-symmetric equilibrium, and harmonic properties of materials (i.e. second order force constants) are not only crucial to vibrational NTE, but also useful in the assessment of the potentiality of selected materials as NTE materials candidates. Indeed, the first fact is enough to understand why large or even giant NTE are so uncommon phenomena among materials even if, as we have briefly mentioned, contributions to thermal expansion due to the tension effect are commonly present [25], [28]; the second fact significantly simplifies the theoretical efforts to direct the search for these anomalous property: going back to the case of ScF_3 , we can estimate how negative the CTE would get if the M mode was the only mode present, $\alpha_{linear, RUM} \approx -k_B / (8I\pi^2\nu_M^2) \approx -73 \text{ ppm} \cdot K^{-1}$ with I the moment of inertia of the ScF_6 octahedra along one of the three axes passing through collinear F-Sc-F atoms, to be compared with an experimental minimum of approximately $-10 \text{ ppm} \cdot K^{-1}$. The discrepancy is due to the fact that all normal modes contribute (positively or negatively) to the thermal expansion.

1.2 Classification of NTE materials

Simplified models allow to intuitively understand specific significative aspects, but to develop a better understanding of any physical property it is also necessary to have a broader view at what types of materials exhibit it and to what extent.

1.2.1 Chemical composition and crystal structure

A first practical way to categorize NTE materials is by their chemical composition: observation of patterns and relationships in particular classes of compounds sharing chemical strong chemical similarities has proven fruitful to the understanding of the basic mechanisms underlying this phenomenon. Also, as we have seen in the previous section, crystal structure plays an important role. The two aspects are often intertwined: for example, studying tetrahedrally coordinated compounds, it has been observed the fact that the CTE is negatively correlated with the ionicity of the compound [29], [30]; a similar observation has been deduced from the study of cyanides and this gives precious insights regarding assessment of NTE in candidate materials [31].

1.2.2 Phase transitions

Another approach starts from the phase diagram of materials: in relevant instances of NTE materials radical changes in the CTE might be observed in different phases of the system. Coming back to the $\text{Fe}_{64}\text{Ni}_{36}$ alloy, which is ferromagnetic (FM), it was observed already by Guillaume that the anomalous thermal behavior only appears at temperatures below the Curie temperature of the alloy. This isn't an isolated case and this radical change is observed also in other invar alloys (e.g. iron-platinum alloys and iron-chromium alloys) at the magnetic ordering phase transition. The important case of PbTiO_3 has already been mentioned: upon transition from the tetragonal ferroelectric phase to the cubic (non-ferroelectric) phase the anisotropic NTE disappears. It has been observed that a positive correlation exists between the square of the spontaneous polarization of NTE ferroelectrics and the anomalous contributions to the CTE, quantified by means of the spontaneous electrostriction parameter $\omega_s = \frac{V_f - V_n}{V_n}$, where V_f and V_n are respectively the volumes of the system in the ferroelectric state and extrapolated from the paraelectric phase. An analogous relationship is available for magnetic alloys with anomalous CTE, with the figure of merit being the spontaneous magnetostriction [32].

We can go a little further in exploring this theoretical framework by introducing in it Ginzburg-Landau theories of critical phenomena, which can be very useful as a starting point of description of phase transitions: the free energy of the system in the vicinity of the critical point of the transition is expanded in powers of the order parameter in accordance with the group of symmetries of the system.

For a system symmetric upon inversion of the order parameter the Landau free energy near the critical point is approximately of the form:

$$F(T, O, e) = A(T) + B \cdot (T - T_c)O^2 + CO^4 + De^2/2 - EeO^2, \quad (1.16)$$

where e is the spontaneous strain with respect to the disordered/normal phase, T_c is the critical temperature and B, C, D and E are quantities that don't depend on temperature, on O nor on e (B, C, D are positive). Important example of quantities employable as O in this scheme are the modulus of the magnetization for ferromagnets, the modulus of the polarization for ferroelectrics, and the modulus of the complex $\Psi O(1)$ order parameter for superconductors [33]. The spontaneous strain introduced here is indeed a generalization of the ones defined when describing the ferroelectric and ferromagnetic cases. Minimizing the free energy with respect to the strain gives an interesting quadratic relation between the spontaneous strain and the order parameter, i.e. $e = (E/D)O^2$ [34], as is observed in the available experimental data.

1.2.3 Microscopic excitations

Observing that the aforementioned mechanisms underlying NTE are strongly tied to a kind of microscopic excitations allows to introduce another possible classification of NTE materials. In fact, in many NTE materials one type of excitations gives the greatest contribution and, even in the cases of multiple sources of NTE, understanding the roles and interplay of the excitations is crucial. In addition to the already mentioned structural thermal disorder related to soft phonons and the excitations arising in long-range ordered ferroelectric or magnetic phases, also variations of the electronic structure may induce a change in sign of the CTE: changes in atomic valence with temperature, charge carrier doping in semiconductors and electron confinement in metal nanoparticles may also lead to NTE or its enhancement.

In general, the problem of relating thermal expansion to microscopic quantities may be framed in the context of thermodynamics and statistical mechanics starting from the following fundamental relationships:

$$\alpha_V = \frac{1}{V} \frac{\partial V}{\partial T} \Big|_P = k_T \frac{\partial P}{\partial T} \Big|_V = -k_T \frac{\partial^2 A}{\partial V \partial T}, \quad 1.17$$

where A is the free energy and k_T is the isothermal bulk compressibility.

The Grüneisen theory follows by using the quasi-harmonic approximation (QHA), obtaining in the end a formula specifying the contributions from single normal modes:

$$\frac{1}{k_T \cdot V} \sum_i \gamma_i c_{V,i} = \gamma \frac{c_V}{k_T \cdot V}, \quad (1.18)$$

defining $\gamma_i = -\frac{V}{\omega_i} \frac{\partial \omega_i}{\partial V}$ to be the Grüneisen parameter relative to the i -th normal mode,

$$c_{V,i} = k_B \left(\frac{\hbar \omega_i}{k_B T} \right)^2 \frac{\exp(-\hbar \omega_i / k_B T)}{(1 - \exp(-\hbar \omega_i / k_B T))^2} \quad (1.19)$$

is the contribution to the specific heat capacity at constant volume of the i -th normal mode and V the specific volume. The normal modes are specified by a wavevector (that for crystals belongs to the first Brillouin zone) and a phonon band index.

Due to the ubiquitous nature of phonons in solids, the QHA is the theoretical framework from which to start the analysis of lattice dynamics and its contributions to thermodynamically relevant quantities (e.g. free energy, specific heat, CTE) in a way capable of describing properties intrinsically related to the anharmonicity of the interatomic potential energy. In fact, as a simple corollary of this description of thermal expansion, we see that in harmonic crystals the thermal expansion is exactly zero.

We can see from this that if the bulk modulus and the (average) Grüneisen parameter weakly depended on the temperature, the thermal expansion would approximately have the same trend in temperature of the heat capacity at constant volume. However, it must be noted that while this might be a good approximation for many simple materials, for example solid bulk copper or gold, it is not for many NTE compounds for which the full phonon dispersion must be considered, especially given the fact that in interesting cases (e.g. ScF_3 , ZrW_2O_8) the negative contributions come mainly from limited regions of the first Brillouin zone. In particular, in the neighborhood of high-symmetry k -points low energy modes (usually quasi-RUMs) have been found to be endowed with a large negative Grüneisen parameter. Limitations of the QHA are easy to point out and are mainly related to the fact that in QHA anharmonicity is accounted for only at the implicit level, i.e. the normal mode frequencies are assumed to depend only on structural parameters (e.g. specific volume, lattice constants) and not on temperature or other state variables.

In order to develop particular considerations from the general theoretical starting points, different strategies are deployed to calculate the various contributions to free energy and then derive the

thermal expansion along with all the relevant thermal quantities. An approach is to calculate the energy contributions only from certain types of microscopic excitations (for example phonons), keeping fixed the degrees of freedom related to the others (for example keeping the electrons in the ground state or imposing a value of the magnetization). In mathematical terms (O stands for the considered degrees of freedom, e.g. magnetization or polarization):

$$\frac{dV}{dT} = \left. \frac{\partial V}{\partial T} \right|_O + \frac{\partial V}{\partial O} \cdot \frac{\partial O}{\partial T} \quad (1.20)$$

If $\partial O / \partial T < 0$ (as usually is the case for ferromagnets and ferroelectrics, in which O may be respectively taken as the magnetization or the polarization), the sign of the second term is determined by the sign of $\partial V / \partial O$, which in the case of ferromagnetism is the magnetostriction. After completion of the necessary calculations, it is possible to estimate the difference between the computed result and the experimental data, thus making the necessity of including particular excitations clear; it is also possible to try to repeat the operation with different degrees of freedom fixed and then combining the results to obtain a more realistic description [35], [36].

1.3 Tuning thermal expansion

A better understanding of the mechanisms behind NTE in some relevant cases (e.g. ScF_3 , ZrW_2O_8), paved the way to new methods to tune the thermal expansion, in the sense of producing materials with CTE determined by design (in a reasonable range of values).

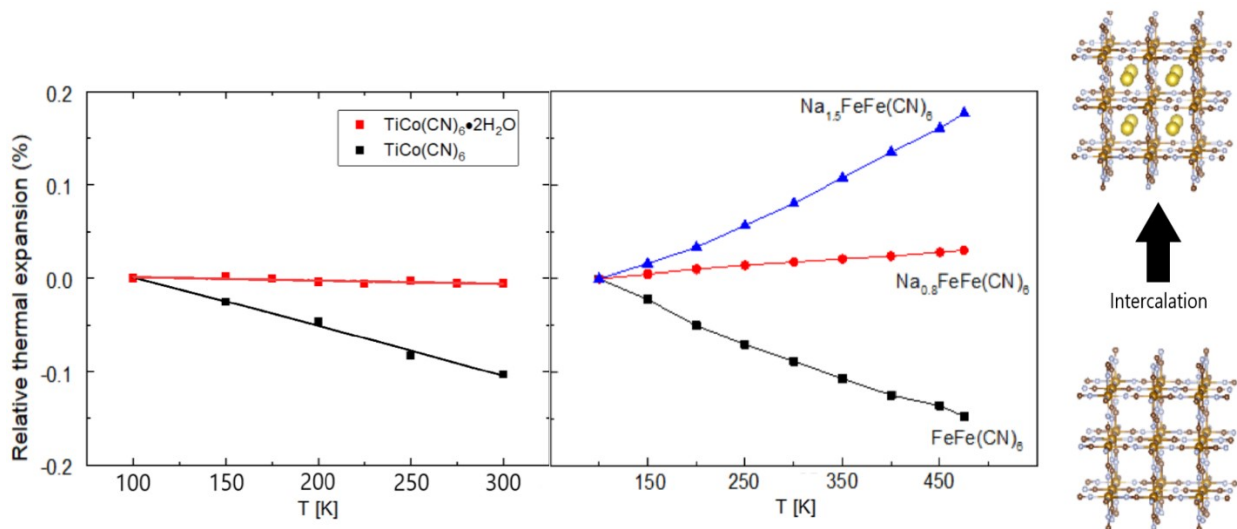


Figure 1.4: Examples of effect of intercalation of water molecules (left) and alkaline ions (right) on thermal expansion in framework structured compounds (Data acquired by the research group of Prof. Jun Chen)

This provides a way of exploiting this exotic behavior of matter. Up to now, three main processes have been developed to obtain materials with a specific CTE: intercalation of small species, chemical substitution and nano-structuration.

Intercalation of framework structured materials with small species can be performed by electrochemical means. The CTE of framework structured compounds that display significant voids in their structure increases as these are filled with small chemical species, such as alkaline ions or water molecules. According to the analysis in the previous chapter, the hindrance of RUMs due to the presence of the intercalated species is a plausible candidate for this mechanism of NTE suppression. However, a lot remains to be understood about this method, especially regarding the specific roles of the various atoms in the framework structures and how the intercalated species interfere with the lattice dynamics. Compounds with similar crystal structure and chemical composition, as mentioned before, can display a CTE different from the pure versions of the compounds: this has been highlighted by studies involving families of compounds mainly differing by the stoichiometry of elements occupying specific lattice sites. An example among framework structured compounds is the family of compounds $Zr_{1-x}Sn_xMoO_8$, which displays NTE or PTE depending on the value of x [37]. This approach allows to systematically tune the thermal expansion coefficient in between the extreme values. However, the substitution of atomic species with others is a process significantly more invasive than intercalation and can cause changes to the materials that are in general more difficult to predict and control, from the distortion of the local structure to crystal structure transitions.

The third process that can radically change the thermal expansion of a material is nano-structuration: it is well-known that materials with nanometric dimensions can display different properties than their bulk correspondent and they usually do [38]. In various cases (e.g. Au, CuO, MnF₂, ScF₃ and PbTiO₃) the thermal expansion coefficient of the nanoparticles strongly depends on the particle size, to the point of changing sign with respect to the bulk value with sufficiently small size [39]. This phenomenon is often accompanied by (local) phase transitions (ScF₃ and PbTiO₃) and/or by a peculiar magnetic structure, both of which are very hard to fully understand [40], [41], [42]. Magnetic nanoparticles present important case studies in which the interplay between different mechanisms

might give non-negligible contributions to the thermal expansion. Applications of this phenomenon may be found for nanoparticles embedded in particular matrices [43].

Among the great quantity of information collected up to now, those regarding the relation between thermal expansion and simpler properties of materials are especially relevant to further improve thermal expansion control. For example, the specific volume per atom (closely related to the concept of average atomic volume, AAV) of the crystal structure, the ionic radius of particular atoms and the anisotropy of thermal vibrations have been found to be negatively correlated to the coefficient of thermal expansion in several cases [44], [45].

As for the potentiality of these approaches, the lines of research are various: on one side it is interesting to fully explore the classes of materials where NTE has been found, because, while many of the materials found up to now are not widely employable in technological applications, exploiting the acquired knowledge it might be possible to find materials more favourable to applications, for example displaying chemical stability and good mechanical and/or chemical resistance with an affordable production cost. On the other side the thermal expansion control strategies are interesting. In fact, it is important to have results on the efficacy of the procedures for thermal expansion control that are as complete as possible. Thus, a variety of relatively simple compounds are required to be thoroughly investigated.

At this point it must be clear that in general the question of whether and how much the negative contributions to thermal expansion are caused by one mechanism or another is hard to answer, but also interesting, both from the scientific and applicative point of view.

Bibliography

- [1] J. S. O. Evans, "Negative thermal expansion materials," *J. Chem. Soc., Dalton Trans.*, p. 3317–3326, 1999.
- [2] J. Chen, L. Hu, J. Deng and X. Xing, "Negative thermal expansion in functional materials: controllable thermal expansion by chemical modifications," *Chem. Soc. Rev.*, vol. 44, p. 3522, 2015.
- [3] G. Barrera et al., "Negative thermal expansion," *J. Phys.: Condens. Matter*, no. 17, p. R217.
- [4] M. Blackman, "On the thermal expansion of solids," *Proc. Phys. Soc. B*, vol. 70, p. 827, 1957.
- [5] G. Rossetti et al., *J. Mater. Res.*, no. 13, p. 3197, 1998.
- [6] J. S. O. Evans et al., "Structural investigation of the negative-thermal-expansion material ZrW₂O₈," *Acta Cryst.*, vol. B55, pp. 333-340, 1999.
- [7] T. A. Mary et al., "Negative Thermal Expansion from 0.3 to 1050 Kelvin in ZrW₂O₈," *Science*, vol. 272, no. 5258, pp. 90-92, 1996.
- [8] C. E. Guillaume, "Invar and its applications," *Nature*, vol. 71, no. 1832, pp. 135-139, 1904.
- [9] A. L. Goodwin et al., "Colossal Positive and Negative Thermal Expansion in the Framework Material Ag₃[Co(CN)₆]," *Science*, vol. 319, no. 5864, pp. 794-797, 2008.
- [10] R. Carr et al., "Thermal expansion of germanium and silicon at low temperatures," *Philosophical Magazine*, pp. 157-163, 1964.
- [11] K. G. Lyon et al., "Linear thermal expansion measurements on silicon from 6 to 340 K," *J. Appl. Phys.*, vol. 48, p. 865, 1977.
- [12] W. Tiano et al., "Thermal expansion in cuprite-type structures from 10K to decomposition temperature: Cu₂O and Ag₂O," *J. Appl. Cryst.*, vol. 36, pp. 1461-1463, 2003.
- [13] P. Fornasini et al., "Bond compressibility and bond Grüneisen parameters of CdTe," *Journal of Physics: Condensed Matter*, vol. 30, no. 24, p. 245402, 2018.
- [14] M. Dapiaggi and A. Fitch, "Negative (and very low) thermal expansion in ReO₃ from 5 to 300 K," *J. Appl. Cryst.*, vol. 42, pp. 253-258, 2009.
- [15] B. Greve et al., "Pronounced Negative Thermal Expansion from a Simple Structure: Cubic ScF₃," *J. Am. Chem. Soc.*, vol. 132, no. 44, pp. 15496-15498, 2010.
- [16] K. Takenaka and H. Takagi, "Giant negative thermal expansion in Ge-doped anti-perovskite manganese nitrides," *Appl. Phys. Lett.*, vol. 87, p. 261902, 2005.
- [17] K. W. Chapman et al., "Compositional Dependence of Negative Thermal Expansion in the Prussian Blue Analogues MIIIPtIV(CN)₆ (M = Mn, Fe, Co, Ni, Cu, Zn, Cd)," *J. Am. Chem. Soc.*, vol. 128, no. 21, pp. 7009-7014, 2006.

- [18] S. Margadonna et al., "Zero Thermal Expansion in a Prussian Blue Analogue," *J. Am. Chem. Soc.*, vol. 126, no. 47, pp. 15390-15391, 2004.
- [19] Y. Muraoka et al., "Magnetovolume effects in $Zr-(Fe_{1-x}Co_x)_2$," *J. Phys. F: Met. Phys.* 10 127, 1980.
- [20] N. Wang et al., "Phonon spectrum attributes for the negative thermal expansion of $MZrF_6$ ($M = Ca, Mn-Ni, Zn$)," *Inorg. Chem. Front.*, vol. 6, p. 1022, 2019.
- [21] M. Zhang et al., "Negative thermal expansion in NbF_3 and $NbOF_2$: a comparative theoretical study," *Chin. Phys. B*, vol. 30, no. 5, p. 056501, 2021.
- [22] Y. Liu et al., "Negative thermal expansion in isostructural cubic ReO_3 and ScF_3 : A comparative study," *Computational Materials Science*, vol. 107, pp. 157-162, 2015.
- [23] U. D. Wdowik et al., "Lattice dynamics of rhenium trioxide from the quasiharmonic approximation," *PHYSICAL REVIEW B*, vol. 82, p. 104301, 2010.
- [24] E. Gruneisen, "Theorie des festen Zustandes einatomiger Elemente," *Annalen der Physik*, vol. 344, no. 12, pp. 257-306, 1912.
- [25] A. Sanson, "On the switching between negative and positive thermal expansion in framework materials," *Materials Research Letters*, vol. 7:10, pp. 412-417, 2019.
- [26] V. Heine et al., "Geometrical origin and theory of negative thermal expansion in framework structures," *J. Am. Ceram. Soc.*, vol. 82, no. 7, pp. 1793-1802, 1999.
- [27] T. Chatterji et al., "Pressure- and temperature-induced M_3 phonon softening in ReO_3 ," *Phys. Rev. B*, vol. 79, p. 184302, 2009.
- [28] M. T. Dove and H. Fang, "Negative thermal expansion and associated anomalous physical properties: review of the lattice dynamics theoretical foundation," *Rep. Prog. Phys.*, vol. 79, p. 066503, 2016.
- [29] J. C. Phillips, "Ionicity of the Chemical Bond in Crystals," *Rev. Mod. Phys.*, vol. 42, p. 317, 1970.
- [30] P. Fornasini et al., "Nearest-neighbour distribution of distances in crystals from extended X-ray absorption fine structure," *J. Chem. Phys.*, vol. 147, p. 044503, 2017.
- [31] Y. Li et al., "Effect of bond on negative thermal expansion of Prussian blue analogues $MCo(CN)_6$ ($M = Fe, Ti$ and Sc): a first-principles study," *J. Phys. Condens. Matter*, vol. 32(45), p. 455703, 2020.
- [32] J. Chen et al., "The Role of Spontaneous Polarization in the Negative Thermal Expansion of Tetragonal $PbTiO_3$ -Based Compounds," *J. Am. Chem. Soc.*, vol. 133, p. 11114-11117, 2011.
- [33] H. Yamada, "Pressure effect in an itinerant-electron metamagnet at finite temperature," *J. Magn. Magn. Mat.*, vol. 139, pp. 162-170, 1995.
- [34] H. Fujishita et al., "X-ray diffraction study of spontaneous strain in Fe-pnictide superconductor, $NdFeAsO_{0.89}F_{0.11}$," *The European Physical Journal B*, vol. 85, 2012.

- [35] S. Khmelevskiy, I. Turek and P. Mohn, "Large Negative Magnetic Contribution to the Thermal Expansion in Iron-Platinum Alloys: Quantitative Theory of the Invar Effect," *Phys. Rev. Lett.*, vol. 91, no. 3, p. 037201, 2003.
- [36] S. Khmelevskiy and P. Mohn, "Magnetostriction in Fe-based alloys and the origin of the Invar anomaly," *Phys. Rev. B*, vol. 69, p. 140404, 2004.
- [37] S. E. Tallentire et al., "Systematic and Controllable Negative, Zero, and Positive Thermal Expansion in Cubic $Zr_{1-x}Sn_xMo_2O_8$," *J. Am. Chem. Soc.*, vol. 135, no. 34, p. 12849–12856, 2013.
- [38] W. P. Halperin, "Quantum size effects in metal particles," *Rev. Mod. Phys.*, vol. 58, p. 533, 1986.
- [39] W.-H. Li et al., "Thermal Contraction of Au Nanoparticles," *Phys. Rev. Lett.*, vol. 89, p. 135504, 2002.
- [40] L. Hu et al., "Localized Symmetry Breaking for Tuning Thermal Expansion in ScF_3 Nanoscale Frameworks," *J. Am. Chem. Soc.*, vol. 140, no. 13, pp. 4477-4480, 2018.
- [41] X. G. Zheng et al., "Giant negative thermal expansion in magnetic nanocrystals," *Nature Nanotechnology*, vol. 3, pp. 724-726, 2008.
- [42] A. L. Goodwin, "The ins and outs of thermal expansion," *Nature Nanotechnology*, vol. 3, pp. 711-712, 2008.
- [43] J. Ba et al., "C/SiC composite-Ti6Al4V joints brazed with negative thermal expansion ZrP_2WO_{12} nanoparticle reinforced AgCu alloy," *Journal of the European Ceramic Society* 39, pp. 755-761, 2019.
- [44] K. W. Chapman et al., "Compositional Dependence of Negative Thermal Expansion in the Prussian Blue Analogues $MIIIPtIV(CN)_6$ ($M = Mn, Fe, Co, Ni, Cu, Zn, Cd$)," *J. Am. Chem. Soc.*, vol. 128, no. 21, pp. 7009-7014, 2006.
- [45] Q. Gao et al., "Discovering Large Isotropic Negative Thermal Expansion in Framework Compound $AgB(CN)_4$ via the Concept of Average Atomic Volume," *J. Am. Chem. Soc.*, vol. 142, no. 15, p. 6935–6939, 2020.

Chapter 2

Experimental methods

The EXAFS spectroscopy is a technique which allows to investigate the local vibrational dynamics of materials at the atomic scale. It is the main focus of this work to use the experimental data from this technique to inquire materials displaying anomalous thermal expansion. Thus, in this chapter the technique is briefly presented and theoretically contextualized, together with the data analysis procedure that will be extensively employed in the following chapters.

2.1 Storage rings and synchrotron light

Synchrotrons are devices capable of accelerating charged particles by using a magnetic field increasing in intensity across a vacuum chamber together with the particle kinetic energy, which at the end is usually in the ultra-relativistic regime, i.e. $E_{kin} \gg E_{rest} = mc^2$, where m is the particle's mass and c is the speed of light [1], [2], [3], [4]. After the development of the first synchrotrons it was discovered that they emitted a peculiar type of electromagnetic radiation, also called synchrotron light.

When the particles (in this case electrons) have reached their target energy, they are injected in a storage ring, where they are maintained as long as possible in orbit by use of electro-cavities in which electric oscillations are synchronized with the orbit of the electrons; synchrotron radiation is emitted as the electrons subjected to magnetic forces accelerate following a curved orbit. The beam of electrons, subdivided in bunches, must remain in a very high vacuum in order to minimize interactions with gas atoms, which are detrimental to the beam: the electric current circulating in the storage ring tends to decrease over time and eventually the beam has to be refilled according to one of the various filling modes available (e.g. in the top-up mode the refill occurs so frequently that the current in the storage ring only slightly fluctuates during operation).

What distinguishes the storage rings from the X-ray tubes as a radiation source, apart from the physical mechanism leading to X-ray emission and the sophisticated methods of X-rays manipulation, is the brilliance, a parameter characterizing the performance of a source of X-rays in terms of its emission bandwidth, flux and angular distribution. Nowadays, the fourth-generation of synchrotron

light sources is being developed (e.g. the ESRF, a third-generation source, has been upgraded to ESRF-EBS), with the intention of ultimately pushing their design concepts to their fundamental limits.

The relativistic γ factor of the electrons affects the synchrotron light properties, e.g. its emission frequency spectrum. In the case of ESRF in Grenoble, France $\gamma \approx 12000$ and in the case of ELETTRA synchrotron in Trieste, Italy $\gamma \approx 4000$ [5], [6]. The spectrum of the radiation emitted by the electrons also strongly depends on the type of magnetic configuration employed. Bending magnets, which consist of a single dipole magnet, are usually employed whenever there is need for a smooth and wide range of photon energies: all the data reported on in this work have been collected at beamlines using the bending magnet configuration. There are however other magnetic configurations, i.e. wigglers and undulators, employing periodic arrays of magnets rather than a single dipole magnet as in bending magnets: they are referred to as insertion devices.

Storage rings are surrounded by beamlines, each dedicated to certain types of measurements. Beamlines usually have these common elements: starting from the joint with the storage ring, usually called the source (as X-rays come from it) there is the optical hutch, which contains the instruments (mirrors,

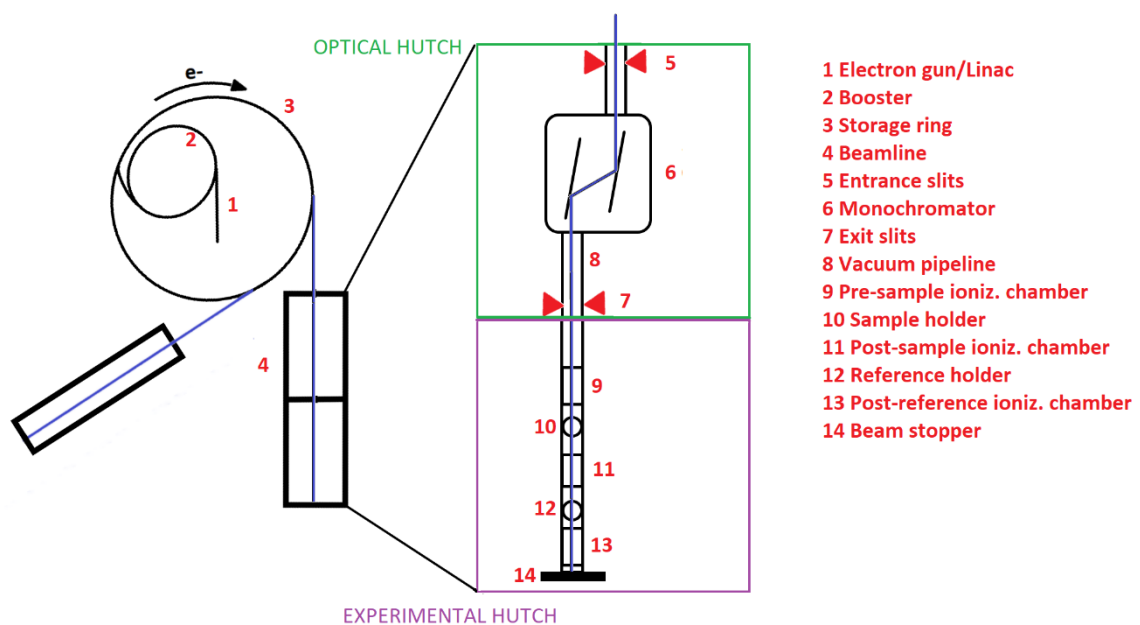


Figure 2.1: Schematics of a typical XAS beamline in the transmission configuration (not in scale).

The X-ray beam is in blue; in the optical hutch there might be X-ray mirrors that are not indicated here

monochromator, slits) devoted to focus, reduce, align and/or monochromatize the radiation coming from the source; then the experimental hutch, where the sample is kept in the conditions required by the experiment and the measurements are performed [6], [7].

The experimental setup employed in this work is that of X-ray Absorption Spectroscopy (XAS) in transmission geometry, that is, the detectors are positioned behind the sample, thus measuring the flux of the X-ray beam after its interaction with the sample itself. In this simple setup it is straightforward to extract the absorbance in accordance with Lambert-Beer law:

$$I(d) = I_0 e^{-\mu d}, \quad (2.1)$$

where μ is the absorption length, d the width of the system in the direction traversed by the X-rays beam and I_0 and $I(d)$ are the intensity of the X-ray beam respectively before and after its interaction with the system. So, two ionization chambers are needed in order to measure the intensity of the radiation before and after its interaction with the sample. The pressure and chemical composition of the gas mixture inside the ionization chambers are determined in order to have the radiation beam attenuated by a known factor. To properly calibrate the energy of the incident photons a reference sample is placed after the second ionization chamber.

2.2 X-ray Absorption Fine Structure

When hard X-rays irradiate a sample their predominant interaction with it is the photoelectric effect: photons are absorbed by the sample and the electrons in the sample are excited.

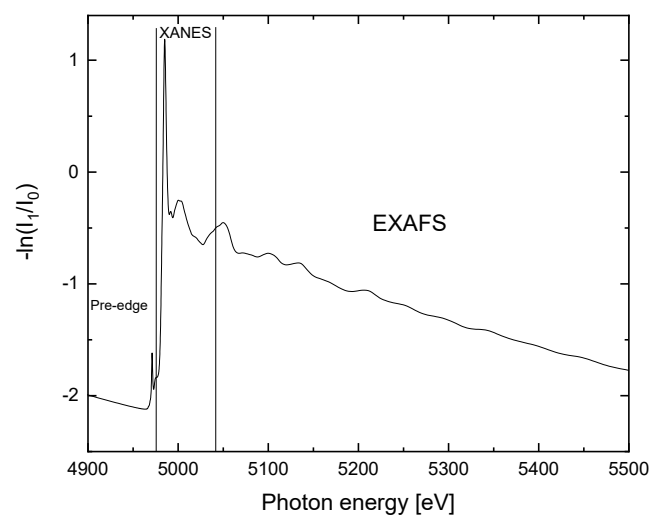


Figure 2.2: An absorption spectrum of $TiCo(CN)_6 \cdot 2H_2O$ @ Ti K-edge acquired at XAFS beamline, ELETTRA at 100K with the interesting energy regimes highlighted

This fact allows to approximate the extinction coefficient with the absorption one. While the photoelectric effect in solids requires in general a quite involved theory, it admits a simple description in the high energy range of the absorption spectrum, so called extended range, due to several key aspects leading to significant simplifications in the theoretical description of the phenomenon, ultimately allowing to reliably extract physical quantities from spectroscopic measurements. The absorption coefficient of materials shows edge displays a discontinuity in correspondence with atomic transitions from deep core states. The absorption spectrum regime near the edge is called XANES (X-ray Absorption Near Edge Structure). Beyond the absorption edge, the absorption coefficient of matter (from molecular gases to solids and liquids) shows oscillations, called Extended X-ray Absorption Fine Structure (EXAFS). A simple illustration of this taxonomy is presented in Figure 2.2. In the early EXAFS studies [8], it was recognized at an empirical level that the X-ray Absorption Fine Structure (XAFS) was well described as a sum of terms of the form:

$$\chi(k) = \frac{N \cdot S_0^2 \cdot f_{eff}(k) \cdot e^{-2R/\lambda(k)} \cdot \sin(2kR + \phi(k))}{k \cdot R^2} \quad (2.2)$$

where $k = \sqrt{\frac{2m_e}{\hbar^2}(E - E_0)}$ is the photoelectron wavevector modulus, $\lambda(k)$ is the inelastic mean free path of the photoelectron, R is the distance between the absorber and the scatterer, N is the degeneracy of the scatterers, f_{eff} and ϕ are the scattering amplitude and phase. This functional form, called the EXAFS equation, can be given a more theoretical context as follows. The phenomenon can be described using the formalism of multiple scattering, which can be developed starting from the following expression, related to the Fermi's Golden rule:

$$\mu \propto \sum_f |\langle f | \vec{\epsilon} \cdot \vec{d} | i \rangle|^2 \delta(\omega + E_i - E_f) \quad (2.3)$$

where $\vec{\epsilon}$ is the polarization vector of the vector potential of the incident electromagnetic field, \vec{d} is the appropriate dipole operator for the system in question, ω is the energy of the incident photon and E_i and E_f are respectively the initial and final energy of the (many-body) system.

A convenient method to perform calculations in this context is based on the reformulation of the absorption coefficient in terms of a (generalized) single-particle electronic Green's function, as in:

$$\mu(E) \propto \text{Im}[\langle i | \epsilon \cdot r G(r, r', E) \epsilon \cdot r' | i \rangle], \quad (2.4)$$

where G is the electron Green's function. The Green's function is calculated solving (perturbatively) the Dyson's equation:

$$G = G_0(1 - TG_0)^{-1}, \quad (2.5)$$

where G_0 is the Green's function for the free electron, while T is the transition matrix relative to the optical potential, accounting for the interaction of the emitted photo-electron with all the others and the ions. Then, formally, $G = \sum_i G_0(TG_0)^i$, where each term has a remarkable form inspiring the concepts of path expansion and multiple scattering. Indeed, in the case $i = 1$ it is G_0TG_0 , where T can be further expanded in terms of the muffin tin core effective potentials as $T = \sum_i t_i$, the index i running over all atoms surrounding the absorber; while in principle all of them should be accounted for, in practice only those not farther than 10\AA from the absorbing atom give relevant contributions. Usually, the EXAFS analysis results weakly depend on the details of the potential chosen in the interstitial regions between atom cores. The electronic structure is strongly related to chemical properties of the materials and to the electronic density of states, influencing other strongly related properties, e.g. the XANES. In fact, the kinetic energy of the EXAFS photoelectrons is too high for them to be significantly influenced by the slowly varying details of the electron structure between atoms that dictate the chemical properties of the material [9]. This is usually employed in considerably simplifying the potential in a muffin-tin form. The absolute value of the absorption coefficient is not very important for this discussion, since in the end only the fine structure

$$\chi(k) = \frac{\mu - \mu_0}{\mu_0} \quad (2.6)$$

will be considered; it is however important to consider the role of the background absorption signal μ_0 , due to the absorber atom alone (but in general not the isolated specie) [10], [11].

2.2.1 The EXAFS equation

The EXAFS equation is available to describe how the XAFS depends on the photoelectron wavevector. It is immediately evident that, to practically employ it, either the scattering amplitudes and phases must be obtained in a reliable way or removed from the problem (e.g. by the ratio method) [12], [13]. We will illustrate and use the first approach. The X-ray Absorption Fine Structure contribution due to the i -th path is:

$$\chi_i(k) = \frac{N_i \cdot S_0^2 \cdot f_{eff,i}(k) \cdot e^{-2R_i/\lambda_i(k)} \cdot \sin(2kR_i + \phi_i(k))}{k \cdot R_i^2} \quad (2.7)$$

where R_i , $f_{eff,i}$, ϕ_i are referred to the i -th path.

The final result, which is the one to be compared to experimental results, is both an average over time (usually substituted by a suitable ensemble average) and over all the absorbing atoms, here indicated with angle brackets $\langle \dots \rangle$:

$$\langle \chi(k) \rangle = \text{Im} \left[e^{i\phi(k)} f_{eff}(k) \langle e^{2ikR_i} \cdot e^{-2R/\lambda(k)} / R^2 \rangle \right] \quad (2.8)$$

that can be rewritten using the cumulants (C_n) of an effective atomic pairs distance distribution:

$$\langle \chi(k) \rangle = \frac{N \cdot S_0^2 \cdot f_{eff}(k) \cdot e^{-2R/\lambda(k) - 2k^2 C_2 - \frac{2}{3} k^4 C_4} \cdot \sin \left(2kC_1 + \frac{4}{3} C_3 k^3 + \phi(k) \right)}{k \cdot C_1^2} \quad (2.9)$$

At this point the problem of path proliferation emerges, since the number of paths rapidly increases as the number of the included atomic shells surrounding the absorbing atom increases and with it the number of free parameters needed.

The cumulants of a distribution of the atomic distances are defined using the following equation:

$$e^{\sum_{i=0}^{\infty} C_n (it)^n / n!} = \langle e^{itX} \rangle \quad (2.10)$$

It is possible to express the n -th cumulant in terms of the moments by taking the n -th derivative with respect to t and evaluating it at $t = 0$, as in $\frac{d^n}{dt^n} \ln \langle e^{itX} \rangle |_{t=0} = C_n$. The first cumulant is the first moment, the second and third cumulants are respectively the second and third central moments; however, this simple trend doesn't hold for higher order cumulants: e.g. $C_4 = \langle (X - \langle X \rangle)^4 \rangle - 3(C_2)^2$. The difference between the real distance distribution cumulants of order higher than the first and the effective ones is usually negligible in EXAFS spectroscopy. The first cumulant however must be corrected: a good approximation is given by the expression $C_1^* = C_1 + \frac{2C_2}{C_1} (1 + C_1/\lambda)$, where λ is the central value of the inelastic free path [14]. At this point it will be clear that the absolute values of the cumulants have little physical meaning in general, since they are strongly correlated with the S_0^2 and E_0 quantities, which have to be fitted. This conclusion doesn't hold if the S_0^2 and E_0 parameters can be reliably known by other means (e.g. calibration on known substances containing the same atomic specie with a similar electronic structure).

However, if the goal of the analysis is to obtain the values of the cumulants relative to those of one spectrum (usually the one at the lowest temperature), then a trend in temperature or other relevant quantities may be reliably extracted. The basic assumption on the S_0^2 and E_0 quantities for this procedure to yield correct results is that they must be (at least approximately) considerable as equal. This is usually the case if the temperature changes don't imply changes in valence state of the absorbing atom. The visual inspection of the XANES is usually sufficient to ascertain the validity of these assumptions. The alignment of the sample spectra allows to assign the same E_0 parameter to all spectra during the fitting procedure: this fact is crucial to compare the first cumulants at different temperatures, since they are strongly correlated with the E_0 parameter.

2.2.2 EXAFS dependence on local vibrational dynamics

Dynamic thermal disorder might be understood as the deviation from ideality of the crystal structure due to thermal motion, which give contributions to the EXAFS second cumulant. In general, though, the second cumulant doesn't receive contributions only from the atomic motions, as can be deduced from the

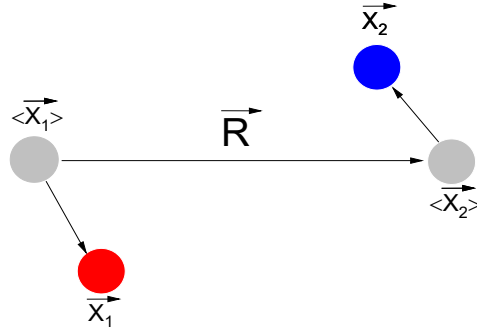


Figure 2.3: A schematic pair of atoms displaced from their equilibrium positions

definition, but also in the case of atomic (average) positions not arranged in a regular crystal. The difference between the second cumulant and its contributions due to thermal motions is referred to as static second cumulant and can be intuitively thought as arising from a static disorder.

A few definitions may clarify the notation of the following remarks, illustrated in Figure 2.4: \vec{X}_1 and \vec{X}_2 are the positions of the atoms in the selected atomic pair, $\vec{R}_{cryst} := \langle \vec{X}_2 - \vec{X}_1 \rangle$ is the average position difference of the atomic pair, that will also be referred to as \vec{R} for brevity, while \vec{u}_1 and \vec{u}_2 represent the displacements of atoms from the respective average positions, i.e. $\vec{u}_i := \vec{X}_i - \langle \vec{X}_i \rangle$.

In the following chapters, two approximations will allow us to access the longitudinal and transverse *MSRDs* starting from the EXAFS real distribution cumulants will be employed extensively: it is thus important to understand their origin and validity. In particular, the $MSRD_{\parallel}$, defined as $\langle ((\vec{u}_2 - \vec{u}_1) \cdot \hat{R}_{cryst})^2 \rangle$, is approximated to a good amount by the second cumulant:

$$C_2 := \langle (r - \langle r \rangle)^2 \rangle \approx MSRD_{\parallel}, \quad (2.11)$$

while the $MSRD_{\perp}$, defined as $\langle |(\vec{u}_2 - \vec{u}_1)|^2 \rangle - MSRD_{\parallel}$, is approximated by the expression:

$$MSRD_{\perp} \approx 2 \cdot R \cdot (C_1^* - R). \quad (2.12)$$

In this context, the anisotropy γ of thermal disorder is defined as:

$$\gamma := \frac{MSRD_{\perp}}{MSRD_{\parallel}} \quad (2.13)$$

In many relevant cases the data analysis might show complications even in the simplest case, that of single scattering: the atomic neighborhood of the absorbing atom might consist of different atomic species with only slightly different atomic number or inequivalent atoms of the same type with distances from the absorber that don't differ enough to be treatable as different paths in the fit, both for the obvious proliferation of fitting parameters and for the physical limits on resolution of distances by EXAFS experiments. A pragmatic solution is to employ an average (weighted with f_{eff} values) of similar paths. In this case the static thermal disorder gives an important component to the second cumulant. Also, the weighted mean must be reasonably performed, usually comprising only paths with very similar transition amplitudes dependence on the wavevector.

It is worth to elaborate a little more on the fact expressed in Eq. (2.12), as the existence of two different yet similar quantities could be confusing on the experimental side of the issue. The equilibrium lattice parameters and interatomic distances are usually extracted using (X-rays or neutrons) diffraction techniques; those access the "apparent" atomic distances, i.e. R in Eq. (2.12). This follows from the general theory of diffraction: the field scattered from an atom is of the form $e^{i\vec{k}\cdot\vec{R}}$ and the total scattered field is proportional to $\sum_i e^{i\vec{k}\cdot\vec{R}_i}$ (with the index i running over all atoms in the crystal), thus, all that the technique can probe is the apparent distance, because, taking a suitable thermal average of the total scattered field we obtain

$$\left\langle \sum_i e^{i\vec{k}\cdot\vec{R}_i} \right\rangle \approx \sum_i e^{i\vec{k}\cdot\langle\vec{R}_i\rangle} e^{-k^2\sigma_i^2/2}, \quad (2.14)$$

where σ_i^2 is the Debye-Waller factor, so the interference conditions are determined by the $\langle\vec{R}_i\rangle$ and for example the measured distances between crystal planes are "apparent" distances, $|\langle\vec{R}_n - \vec{R}_m\rangle|$. Instead, the EXAFS equation contains the first cumulant (the "real" interatomic distance, $C_1^* = \langle|\vec{X}_2 - \vec{X}_1|\rangle$), which differs from R (the "apparent" interatomic distance, $R = |\langle\vec{X}_2 - \vec{X}_1\rangle|$) due to the correlations of the atomic motions. The physical origin of this difference between these techniques relies on the different time period of atomic oscillations and of lifetime of the photoelectron in the EXAFS excited states.

2.3 Sample preparation

One of the main assumptions behind the use of the Lambert-Beer law in the form presented before is that the sample is uniform (at least in the region irradiated by the beam). Thus, inhomogeneities in the sample might hinder the success of the measurement: what is sought after is the absorption constant of the sample compound, but what is measured is the absorbance, which is in general an

integrated quantity depending on the values along optical paths, not easily related to the absorption constant apart from the case of homogenous materials. In order to avoid this issue, the following procedure has been followed: the samples, always in form of powders, have been ground in a mortar for the amount of time necessary to reduce as much as possible the coarse textures of the sample. The sample powder has then been thoroughly mixed with boron nitride powder and the mixture reduced in form of pellet with the use of a pelletizer device and hydraulic press (usually producing 13 mm diameter pellets). The amount of sample powder and boron nitride are determined by imposing that the absorption edge jump be approximately $\Delta\mu_{\text{edge}} \cdot d \approx 1$ (employing the XAFS_{mass} software [15]): if the absorption is too strong the intensity after the sample will be small and thus the spectrum too noisy, whilst if the absorption is too weak the absorbance will be too small and noisy to extract the XAFS reliably.

It must also be considered that the pellet must be fixed to the sample holder with a metallic mask (and eventually Kapton film): it must thus be enough mechanically resistant to endure the procedure without an excessive risk of breaking. In this work this is achieved by the homogenization of the pellet and avoiding abrupt stresses during the pressing process: typical values for the pellet mass are in the range $120 \div 150 \text{ mg}$, most of which is boron nitride, a compound that is almost transparent to hard X-rays if compared to usual samples; however a compromise must be made between stability and homogeneity of the pellet: the higher the filler to sample powder ratio, the longer and more thoroughly the powder mixture must be mixed (also with more chances of obtaining inhomogeneous samples).

To further lower the error due to inhomogeneities an alignment procedure is performed before initiating the acquisition process: the samples are scanned both horizontally and vertically after having diminished the beam size in the direction of the scanning to find the most homogeneous region. In this type of setup, the beam size during the data acquisition is as wide as it can be to take advantage of the high photon flux emitted from the source.

2.4 Data acquisition

Once the samples are allocated in their holder a high vacuum is produced inside of it both to avoid intolerable absorption of the X-ray beam and for thermal insulation of the sample. The temperature of the sample is controlled using a helium cryostat at lower than ambient temperatures and by Joule heating to reach temperatures higher than ambient temperatures. Temperature control is crucial for

the success of the experiments described in this work: the temperatures are usually to be intended with a 0.1 K uncertainty.

The measured quantities are the time-integrated photon fluxes in the ionization chambers; thus, the measure is sustained for a determined period of time (integration time), ensuring a precise value of the measured intensity. An integration time not lower than 2 seconds is employed during the data acquisition (lower integration times are employed during alignment and calibration procedures). Further, various absorption spectra should be acquired for each state (e.g. temperature) of each sample to allow for a simpler treatment of the uncertainties on the final results of the data analysis; it is usually unfeasible to acquire more than 2 or 3 repeated spectra due to the time constraints of these experiments, since typical acquisition requires 30-45 minutes without the dead times due to temperature change and equilibration.

The beam flux is usually sampled at an evenly spaced mesh of energy points, coarse in the pre-edge (≈ 10 eV with the exception of the presence of pre-edge peaks), dense in the edge region (≈ 0.2 eV or larger depending on the energy resolution at the chosen energy), where the intensity changes rapidly with energy; in the post-edge range (from approximately 50 eV above the edge energy) the sampling mesh is non-uniform in energy and uniform in the wavevector modulus instead: this is useful because it both simplifies the Fourier transform of the XAFS signal and helps significantly quickening the measurement procedure by sampling less densely in the high energy regime, where the noise to signal ratio is higher.

2.5 Data analysis procedure

Returning to the EXAFS data analysis, it can be described as follows. After the energy scale has been calibrated, the absorption spectra must be aligned and eventual glitches removed. Since the absorbance is proportional to the sample thickness, the XAFS oscillations must be normalized as

$$\chi(k) = (\mu - \mu_0)/\mu_0, \quad (2.15)$$

extracting the XAFS signal. The subtraction of the background μ_0 is a crucial passage, since the quality of the resulting XAFS signal depends on it: to perform this and other preprocessing operations on the acquired spectra a number of software are available, in this work we have used the ATHENA software from the DEMETER package [16]. The EXAFS fitting procedure that follows is implemented in this work using the FEFFIT software [13], which combines the output of the previous calculations of scattering amplitudes, phases and inelastic mean free paths performed by the FEFF software [17]

with the parametric model defined by the user. Regarding the latter, a number of choices must be made, which comprise the number of paths to be included in the fit, the number of parameters for each path and which constraints between the various cumulants are to be enforced. If this procedure is successful, the fit results (most importantly the cumulants of the atomic pair distance distribution) may be elaborated to obtain the desired quantities regarding vibrational anisotropy. Where several absorption spectra have been acquired at the same temperature, the mean of the resulting cumulants has been used in the data analysis [18], [19], [20], [21], [22].

2.5.1 Preprocessing

The data analysis procedure begins with the calibration of one of the reference spectra, which yields a correct energy scale, and the alignment of the various reference spectra to the calibrated one, which is necessary if they are to be compared, especially considering the strong correlation of the first and third cumulants with the edge energy E_0 . The calibration is performed by assigning the edge of the reference spectrum its literature value: the edge is identified conventionally as the point of maximum of the first derivative of the (smoothed, if necessary) normalized absorbance. The reference spectra are taken on a known substance, maintained at room temperature, after the sample along the beam trajectory. The sample spectra can thus be aligned by and aligning the reference spectra.

In the absence of reference spectra or if they are of too low quality to be calibrated and/or aligned, the procedure might be performed with the sample spectra themselves, usually employing the spectrum at the lowest temperature as a reference for calibration and then aligning the others to it: in this case the energy scale is probably incorrect, but the relative values of the physical results (in particular the first cumulants) are not affected, as they are not correlated to the edge energy, differently from their absolute values. However, this might not be always possible, since the edge structure can depend on the temperature, as the valence state of the absorbing atoms changes or for other subtler reasons, e.g. changes in the effective coordination geometry and/or in the symmetry of the atomic neighborhood of the absorber.

As pointed out before, the XAFS signal is obtained by subtraction of a background signal from the absorption spectrum, which is to be intended not as the absorption due to the isolated atom, but the contribution in the case in which the photoelectron is not scattered by the atoms surrounding the absorbing one. The method employed in this work, as implemented in the ATHENA software, exploits the fact that the background (apart from the near edge region) varies more slowly with energy than

the fine structure which is a rapidly oscillating function of energy. In other terms, it is composed by low Fourier components in the R -space (the reciprocal to the k -space). In particular, it is a well-established fact that in most experimental cases Fourier components in the R -space with $R \lesssim 1 \text{ \AA}$ are not related to the XAFS signal, but are instead contributing to the background absorption. This might be understood considering the typical values of the atomic distances, which are rarely lower than 1 \AA for the atomic neighborhoods of heavy absorber atoms.

2.5.2 Model building and fitting

Once the background has been removed, the scattering amplitudes and phases must be calculated to use the EXAFS equation presented above. In this case, this is obtained by the use of the FEFF software, which takes as input a crystallographic structure in the form of an atomic cluster centered on the absorber atom. This must be obtained in an independent way, in this case by diffraction techniques. In the case of EXAFS spectroscopy, the results of these calculations are weakly dependent on the crystallographic input and other computational details, such as the cluster size. As an aside, as can be understood from the discussion above, this is different from the case of XANES spectroscopy, where the convergence with cluster size and other computational parameters must be carefully ascertained.

To initiate the fitting procedure the Fourier transform of the properly weighted XAFS data $\chi(k)$ is calculated:

$$\tilde{\chi}(R) = \frac{1}{\sqrt{2\pi}} \int_{k_{min}}^{k_{max}} dk \cdot \chi(k) k^w e^{-i2kR} W(k) \quad (2.16)$$

To complete the input to the fitting procedure, a number of settings must be carefully chosen: the range of values of k and R considered, the window function type $W(k)$ and its parameters, the k -weight w , the number of paths, the cumulants for each path, the constraints among the cumulants. In the case of multiple scattering the first and second cumulants are assigned as follows: the first cumulant is the weighted sum of the first cumulants of the partial paths (one half per leg), while the second cumulant is the weighted sum of the second cumulants of the partial paths (again one half per leg) [23]. While the first procedure is quite robust, the second heavily relies on the assumption that the motions of the atoms involved as scatterers in the path are uncorrelated, which is of course not exact.

2.6 Results elaboration

As previously indicated, the longitudinal MSRD may be well approximated by the dynamical second cumulant, while the transverse MSRD is recovered from the comparison of the first cumulant obtained by EXAFS spectroscopy and the (average) crystallographic distance obtained by diffraction techniques.

However, in order to obtain the thermal vibration anisotropy γ , the absolute values of the MSRD transverse and longitudinal are required. Since only the relative values of the cumulants are (reliably) obtainable from the EXAFS fitting procedure, a procedure is needed to recover the absolute values from the temperature trend of the relative values. This is obtained fitting the temperature trend of the MSRDs with a given function that approximates them well: in this work the Einstein model (plus an additional constant that is later subtracted) has been employed, which for the longitudinal and transverse *MSRDs* is:

$$MSRD_{\text{dyn},\parallel}(T) = \frac{\hbar}{2\mu\omega_{E,\parallel}} \coth\left(\frac{\hbar\omega_{E,\parallel}}{k_B T}\right) \quad (2.17)$$

$$MSRD_{\text{dyn},\perp}(T) = \frac{\hbar}{\mu\omega_{E,\perp}} \coth\left(\frac{\hbar\omega_{E,\perp}}{k_B T}\right) \quad (2.18)$$

where μ is the reduced mass of the atomic pair. The factor of two of difference in the functional form accounts for the presence of two transverse normal modes for each wavevector. It should be noted that although the Debye model for the dispersion of phonons in solids is more realistic, the Einstein model displays almost the same fit results with the same number of free parameters and the benefit of a much simpler functional form.

A common case is that in which the considered paths are not crystallographically equivalent, but only similar in length and atomic configuration. If their length is too similar the acquired data might be insufficient to distinguish their contributions to the EXAFS signal, thus requiring their fitting parameters to be dependent upon each other. Therefore, the resulting quantities are to be considered as a mean of the individual cumulants, appropriately weighted with path degeneracy and effective scattering amplitude: if the first cumulant is referred to a weighted average of similar paths, it must be compared to the average, weighted in the same way, of the involved crystallographic distances. As the effective scattering amplitude depends on the photoelectron wavevector, this procedure is best suited to paths that have scattering amplitudes with a similar trend with the wavevector.

Further, the resulting second cumulant usually has a non-negligible static component, which can show an important variation with temperature. This static component can be estimated as the standard deviation of the different distances at each temperature, weighted in the same way as the average of bond lengths. The dynamic component of the second cumulant is obtained by subtracting the static component from the second cumulant obtained from the fits, at last allowing to calculate the γ anisotropy ratio.

As a further effort, the effective bond-stretching force constant κ are calculated using the following formulas:

$$\kappa_{\parallel} = \mu\omega_{E,\parallel}^2 \quad (2.19)$$

while the effective bond-bending force constant can be expressed as:

$$\kappa_{\perp} = \mu\omega_{E,\perp}^2 \quad (2.20)$$

These quantities allow the quantification of the stiffness of atomic pairs in a temperature-independent way, although in general they are not actual interatomic force constants, which are usually defined starting from a microscopic theory of the crystal, as was done in the previous chapter. A useful relation between the effective force constants and the γ ratio, valid in the harmonic approximation, is

$$\lim_{T \rightarrow \infty} \gamma(T) = 2 \frac{\kappa_{\parallel}}{\kappa_{\perp}}. \quad (2.21)$$

Bibliography

- [1] A. Hofmann, *The Physics of Synchrotron Radiation*, Cambridge University Press.
- [2] D. M. J. Als-Nielsen, *Elements of Modern X-ray Physics*, John Wiley & Sons, 2001.
- [3] J. Jackson, *Classical Electrodynamics*, John Wiley & Sons.
- [4] J. Schwinger, "On the Classical Radiation of Accelerated Electrons," *Phys. Rev.*, vol. 75, p. 1912, 1949.
- [5] D. H. Bilderback et al., "Review of third and next generation synchrotron light sources," *Journal of Physics B: Atomic, Molecular and Optical Physics*, vol. 38, p. S773, 2005.
- [6] A. Di Cicco et al., "Novel XAFS capabilities at ELETTRA synchrotron light source," *Journal of Physics: Conference Series*, vol. 190, p. 012043, 2009.
- [7] F. d'Acapito, G. O. Lepore, A. Puri, A. Laloni, F. La Manna, E. Dettona, A. De Luisa and A. Martin, "The LISA beamline at ESRF," *Journal of synchrotron radiation*, vol. 26, pp. 551-558, 2018.
- [8] E. Stern, D. Sayers and F. Lytle, "Extended x-ray-absorption fine-structure technique. III. Determination of physical parameters," *Phys. Rev. B*, vol. 11, p. 4936, 1975.
- [9] J. Rehr and R. Albers, "Theoretical approaches to x-ray absorption fine structure," *Rev. Mod. Phys.*, vol. 72, no. 3, 2000.
- [10] P. Lee and J. B. Pendry, "Theory of the extended x-ray absorption fine structure," *Phys. Rev. B*, vol. 11, p. 2795, 1975.
- [11] T. Fujikawa and L. Hedin, "Theory of electron scattering from solids," *Phys. Rev. B*, vol. 40, no. 17, p. 11 507, 1989.
- [12] G. Bunker, *Introduction to XAFS. A Practical Guide to X-ray Absorption Fine Structure Spectroscopy*, Cambridge University Press, 2010.
- [13] M. Newville et al., "Analysis of multiple-scattering XAFS data using theoretical standards," *Physica B: Condensed Matter*, Vols. 208-209, pp. 154-156, 1995.
- [14] P. Fornasini, F. Monti and A. Sanson, "On the cumulant analysis of EXAFS in crystalline solids," *J. Synchrotron Rad.*, vol. 8, pp. 1214-1220, 2001.
- [15] K. Klementiev and R. Chernikov, "XAFSmass: a program for calculating the optimal mass of XAFS samples," *J. Phys.: Conf. Ser.*, vol. 712, p. 012008, 2016.
- [16] B. Ravel and M. Newville, "ATHENA, ARTEMIS, HEPHAESTUS: data analysis for X-ray absorption spectroscopy using IFEFFIT," *Journal of Synchrotron Radiation*, vol. 12, pp. 537-541, 2005.
- [17] A. L. Ankudinov et al., "Real-space multiple-scattering calculation and interpretation of x-ray-absorption near-edge structure," *Phys. Rev. B*, vol. 58, p. 7565, 1998.

- [18] P. Fornasini et al., "Bond compressibility and bond Grüneisen parameters of CdTe," *J. Phys.: Condens. Matter*, vol. 30, p. 245402, 2018.
- [19] P. Fornasini and R. Grisenti, "On EXAFS Debye-Waller factor and recent advances," *J. Synchrotron Rad.*, vol. 22, no. 5, pp. 1242-1257, 2015.
- [20] P. Fornasini et al., "Extended x-ray-absorption fine-structure measurements of copper: Local dynamics, anharmonicity, and thermal expansion," *Phys. Rev. B*, vol. 70, p. 174301, 2004.
- [21] P. Fornasini et al., "Local behaviour of negative thermal expansion materials," *Nucl. Instr. and Meth. in Phys. Res. B*, vol. 246, p. 180.183, 2006.
- [22] P. Fornasini, "Study of lattice dynamics via extended x-ray absorption fine structure," *J. Phys.: Condens. Matter*, vol. 13, no. 34, p. 7859, 2001.
- [23] N. Dimakis and G. Bunker, "Ab initio single- and multiple-scattering EXAFS Debye-Waller factors: Raman and infrared data," *Phys. Rev. B*, vol. 58, p. 2467, 1998.
- [24] L. F. Mattheiss, "Energy bands for solid argon," *Phys. Rev.*, vol. 133, p. A1399, 1964.
- [25] L. Hedin and B. I. Lundqvist, "Explicit local exchange-correlation potentials," *J. Phys. C: Solid State Phys.*, vol. 4, p. 2064, 1971.
- [26] J. A. Soininen et al., "Inelastic scattering from core electrons: A multiple scattering approach," *Phys. Rev. B*, vol. 72, p. 045136, 2005.
- [27] J. Rehr et al., "Final-state rule vs the Bethe-Salpeter equation for deep-core x-ray absorption spectra," *Physical Scripta*, vol. 2005, no. T115, 2005.

Chapter 3

Local dynamics and intercalation effects in Prussian Blue Analogues

Experimental results and the relative data analysis regarding the EXAFS of Prussian blue analogues are presented. This class of compounds has been of recent interest due to various of its members displaying anomalous thermal expansion coefficients and promising electrochemically properties. Indeed, it has been proven that by intercalation of small chemical species the thermal expansion coefficient drastically changes: EXAFS spectroscopy, allowing to characterize the local vibrational dynamics, is an invaluable tool in clarifying the mechanism of this phenomenon.

3.1 Prussian blue analogues

Prussian Blue Analogues (PBAs) are a class of compounds comprising metal sites coordinated with cyanide units, arranged in a crystalline structure (e.g. hexagonal: $\text{LuFe}(\text{CN})_6$, cubic: $\text{TiCo}(\text{CN})_6$, $\text{YFe}(\text{CN})_6$, $\text{FeFe}(\text{CN})_6$, $\text{Zn}(\text{CN})_2$). These compounds can present defects of metal atoms and of the relative cyanide units, but even in the ideal form they display significant crystal voids, allowing for intercalation of small chemical species: this is an interesting aspect due to its implications for electrochemistry, as PBAs have the potential to be materials for non-toxic battery cathodes with facile synthesis routes [1], [2], [3], [4], [5].

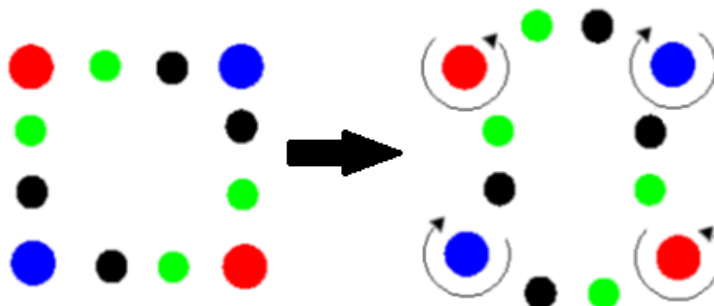


Figure 3.1: Simplified 2D depiction of a (symmetry bearing) portion of crystalline cell undergoing a breathing mode in a cubic hexacoordinated Prussian blue analogue

Several PBAs with negative or zero thermal expansion have been reported [6], [7], [8], [9]: owing to their framework structure, these compounds display relevant RUMs, where the “rigid” units are the polyhedral units consisting in metal atoms and their coordinated nearest neighbors. For example, in the cubic hexacoordinated PBAs (with formula $MM'(CN)_6$) the “rigid” units are the MN_6 and $M'C_6$ octahedra, which undergo breathing motions as depicted in Figure 3.1. in a simplified manner; another example is the normal mode of $Zn(CN)_2$ involving tetrahedral units investigated in [10].

Intercalation with small species in these compounds has been achieved in two ways: electrochemical insertion of small ions and inclusion of water of hydration. The intercalated species are found in the crystal voids typical of these framework structured materials, which inhibits motions of the cyanide groups transverse to their equilibrium axis, thus, if these are the motions relevant to NTE, the CTE should consequently increase. Interstitial water molecules can also be coordinated to the defective sites [11].

In this chapter we report on the EXAFS analysis of two compounds in the PBA class, $TiCo(CN)_6 \cdot 2H_2O$ and $LuFe(CN)_6$, with the goal of studying the vibrational anisotropy of the M-N and M'-C atomic pairs. Images of crystal structures are obtained with the VESTA software [12].

3.2 $TiCo(CN)_6 \cdot 2H_2O$

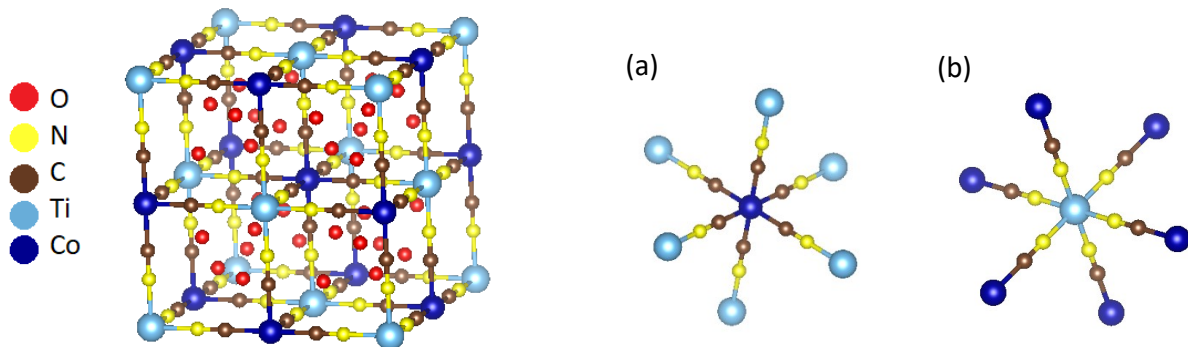


Figure 3.2: (left) Cubic unit cell of $TiCo(CN)_6 \cdot 2H_2O$ defect-free with all water sites occupied. Hydrogen atoms are not shown; (right) local atomic neighborhood of (a) Ti K-edge and (b) Co K-edge

The anhydrous PBA with $M=Ti$ and $M'=Co$ displays NTE, but when its crystal is intercalated with water molecules the NTE changes to ZTE [13], as is shown in Figure 3.3.

XAS data has been acquired at the Ti K-edge (4966 eV) from 100 to 350K with steps of 50K and at Co K-edge (7709 eV) from 100 to 300K with steps of 50K at the XAFS beamline of the ELETTRA

synchrotron light facility. In the EXAFS region the absorption spectrum has been sampled with energy steps that result in a constant k -step of around 0.035 \AA^{-1} .

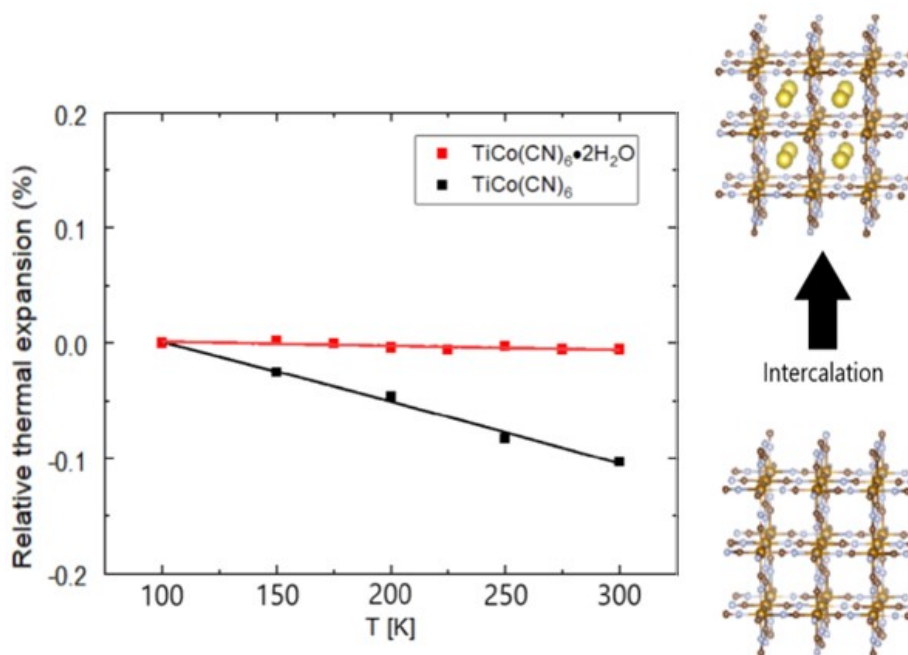


Figure 3.3: Effect of intercalation of water molecules on the thermal expansion of $\text{TiCo(CN)}_6 \cdot 2\text{H}_2\text{O}$

The extracted (k -weighted) XAFS signals have been reported in Figure 3.4: clear oscillations are visible in the lowest temperature (100K) XAFS signal up to $k=16 \text{ \AA}^{-1}$.

The cubic crystal structure of TiCo(CN)_6 is displayed in Figure 3.2, where there is also depicted the local neighborhood of titanium, comprising six nitrogen atoms in the first shell and six carbon atoms in the second shell; conversely, cobalt atoms have six carbon atoms as first shell of neighbors and six nitrogen atoms as a second shell (both atomic neighborhoods are shown): cyanide units link titanium and cobalt atoms, in the $\text{Ti-N}\equiv\text{C-Co}$ arrangement.

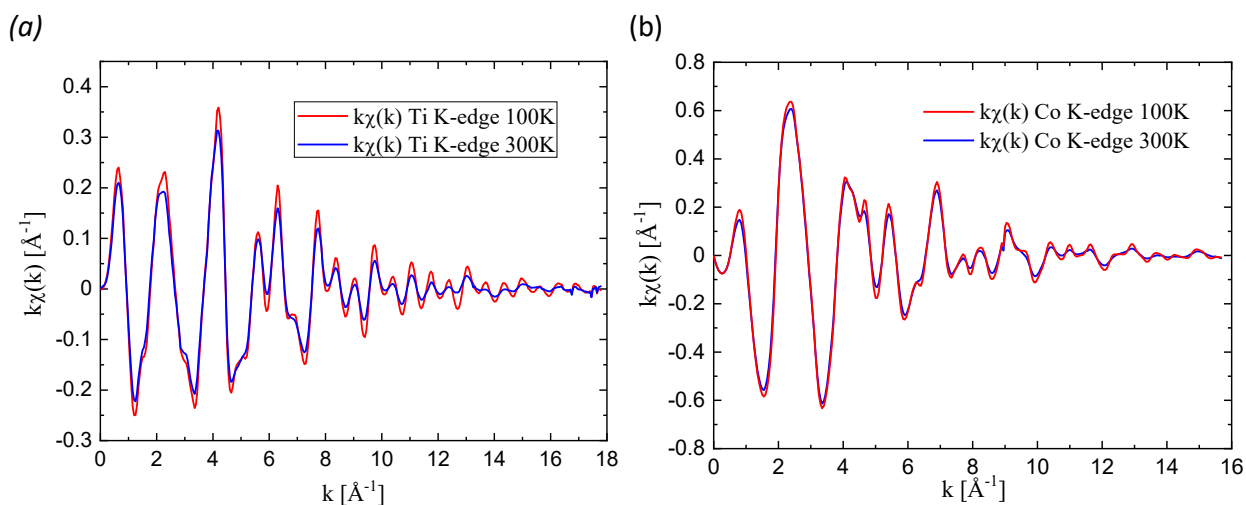


Figure 3.4: Example of EXAFS signals k -weighted for (a) K-edge and (b) Co K-edge

Index	Path	Legs	Degeneracy	r_{eff} [Å]	Amplitude	Parameters
1	Ti-N	2	6	2.0345	100.00	r_1, σ_1^2, C_{31}
2	Ti-C	2	6	3.1336	31.807	r_2, σ_2^2
3	Ti-N-C	3	12	3.1336	184.787	$r_1/2 + r_2/2 + r_3/2$ $\sigma_1^2/2 + \sigma_2^2/2 + \sigma_3^2/2$
4	Ti-N-C-N	4	6	3.1336	292.070	$r_1 + r_3$ $\sigma_1^2 + \sigma_3^2$
5	Ti-N-N	3	24	3.4730	30.368	Neglected
6	Ti-N-N	3	6	4.0689	21.996	Neglected

Table 3.1: Scattering paths for Ti K-edge

Index	Path	Legs	Degeneracy	r_{eff} [Å]	Amplitude	Parameters
1	Co-C	2	6	1.9843	100.00	r_1, σ_1^2, C_{31}
2	Co-O	2	6	2.9878	50.008	Neglected
3	Co-N	2	6	3.0784	36.679	r_2, σ_2^2
4	Co-C-N	3	12	3.0784	200.866	$r_1/2 + r_2/2 + r_3/2$ $\sigma_1^2/2 + \sigma_2^2/2 + \sigma_3^2/2$
5	Co-C-N-C	4	6	3.0784	275.059	$r_1 + r_3$ $\sigma_1^2 + \sigma_3^2$
6	Co-C-C	3	24	3.3874	25.029	Neglected
7	Co-O-C	3	48	3.7127	53.138	Neglected

Table 3.2: Scattering paths for Co K-edge

A collection of the Fourier transformed EXAFS signals is given in Figure 3.5 for both edges, while in Figure 3.6 an example of fit has been given for the Fourier transform of the weighted XAFS signals at the lowest temperature for both edges.

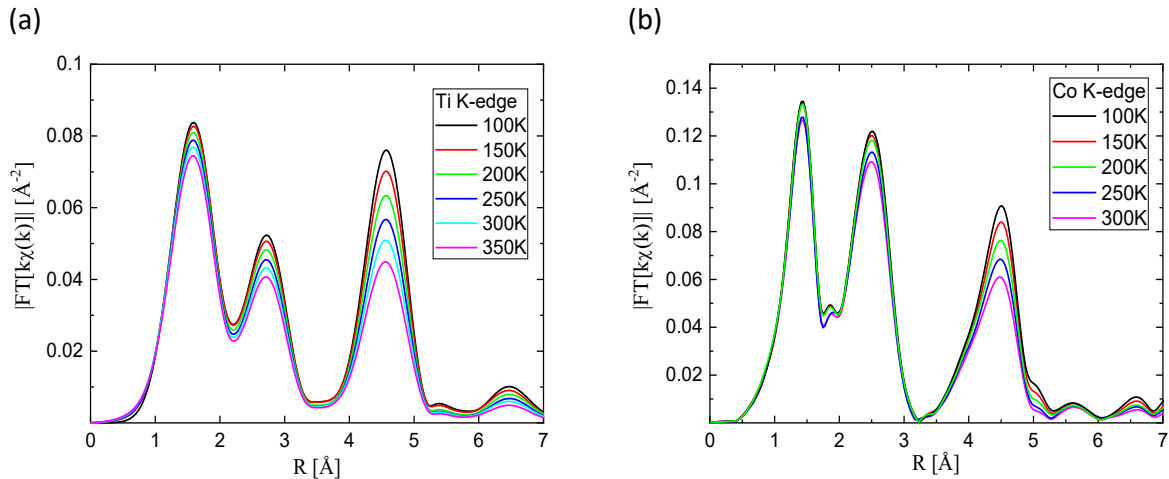


Figure 3.5: Fourier transform of k -weighted XAFS signals for (a) Ti K-edge and (b) Co K-edge

The linear chain structure of the metal-cyanide-metal structure leads to the phenomenon of linear focusing in EXAFS, in which multiple scattering paths can give contributions comparable (if not greater) to those of single scattering paths (as is in this case, see the FEFF amplitudes in Table 3.1 and Table 3.2):

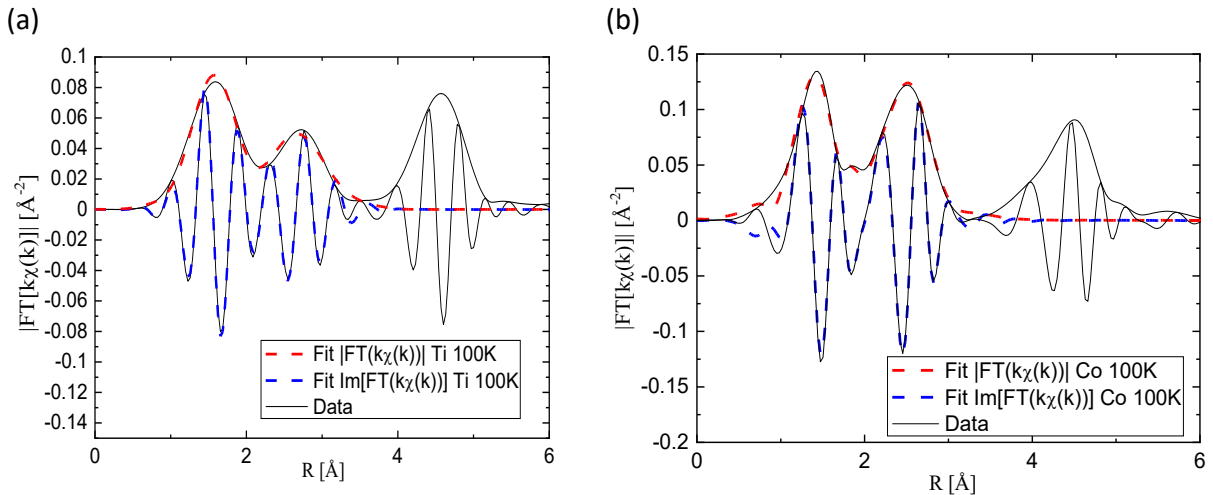


Figure 3.6: Examples of fits of Fourier transformed k -weighted XAFS signals of (a) Ti K-edge and (b) Co K-edge at 100K

thus, it was necessary to include the single scattering from the second shell and the double scattering from the cyanide unit. The third peak is due to contributions from the third shell (the other metal atomic specie) and more complicated multiple scattering paths involving the cyanide unit (again with the linear focusing phenomenon).

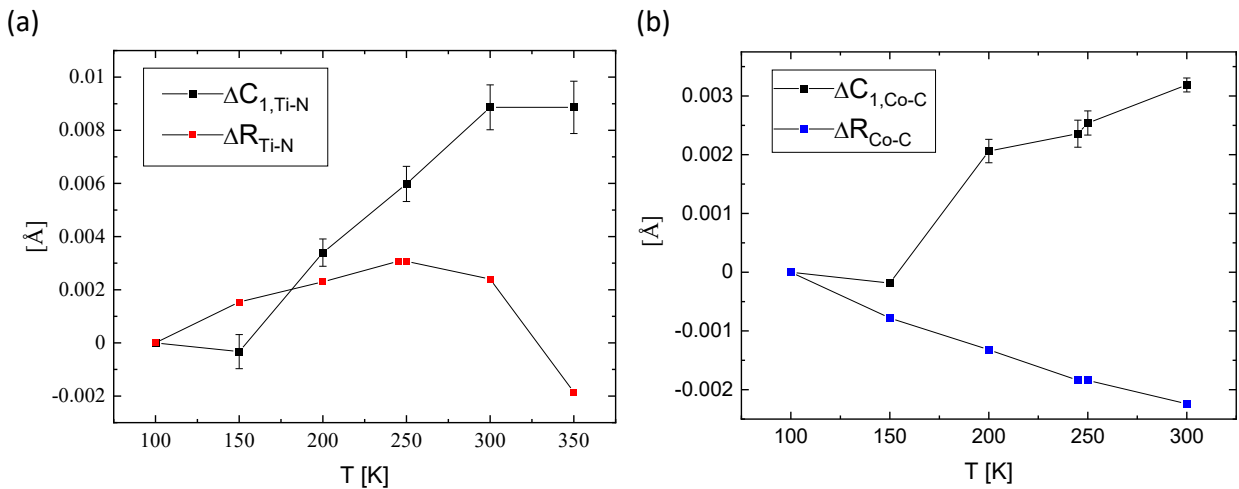


Figure 3.7: Comparison between ΔC_1 and ΔR at different temperatures for (a) Ti K-edge and (b) Co K-edge

In the cobalt K-edge spectra the contributions to the second peak due to oxygen were neglected, even if the FEFF calculation gives a high contribution to the signal (see Table 3.1). However, these estimates are calculated assuming a complete occupation of the water sites, as per the crystal structure in Figure 3.2, which is not realistic. The EXAFS data analysis has been conducted including the paths reported in Table 3.1 for Ti K-edge, while for data at Co K-edge in Table 3.2.

Having obtained the cumulants, the longitudinal and transverse MSRDS can be calculated; as can be seen in Figure 3.7, the “real” and “apparent” nearest neighbors distances indeed display a difference that can be ascribed to transverse motions (as discussed in Chapter 2, see Eq. 2.12), which, as already mentioned in Chapter 1, can play a fundamental role in NTE. The $MSRD_{\perp}$ has been reconstructed by means of an Einstein fit and is presented for Ti and Co K-edges respectively in Figure 3.8, together with the reconstructed $MSRD_{\parallel}$ and their ratio γ : the vibrational anisotropy of the Ti-N atomic pairs is only slightly greater than that of the Co-C atomic pairs, contrary to the case of the anhydrous form $TiCo(CN)_6$ [13]. A summary of the vibrational anisotropy parameters is presented in Table 3.3. Further details and a report on other experimental characterization of $TiCo(CN)_6$ (and its anhydrous form) are present in [13].

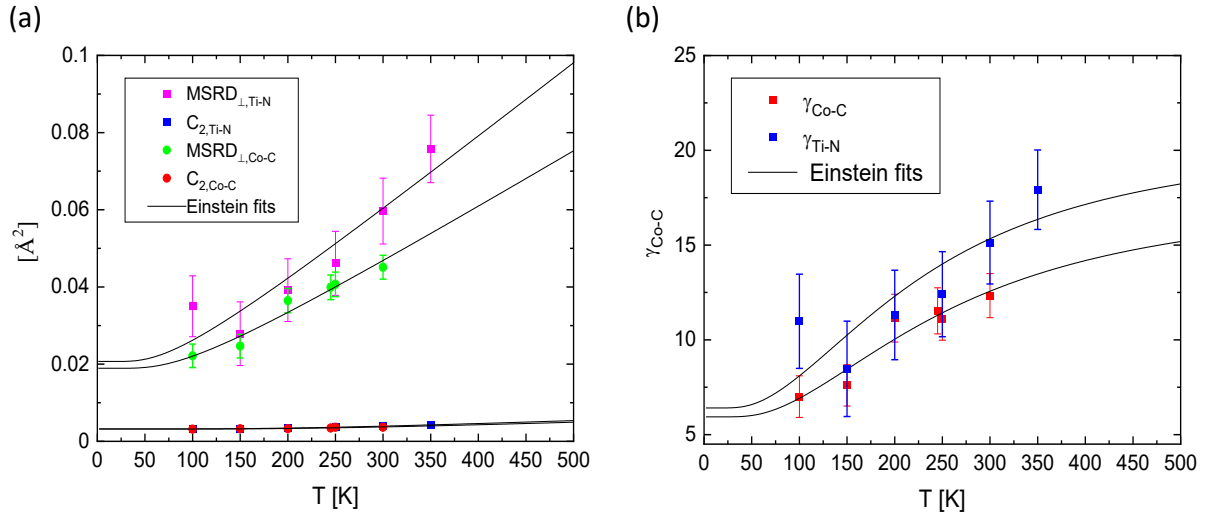


Figure 3.8: Thermal disorder parameters for Ti and Co K-edge (a) MSRDS longitudinal and transverse; (b) anisotropy

Ti-N	Co-C
Stretching $\nu_{\parallel} = (14.44 \pm 0.22) THz$ $k_{\parallel} = (9.25 \pm 0.28) eV \cdot \text{\AA}^{-2}$	Stretching $\nu_{\parallel} = (15.90 \pm 0.91) THz$ $k_{\parallel} = (10.32 \pm 1.18) eV \cdot \text{\AA}^{-2}$
Bending $\nu_{\perp} = (4.46 \pm 0.38) THz$ $k_{\perp} = (0.88 \pm 0.15) eV \cdot \text{\AA}^{-2}$	Bending $\nu_{\perp} = (5.35 \pm 0.26) THz$ $k_{\perp} = (1.17 \pm 0.11) eV \cdot \text{\AA}^{-2}$
Anisotropy $\gamma = (15 \pm 2) @ 300K$ $k_{\perp}/k_{\parallel} = (0.096 \pm 0.016)$	Anisotropy $\gamma = (12 \pm 1) @ 300K$ $k_{\perp}/k_{\parallel} = (0.11 \pm 0.03)$

Table 3.3: Vibrational anisotropy parameters for $TiCo(CN)_6$

3.3 LuFe(CN)₆

LuFe(CN)₆ is instead a PBA with a negative volumetric thermal expansion, displaying a hexagonal crystal structure, which is presented in Figure 3.9, together with the atomic local neighborhoods of

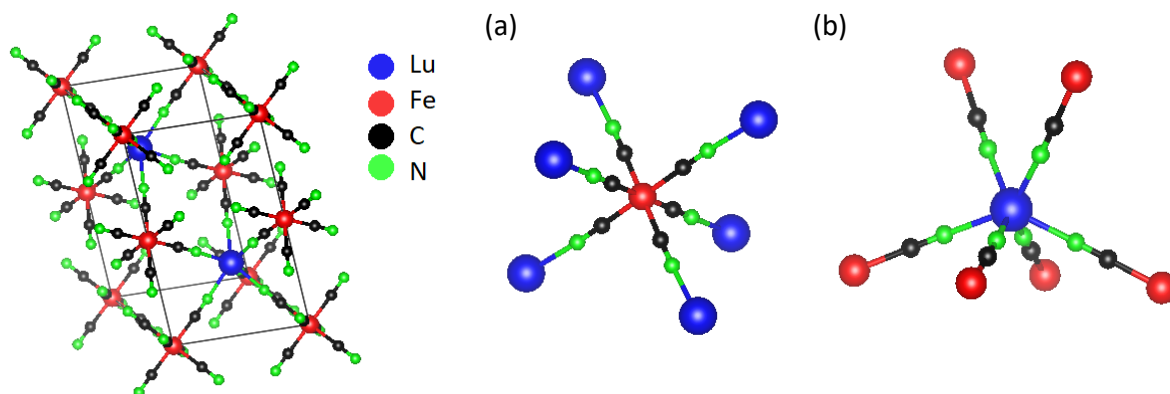


Figure 3.9: Crystal structure of (defect-free) LuFe(CN)₆; Atomic local neighborhood for (a) Fe and (b) Lu atoms

Fe and Lu atoms. XAS data have been acquired at XAFS beamline of ELETTRA synchrotron light source at temperatures from 300 to 525K with steps of around 40K at both the Lu L₃-edge (9244 eV) and Fe K-edge (7112 eV); the relative XAFS signals are shown in Figure 3.10. In the EXAFS region the absorption spectrum has been sampled with energy steps that result in a constant k step of around 0.035 Å⁻¹.

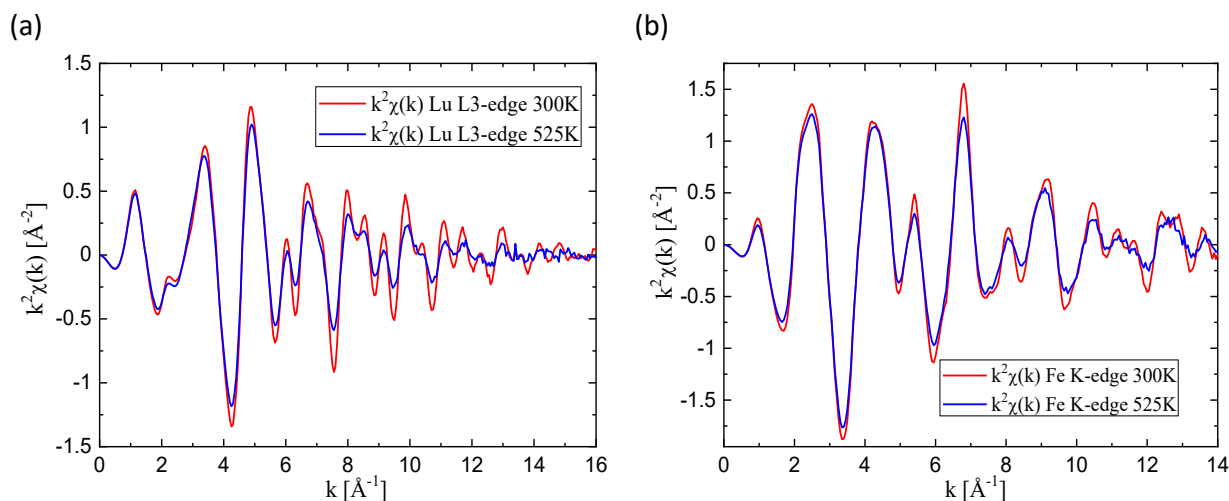


Figure 3.10: Example of XAFS signals k^2 -weighted for (a) Lu L₃-edge and (b) Fe K-edge

Assuming the aforementioned crystal structure, FEFF calculations for Lu L₃-edge were performed including the scattering paths in Table 3.5; the FEFF scattering paths for Fe K-edge are reported in Table 3.4, respectively.

A collection of Fourier transforms of XAFS signals is in Figure 3.11: the first peak is contributed by the scattering from the first shell, the second mainly by the second shell single scattering and the important linear focused path and the third by the third shell single scattering (the other metal atomic specie) and other multiple scattering paths.

Index	Path	Legs	Degeneracy	r_{eff} (Å)	Amplitude	Parameters
1	Fe-C-Fe	2	6	1.9311	100.0	r_1, σ_1^2, C_{31}
2	Fe-N-Fe	2	6	3.0809	35.4	r_2, σ_2^2
3	Fe-C-N-Fe	3	12	3.0809	169.2	$r_1/2 + r_2/2 + r_3/2$ $\sigma_1^2/2 + \sigma_2^2/2 + \sigma_3^2/2$
4	Fe-C-N-C-Fe	4	6	3.0809	202.1	$r_1 + r_3$ $\sigma_1^2 + \sigma_3^2$
5	Fe-C-C-Fe	3	24	3.2964	26.0	Neglected

Table 3.4: Scattering paths for $\text{LuFe}(\text{CN})_6$ Fe K-edge

Index	Path	Legs	Degeneracy	R_{eff} (Å)	Amplitude	Parameters
1	Lu-N-Lu	2	6	2.3003	100.0	r_1, σ_1^2, C_{31}
2	Lu-C-Lu	2	6	3.4493	28.9	r_2, σ_2^2
3	Lu-N-C-Lu	3	12	3.4498	116.8	$r_1/2 + r_2/2 + r_3/2$ $\sigma_1^2/2 + \sigma_2^2/2 + \sigma_3^2/2$
4	Lu-N-C-N-Lu	4	6	3.4503	115.5	$r_1 + r_3$ $\sigma_1^2 + \sigma_3^2$
5	Lu-N-N-Lu	3	12	3.8396	9.6	Neglected

Table 3.5: Scattering paths for $\text{LuFe}(\text{CN})_6$ Lu L_3 -edge

Examples of fits at room temperature at Lu L_3 -edge and Fe K-edge are shown in Figure 3.12. The R-range for the fit has been selected to include the first two peaks: since the goal of the analysis is the study of the first shell vibrational properties, the first peak has to be included, but also the second, being too near and too intense to be neglected.

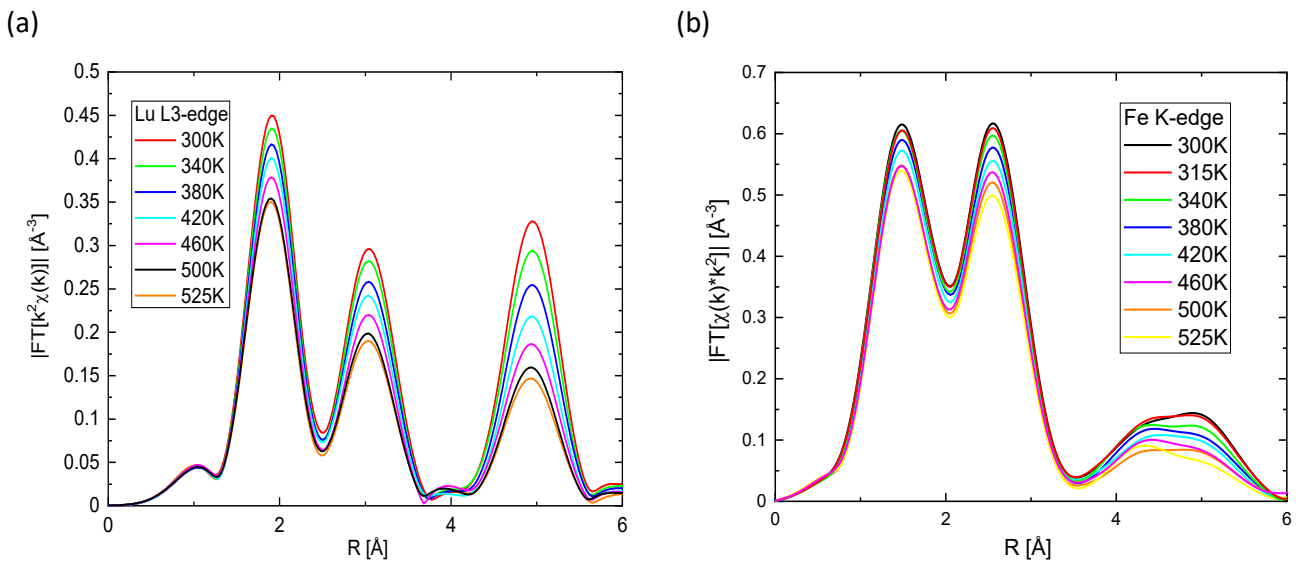


Figure 3.11: Fourier transform of k^2 -weighted XAFS signals (a) Lu L_3 -edge and (b) Fe K-edge

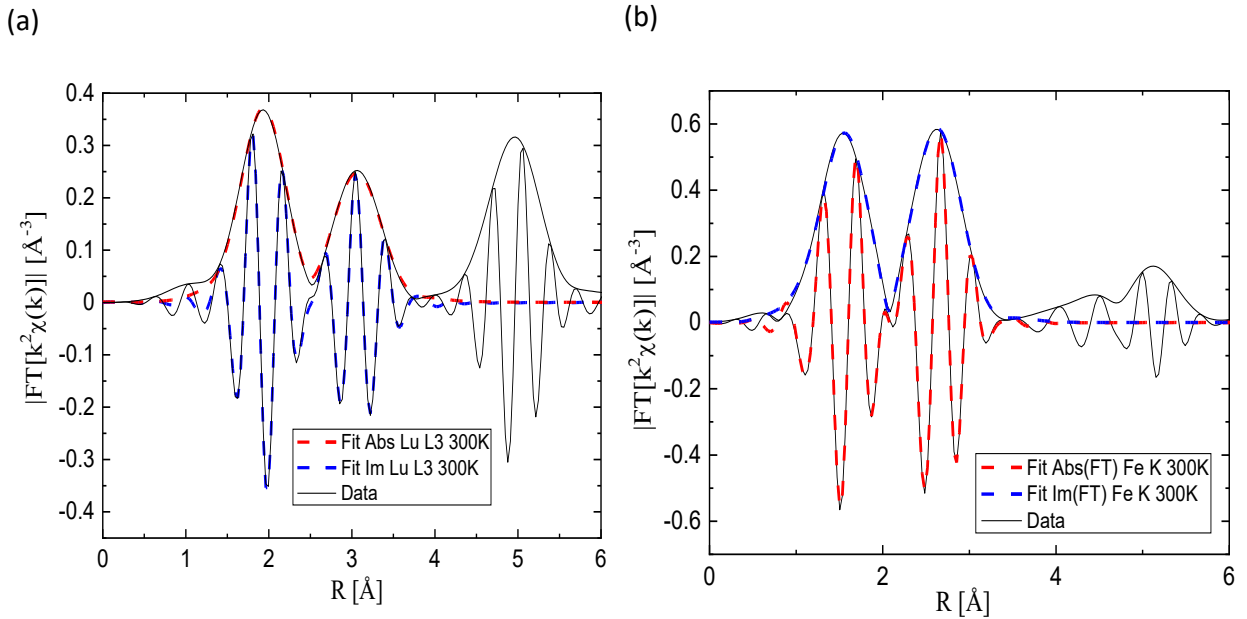


Figure 3.12: Examples of fits Fourier transform of (a) Lu L_3 -edge and (b) Fe K-edge data at 300K

The comparison between “real” and “apparent” nearest neighbors’ distance is in Figure 3.13. The resulting MSRDS (longitudinal and transverse to bond direction) are reported in Figure 3.14 (both Lu L_3 -edge and Fe K-edge), together with their respective Einstein fit and the resulting anisotropy ratio γ : again we see that, as in the case of $\text{TiCo}(\text{CN})_6$, in this NTE Prussian blue analogue the vibrational anisotropy γ of the Lu-N atomic pairs, together with the transversal MSRDS, is definitely greater than that of the Fe-C atomic pairs, suggesting a prominence of the M-N atomic pairs in the NTE mechanism.

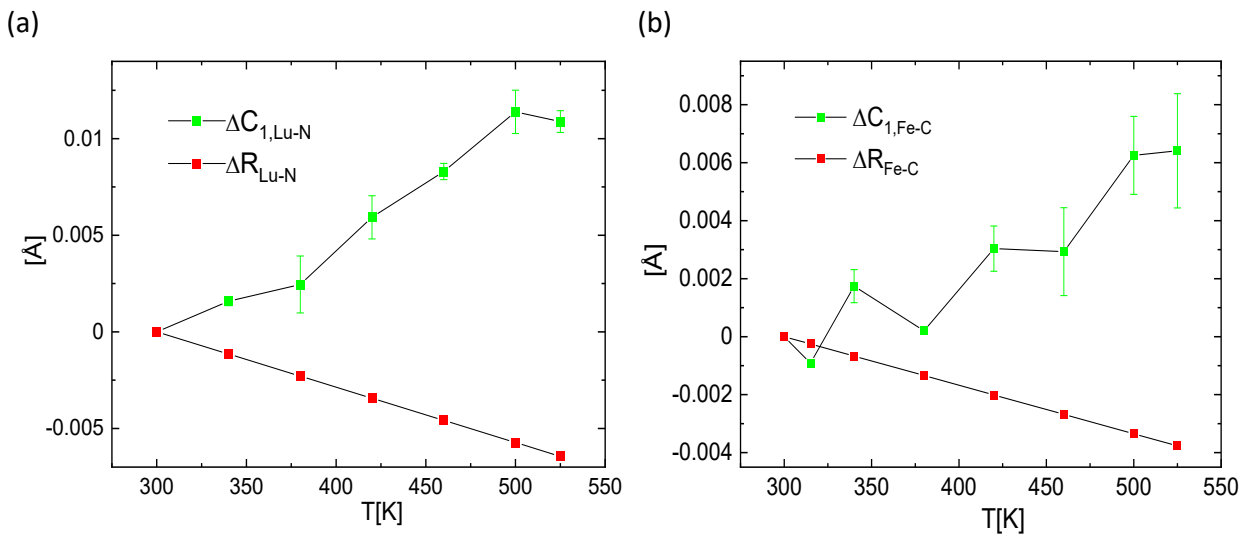


Figure 3.13: Comparison between ΔC_1 and ΔR at different temperatures for (a) Lu L_3 -edge and (b) Fe K-edge

A summary of the vibrational anisotropy parameters can be found in Table 3.6. Other experimental determinations and further details, also comprising a comparison of $\text{LuFe}(\text{CN})_6$ with other rare earth PBAs (La, Y, Ho, Sm), are present in [14].

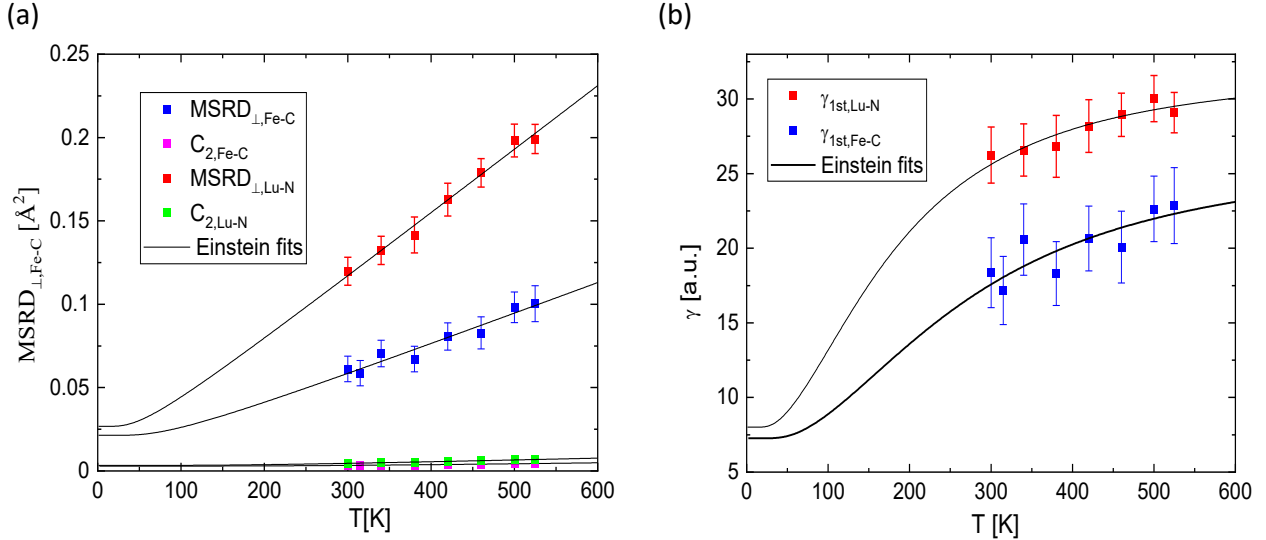


Figure 3.14: Thermal disorder parameters longitudinal and transverse MSRD for (a) Lu-N and Fe-C atomic pairs; (b) anisotropy

Lu-N	Fe-C
Stretching $\nu_{\parallel} = (11.65 \pm 0.09)\text{THz}$ $k_{\parallel} = (7.21 \pm 0.11)\text{eV} \cdot \text{\AA}^{-2}$	Stretching $\nu_{\parallel} = (17.38 \pm 0.26)\text{THz}$ $k_{\parallel} = (12.24 \pm 0.37)\text{eV} \cdot \text{\AA}^{-2}$
Bending $\nu_{\perp} = (2.91 \pm 0.08)\text{THz}$ $k_{\perp} = (0.45 \pm 0.02)\text{eV} \cdot \text{\AA}^{-2}$	Bending $\nu_{\perp} = (4.79 \pm 0.24)\text{THz}$ $k_{\perp} = (0.93 \pm 0.09)\text{eV} \cdot \text{\AA}^{-2}$
Anisotropy $\gamma = (30.0 \pm 1.6)\text{@}500\text{K}$ $k_{\perp}/k_{\parallel} = (0.0624 \pm 0.0034)$	Anisotropy $\gamma = (22.6 \pm 2.2)\text{@}500\text{K}$ $k_{\perp}/k_{\parallel} = (0.0758 \pm 0.0079)$

Table 3.6: Vibrational anisotropy parameters for $\text{LuFe}(\text{CN})_6$

3.4 Discussion and conclusions

Our analysis was limited to two Prussian blue analogues, one with ZTE and one with NTE. However, these can be viewed in a broader context, by examining the relationship between the CTE and the anisotropy of thermal vibrations, quantified in a temperature independent way by using the ratio of the effective force constants it is also interesting to ascertain the different roles of the atomic pairs M-N and M'-C: this is an advantage made available by the EXAFS sensitivity to the local neighborhood of the different atomic species in an independent fashion. In Figure 3.15, these relationships are

presented for both the atomic pair types: the effect of the intercalation seems to be more relevant to the M-N atomic pairs vibrational anisotropy, suggesting a prominent role of those in the NTE mechanism [13], [15], [16].

This is corroborated by the case study of $\text{TiCo}(\text{CN})_6$: the significantly different effects of hydration on Ti-N and Co-C atomic pairs are presented in Figure 3.16. While Ti-N transverse vibration are greatly hindered by occupation of the crystal voids, those of Co-C pairs are unaffected.

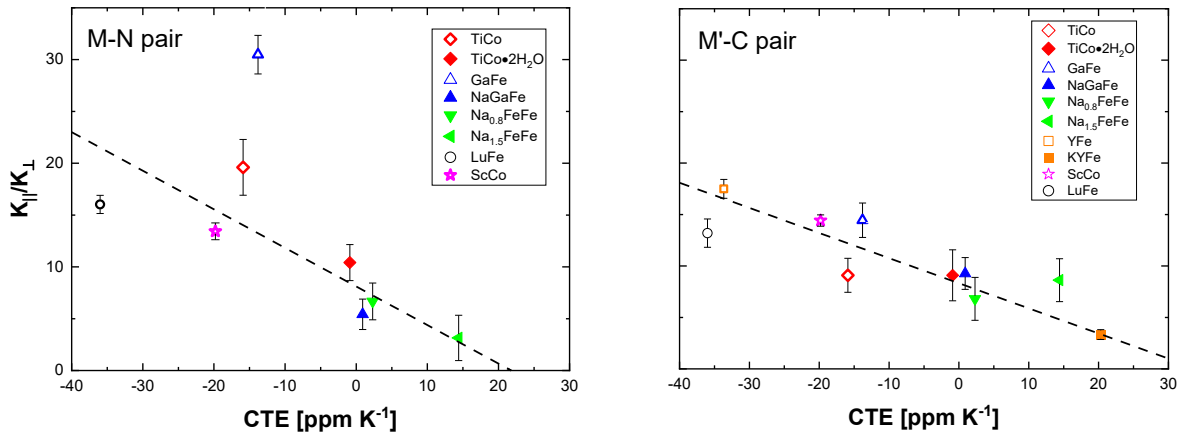


Figure 3.15: The ratio of force constants against the volumetric coefficient of thermal expansion (CTE) for several PBAs for M-N atomic pairs (left) and M'-C atomic pairs (right) with dashed straight lines as guides to the eye

Both theoretical and experimental investigations of series of PBAs differing by the element bound to nitrogen have been performed [17], [14], [18], [7]: $\text{LuFe}(\text{CN})_6$ belongs indeed to a series of rare earth PBAs of brute formula $\text{REFe}(\text{CN})_6$, thus having analyzed its vibrational anisotropy allows to conclude that even in this class of compounds, RE-N vibrations are more important than Fe-C.

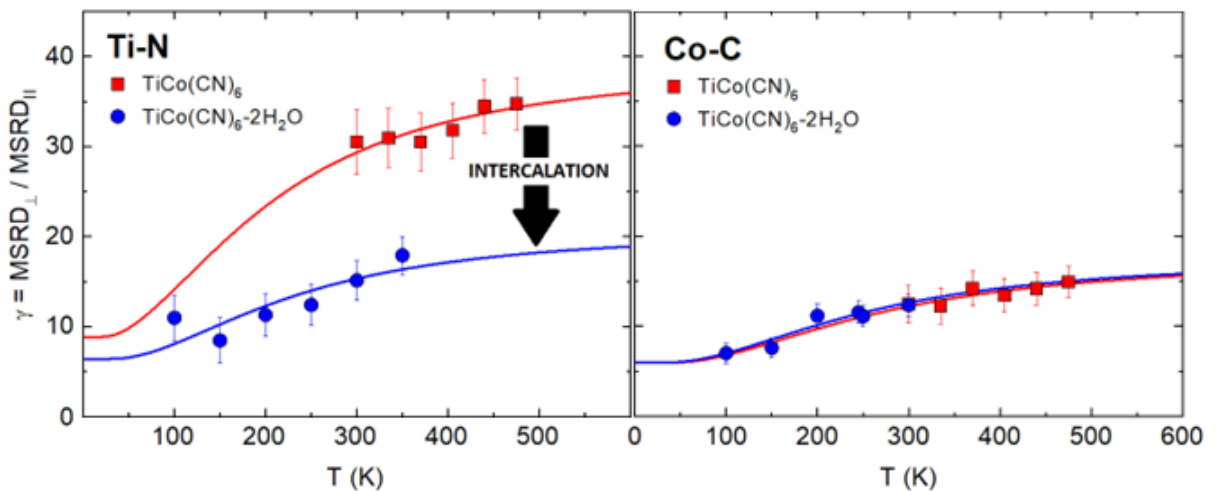


Figure 3.16: Different effect of water intercalation in $\text{TiCo}(\text{CN})_6$ on Ti-N and Co-C atomic pairs vibrational anisotropy

An important role in determining the NTE has been assigned to the ionicity of the M-N bond and the average atomic volume (or the ionic radius of the M specie), however those properties affect NTE indirectly by inhibiting or enhancing M-N transverse vibrations.

Bibliography

- [1] Y. Lu et al., "Prussian blue: a new framework of electrode materials for sodium batteries," *Chem. Commun.*, vol. 48, pp. 6544-6546, 2012.
- [2] S. Kjeldgaard et al., "Strategies for synthesis of Prussian blue analogues," *R. Soc. Open Sci.*, vol. 8, p. 201779, 2021.
- [3] K. Hurlbutt et al., "Prussian Blue Analogs as Battery Materials," *Joule*, vol. 2, no. 10, pp. 1950-1960, 2018.
- [4] K. Itaya et al., "Electrochemistry of Polynuclear Transition Metal Cyanides: Prussian Blue and Its Analogues," *Acc. Chem. Res.*, vol. 19, pp. 162-168, 1986.
- [5] J. Chen et al., "Prussian blue, its analogues and their derived materials for electrochemical energy storage and conversion," *Energy Storage Materials*, vol. 25, pp. 585-612, 2020.
- [6] C. Wang et al., "Large and tunable negative thermal expansion induced by a synergistic effect in $M2II[MIV(CN)8]$ Prussian blue analogues," *Phys. Chem. Chem. Phys.*, vol. 22, pp. 18655-18662, 2020.
- [7] K. W. Chapman et al., "Compositional Dependence of Negative Thermal Expansion in the Prussian Blue Analogues $MII PtIV(CN)6$ ($M = Mn, Fe, Co, Ni, Cu, Zn, Cd$)," *J. Am. Chem. Soc.*, vol. 128, no. 21, pp. 7009-7014, 2006.
- [8] N. Shi et al., "Negative thermal expansion in cubic $FeFe(CN)6$ Prussian blue analogues," *Dalton Trans.*, vol. 48, pp. 3658-3663, 2019.
- [9] S. Adak et al., "Thermal expansion in 3d-metal Prussian Blue Analogs—A survey study," *J. Solid State Chem.*, vol. 184, pp. 2854-2861, 2011.
- [10] S. J. Hibble et al., "Local and Average Structure in Zinc Cyanide: Toward an Understanding of the Atomistic Origin of Negative Thermal Expansion," *J. Am. Chem. Soc.*, vol. 135, p. 16478-16489, 2013.
- [11] F. Herren et al., "Neutron Diffraction Study of Prussian Blue, $Fe_4[Fe(CN)_6]_3 \cdot xH_2O$. Location of Water Molecules and Long-Range Magnetic Order," *Inorg. Chem.*, vol. 19, pp. 956-959, 1980.
- [12] K. Momma and F. Izumi, "VESTA 3 for three-dimensional visualization of crystal, volumetric and morphology data," *J. Appl. Cryst.*, vol. 44, pp. 1272-1276, 2011.

- [13] Q. Gao et al., "Effect of H₂O Molecules on Thermal Expansion of TiCo(CN)₆," *Inorg. Chem.*, vol. 59, no. 20, p. 14852–14855, 2020.
- [14] Q. Gao et al., "The role of average atomic volume in predicting negative thermal expansion: The case of REFe(CN)₆," *Sci. China Mater.*, vol. 65, pp. 553-557, 2022.
- [15] Q. Gao et al., "Tunable Thermal Expansion from Negative, Zero, to Positive in Cubic Prussian Blue Analogues of GaFe(CN)₆," *Inorg. Chem.*, vol. 57, no. 22, pp. 14027-14030, 2018.
- [16] Q. Gao et al., "Low-Frequency Phonon Driven Negative Thermal Expansion in Cubic GaFe(CN)₆ Prussian Blue Analogues," *Inorg. Chem.*, vol. 57, no. 17, pp. 10918-10924, 2018.

Chapter 4

Thermal expansion and local dynamics of zirconium alloys

In this chapter the EXAFS analysis of Zr_2M alloys ($M=Fe, Co, Ni$) is presented. These alloys, characterized by a body-centered tetragonal crystal structure, display a remarkable dependence of the thermal expansion coefficient along the crystalline c -axis from the transition metal indicated with M : α_c is strongly negative for Zr_2Fe , moderately negative for Zr_2Co and even positive for Zr_2Ni . Apart from this striking difference though, the three alloys have analogous crystal structures: this, together with the absence of an ordered magnetic phase allows for a fruitful comparison among the local vibrational dynamics of these alloys to uncover the relevant factors in the mechanism for negative thermal expansion.

4.1 Stoichiometric Zr_2M alloys

The zirconium alloys of stoichiometric composition Zr_2M with M a transition metal ([1], [2]) have been investigated for their relevance to components employed in nuclear power plants [3], for their interesting hydrogen storage properties [4], [5] and for their peculiar superconducting properties [6], [7], [8].

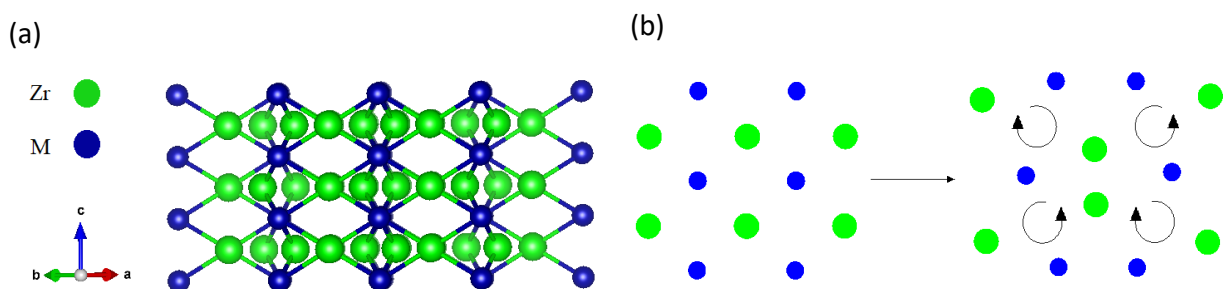


Figure 4.1: (a) Crystal structure of the Zr_2M body centered tetragonal alloys considered in this chapter; (b) breathing mode of the crystal structure highlighting motions of “rigid” units

In addition to these interesting properties, these alloys are also characterized by anomalous thermal expansion properties. Having the same body-centered tetragonal crystal structure, displayed in

Figure 4.1, they allow for an interesting comparison among them, especially considering that the thermal expansion coefficient of the alloys along the *c*-axis strongly depends on the transition metal here indicated as M.

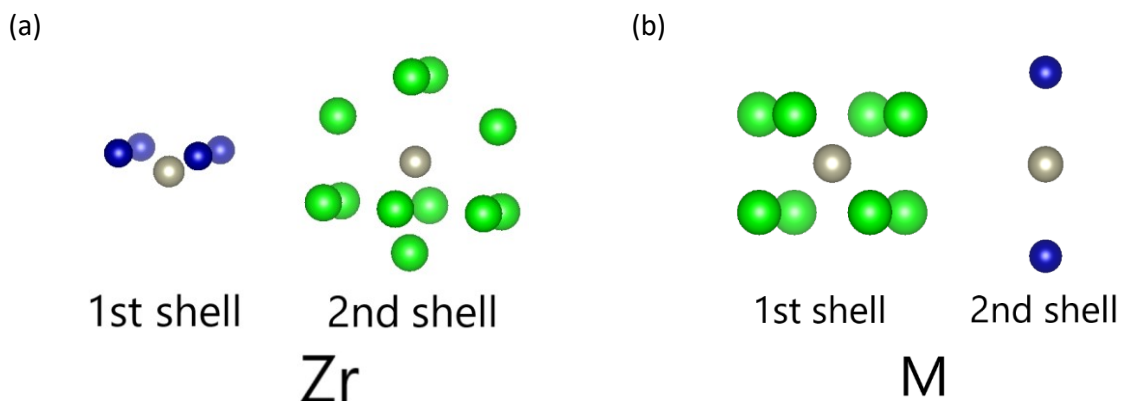


Figure 4.2: Atomic neighborhoods for (a) Zr and (b) M atoms: the first and second atomic shells are portrayed separately, but with the same point of view. The colour code is the same as in Figure 4.1, apart for the absorber atom, which is in grey for clarity.

In this chapter the local vibrational dynamics of the three alloys with M=Fe, Co, Ni have been investigated by temperature-dependent EXAFS spectroscopy. These alloys are interesting due to their different thermal expansion properties, encompassing various possibilities for the coefficient of thermal expansion, from large NTE to PTE. Since they differ mainly by the transition metal M, the study of their local dynamics allows to extract important information, both individually and as a series of compounds.

The local neighborhoods of the two atomic species, Zr and the transition metal (indicated as M), are presented in Figure 4.2. While the treatment of scattering from cobalt atoms doesn't present any complication as they are in crystallographically equivalent positions, the situation is quite different for zirconium atoms, which occupy crystallographically non-equivalent positions: the photoelectron scattering paths don't differ enough to be distinguishable in the EXAFS analysis and thus they have been assigned the same parameters, with the first cumulant weighted with the length of the corresponding path.

The perspective from different edges (M and Zr K-edges) gives a more complete picture and allows to check the self-consistency of the data analysis, i.e., the same physical quantities measured in the two ways must be compatible. However, as will be further detailed in the next sections, the M-M atomic pairs distances are generally similar to those of the M-Zr pairs, which, together with the

significantly smaller contribution to EXAFS scattering (caused by the neat difference in the atomic number), renders the data analysis on the vibrational properties of Fe-Fe atomic pairs unreliable.

4.2 Zr₂Fe

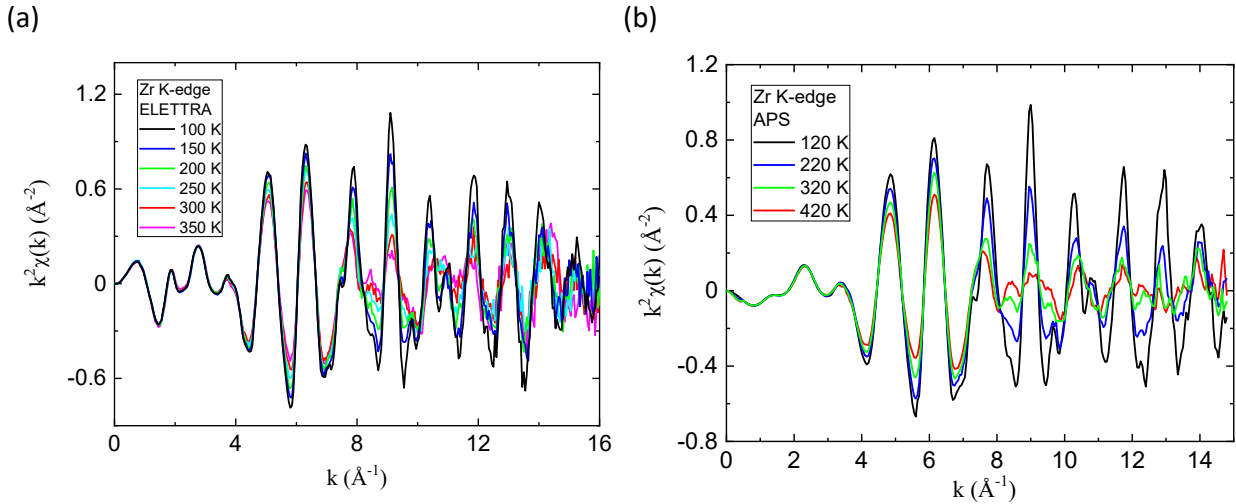


Figure 4.3: $k^2\chi(k)$ signals for Zr₂Fe at Zr K-edge collected at (a) ELETTRA and (b) APS

In the case M=Fe the coefficient of thermal expansion along the c -axis is the most negative of the three alloys ($\alpha_c \approx -37 \text{ ppm} \cdot \text{K}^{-1}$). The XAFS data at the Fe K-edge has been acquired at the ELETTRA synchrotron light facility, while that at the Zr K-edge has been collected in part at the ELETTRA and in part at the APS synchrotron facility by the research group of Prof. Jun Chen.

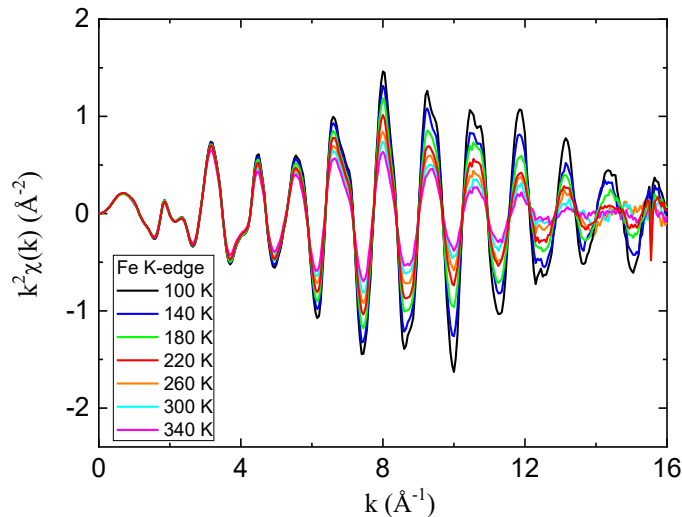


Figure 4.4: $k^2\chi(k)$ signals for Zr₂Fe at Fe K-edge collected at ELETTRA.

The EXAFS spectra (as indicated in Figure 4.3 and Figure 4.4) have been collected at different temperatures using a variable energy step in the extended range, so as to have a constant step in the

momentum of $\Delta k \approx 0.035 \text{ \AA}^{-1}$. The extracted XAFS signals are displayed in Figure 4.3 (Zr K-edge, both datasets) and Figure 4.4 (Fe K-edge). An EXAFS fitting model has been developed performing a FEFF calculation on an atomic cluster built starting from the structural information obtained by the research group of Prof. Jun Chen from diffraction experiments.

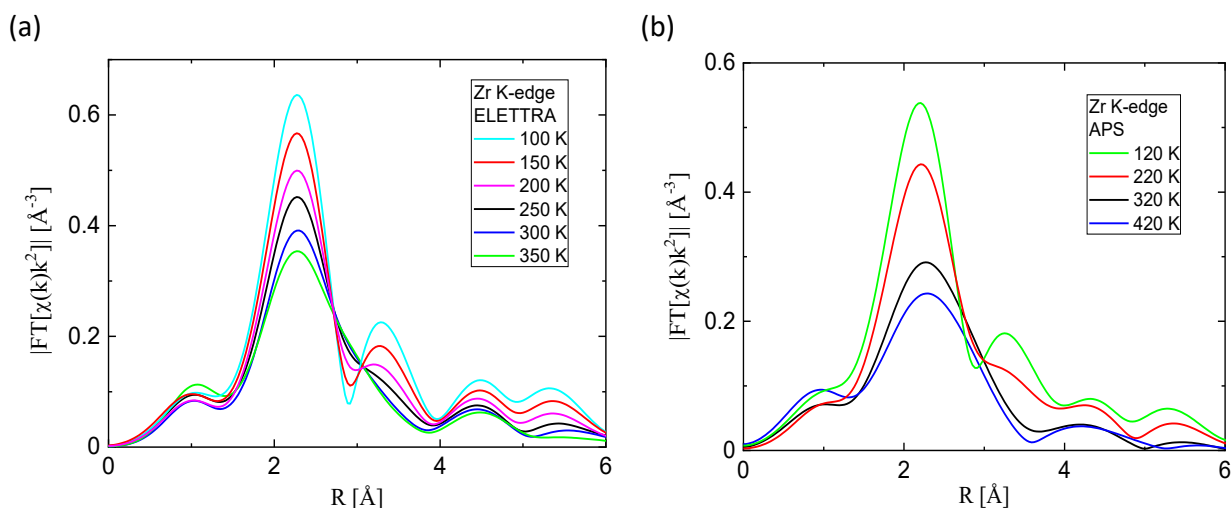


Figure 4.5: Fourier Transform of the k^2 -weighted Zr EXAFS signals vs Temperature collected at (a) ELETTRA and at (b) APS

The resulting scattering paths can be found in Table 4.2 and Table 4.1: in the case of the Fe K-edge, the amplitude due to scattering from zirconium atoms is clearly dominant over that from iron atoms and the two contributing photoelectron paths have similar length, thus making it unfeasible to reliably single out the contribution of the scattering from Fe atoms.

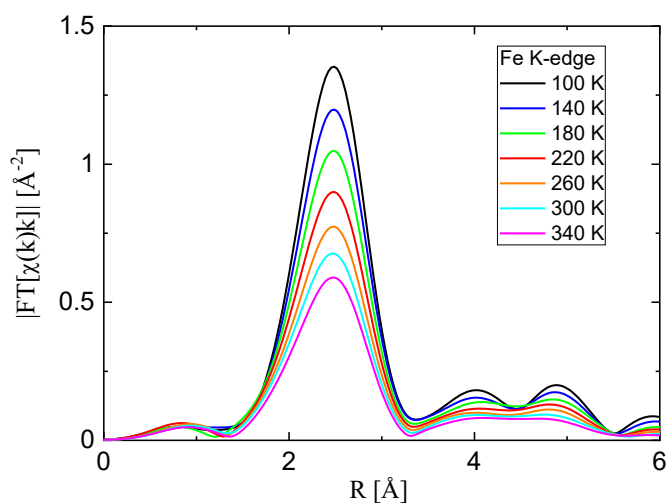


Figure 4.6: Fourier Transform of the k -weighted Fe K-edge EXAFS signals at different temperatures

The first three cumulants have been employed to accurately extract the first cumulant of the first shell at both edges; the higher order shells considered in the fitting have been described with the first two cumulants.

Index	Path	Legs	Degeneracy	r_{eff} [Å]	Amplitude	Parameters
1	Fe-Zr	2	8	2.7290	100.00	r_1, σ_1^2, C_{31}
2	Fe-Fe	2	2	2.7877	18.96	r_2, σ_2^2

Table 4.1: Scattering paths for the EXAFS fitting procedure of Fe K-edge data of Zr_2Fe

Index	Path	Legs	Degeneracy	r_{eff} [Å]	Amplitude	Parameters
1	Zr-Fe	2	4	2.7290	100.00	r_1, σ_1^2, C_{31}
2	Zr-Zr	2	3	3.1091	63.45	r_2, σ_2^2
3	Zr-Zr	2	4	3.3181	71.91	
4	Zr-Zr	2	4	3.5505	60.29	

Table 4.2: Scattering paths for the EXAFS fitting procedure of Zr K-edge data of Zr_2Fe

In Figure 4.5 and Figure 4.6, where the Fourier transforms of the weighted EXAFS signals are reported, the peak structure visible at around $2 \div 2.5 \text{Å}$ consists of the contributions from scattering from both Zr and Fe atoms; it is clearly distinguishable from the signal at higher R values, which is due to scattering from outer atomic shells. Examples of the resulting fits are presented in Figure 4.7.

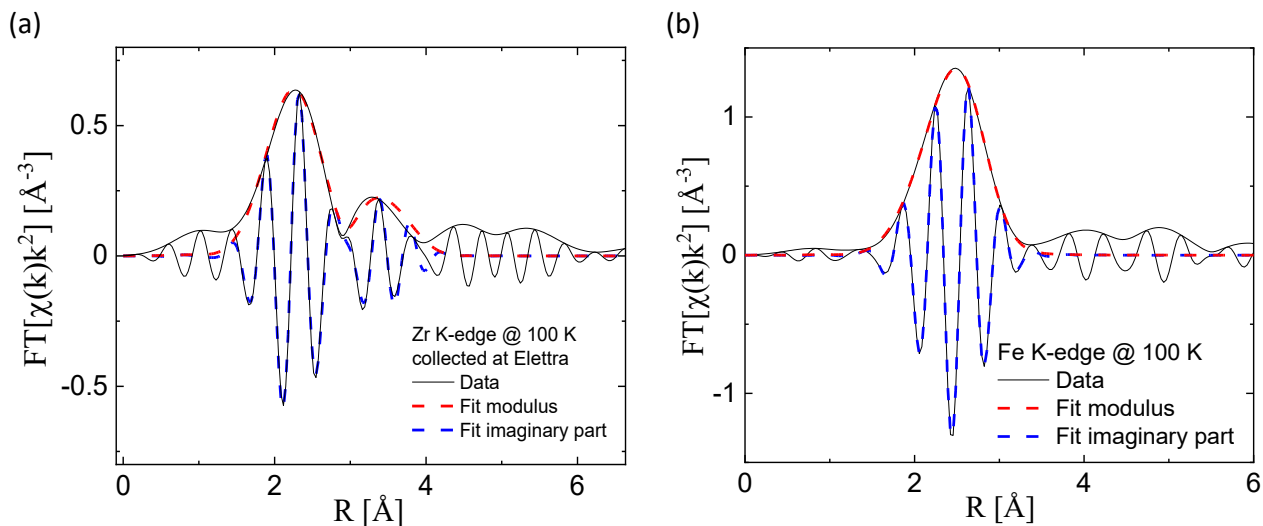


Figure 4.7: Fits of the Fourier transform of the low temperature EXAFS data at (a) Zr K-edge and (b) Fe K-edge

The comparison between the temperature variation with respect to the lowest temperature of the first cumulant (indicated as the “real” distance variation) and the thermal expansion (indicated as the

“apparent” distance variation with temperature and measured by diffraction techniques) of the Zr-Fe atomic pairs is reported in Figure 4.8: as mentioned in the beginning of this chapter, the fact that physical quantities, in this case the first cumulant, obtained from data acquired at different edges, are compatible constitutes an important self-consistency test of the fitting model.

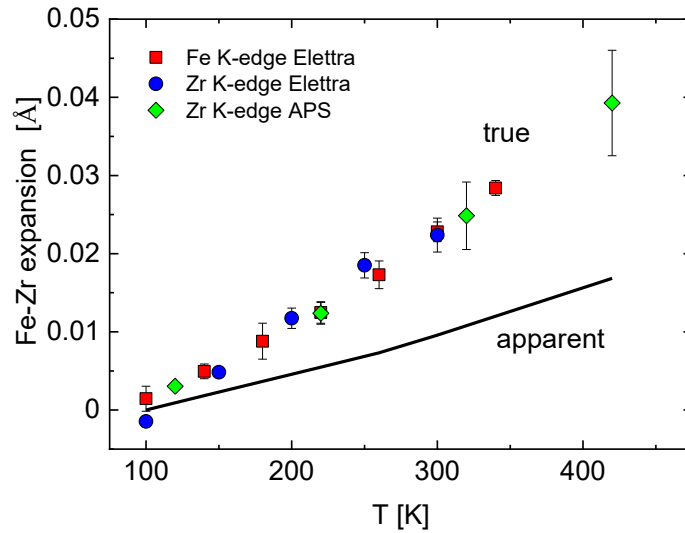


Figure 4.8: Comparison between first cumulant (“true” distance) and thermal expansion (“apparent” distance) for the nearest neighbors Zr-Fe atomic pairs

The MSRDs and the anisotropy of thermal vibrations of Zr-Fe atomic pairs, measured at both the Zr K-edge and the Fe K-edge, are reported in Figure 4.9: as in the case of the first cumulant, the accordance between the results obtained from data at different edges is good.

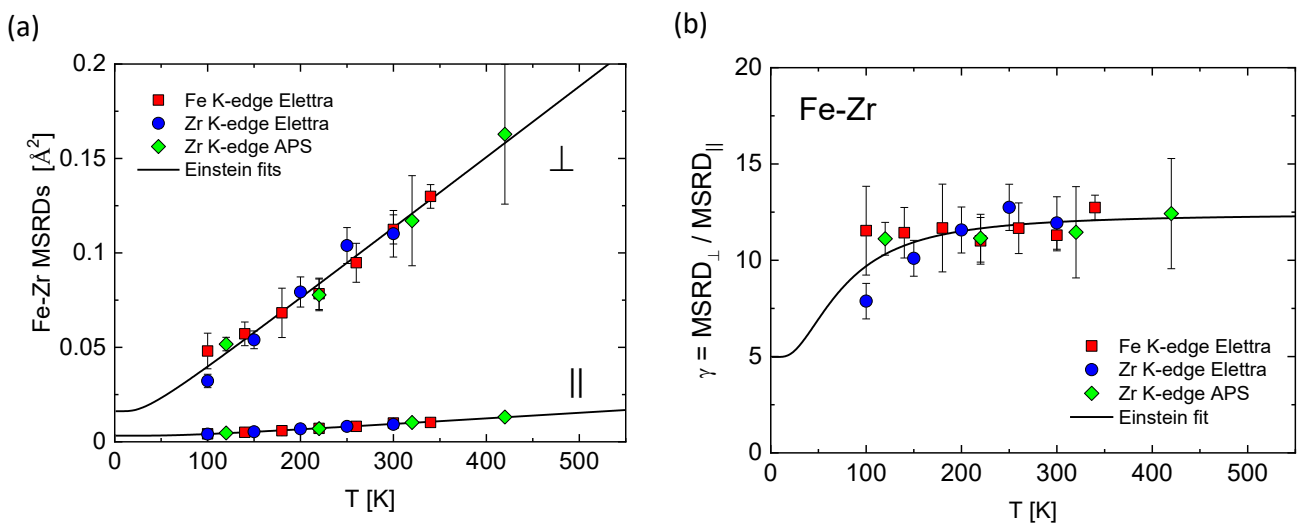


Figure 4.9: (a) MSRDs longitudinal and transverse and (b) anisotropy ratio for the nearest neighbors’ Zr-Fe atomic pairs

The vibrational properties of the Zr-Fe atomic pairs, consisting of the longitudinal and transverse Einstein frequencies and the relative effective force constants can be found in Table 4.3.

Fe-Zr atomic pairs
Stretching $\nu_{\parallel} = 4.41 \pm 0.02$ THz $k_{\parallel} = 2.76 \pm 0.03$ eV/Å ²
Bending $\nu_{\perp} = 1.67 \pm 0.04$ THz $k_{\perp} = 0.40 \pm 0.02$ eV/Å ²
Anisotropy ($2k_{\parallel}/k_{\perp}$) (13.95 ± 0.68)

Table 4.3: Transversal and longitudinal vibrational properties (Einstein frequencies ν and effective force constants κ) of the Fe-Zr nearest neighbors' atomic pairs in Zr₂Fe

4.3 Zr₂Co

In the case M=Co the coefficient of thermal expansion along the c-axis is again negative ($\alpha_c \approx -20$ ppm · K⁻¹), but less than in the Zr₂Fe case.

XAFS data at Co and Zr K-edges has been acquired at the BM08 (LISA) beamline of the ESRF synchrotron light facility. The absorption spectra have been collected at different temperatures using a variable energy step in the extended range, to have a constant step in the momentum of $\Delta k \approx 0.035$ Å⁻¹.

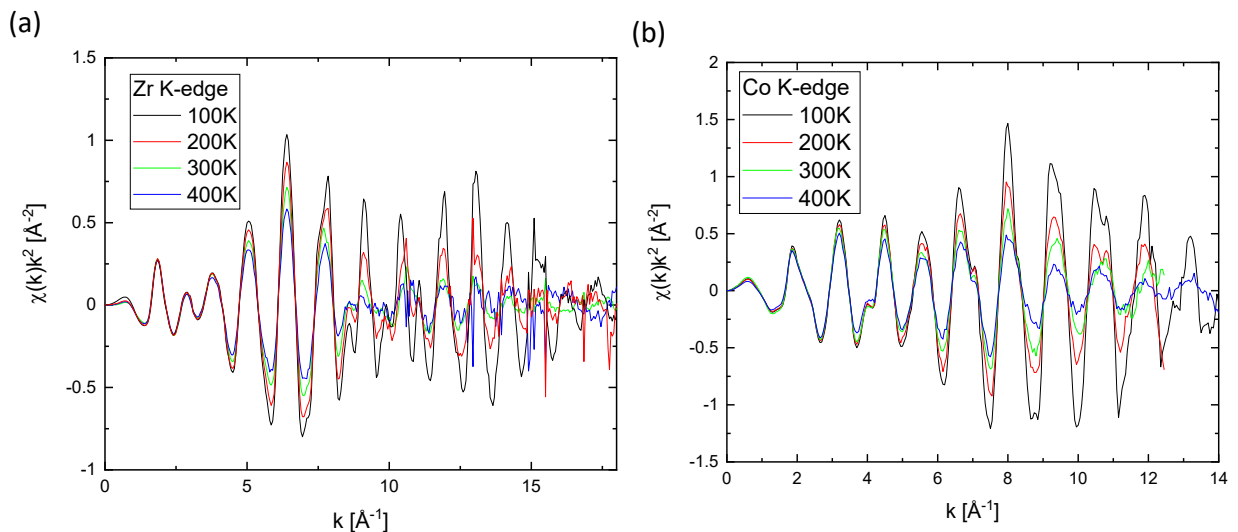


Figure 4.10: $k^2 \chi(k)$ XAFS signals for Zr₂Co at (a) Zr K-edge and (b) Co K-edge

Index	Path	Legs	Degeneracy	r_{eff} [Å]	Amplitude	Parameters
1	Zr->Co->Zr	2	4	2.7347	100	dr_1, C_{21}, C_{31}
2	Zr->Zr->Zr	2	1	3.0672	22.654	dr_2, C_{22}
3	Zr->Zr->Zr	2	2	3.1089	43.840	
4	Zr->Zr->Zr	2	4	3.3394	73.279	
5	Zr->Zr->Zr	2	4	3.5094	64.390	

Table 4.4: Scattering paths for the EXAFS fitting procedure of Zr K-edge data of Zr_2Co

Index	Path	Legs	Degeneracy	r_{eff} [Å]	Amplitude	Parameters
1	Co->Zr->Co	2	8	2.7347	100	dr_1, C_{21}, C_{31}
2	Co->Co->Co	2	2	2.7590	18.667	dr_2, C_{22}

Table 4.5: Scattering paths for the EXAFS fitting procedure of Zr K-edge data of Zr_2Co

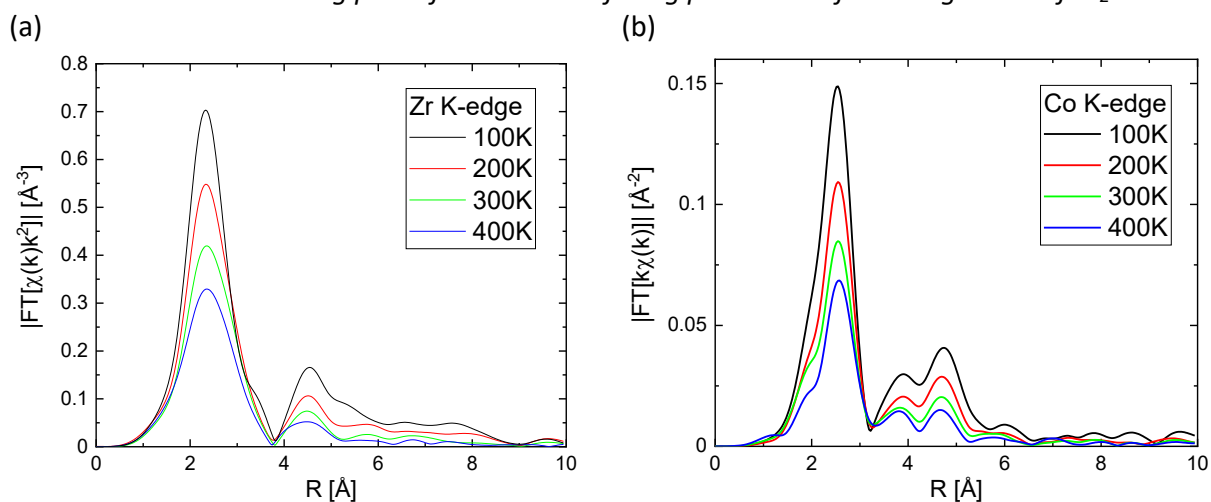


Figure 4.11: Fourier transforms of k^2 -weighted EXAFS data of Zr_2Co at (a) Zr K-edge and (b) Co K-edge

The extracted XAFS signals are displayed in Figure 4.10 (both Zr and Co K-edge): the EXAFS signals, especially at higher temperatures, present a considerable amount of noise in the high- k range, which adds a layer of complication to the overlapping of EXAFS contributions to the first peak due to scattering from both Zr and Co atoms.

FEFF calculations have been performed employing the scattering paths reported in Table 4.4 and Table 4.5: in the case of the Co K-edge the scattering amplitude due to zirconium atoms is dominant over that from cobalt atoms. Also, the scattering amplitudes due to Zr atoms become even more important in the high- k range of the signal, which is also considerably noisy at high temperatures.

To properly treat the fitting procedure and at the same time get rid of unphysical low- R artifacts, the R_{bkg} parameter, used in the background removal procedure, was raised to around 1.3-1.5 and the k -range was chosen with a lower k_{max} of around 13Å^{-1} . An excessive value of the R_{bkg} parameter can

distort the EXAFS signals at low- R , but in this case, due to the relatively long nearest interatomic distances, these concerns are outweighed by the necessity to filter out background and noise.

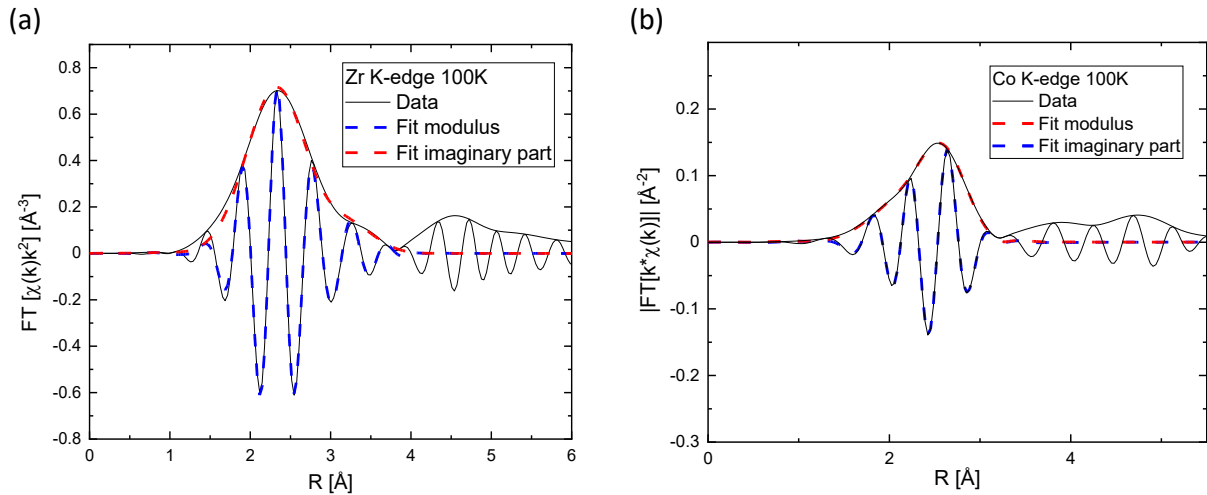


Figure 4.12: Fits of the Fourier transform of the low temperature EXAFS data at (a) Zr K-edge and (b) Co K-edge

The Fourier transform of the XAFS signals are in Figure 4.11: at both edges the first peaks at around $2 \div 2.5 \text{ \AA}$, well distinguishable from the signals at higher- R values, receive contributions from both the scattering from Fe and Zr atoms, though, in the same sense as it was pointed out in the section dedicated to Zr_2Fe , for scattering from Fe atoms, the analysis of Co-Co atomic pairs is unfeasible. Examples of the resulting fits are presented in Figure 4.12.

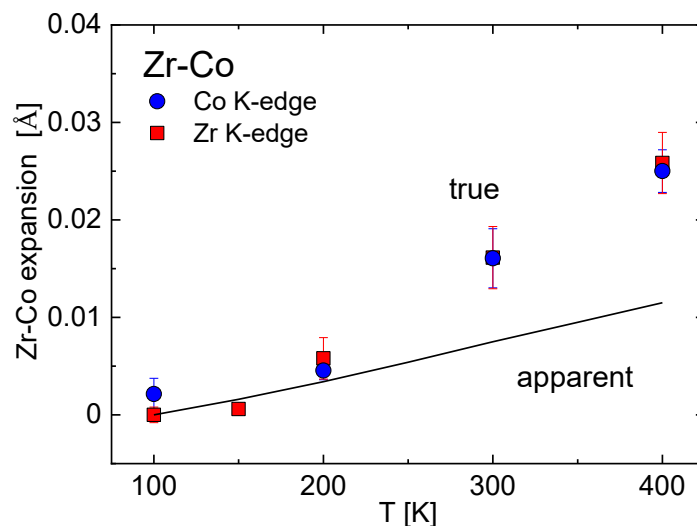


Figure 4.13: Comparison between first cumulant and thermal expansion (continuous line) for the nearest neighbors' Zr-Fe pairs obtained using both the Zr and Co K-edges data

The comparison between the temperature variation with respect to the lowest temperature of the first cumulant and the thermal expansion of the Zr-Co atomic pairs, measured at both Zr K-edge and Co K-edge, is shown in Figure 4.13: the difference between them is employed to estimate the transverse MSRD, which, together with the MSRD_{\parallel} and the anisotropy of the thermal vibrations of Zr-Co atomic pairs can be found in Figure 4.14.

As in the case of Zr_2Fe , there is good compatibility between analogous quantities calculated at different edges. A summary of the vibrational properties characterizing the anisotropy of thermal vibrations of Zr-Co atomic pairs is presented in Table 4.6.

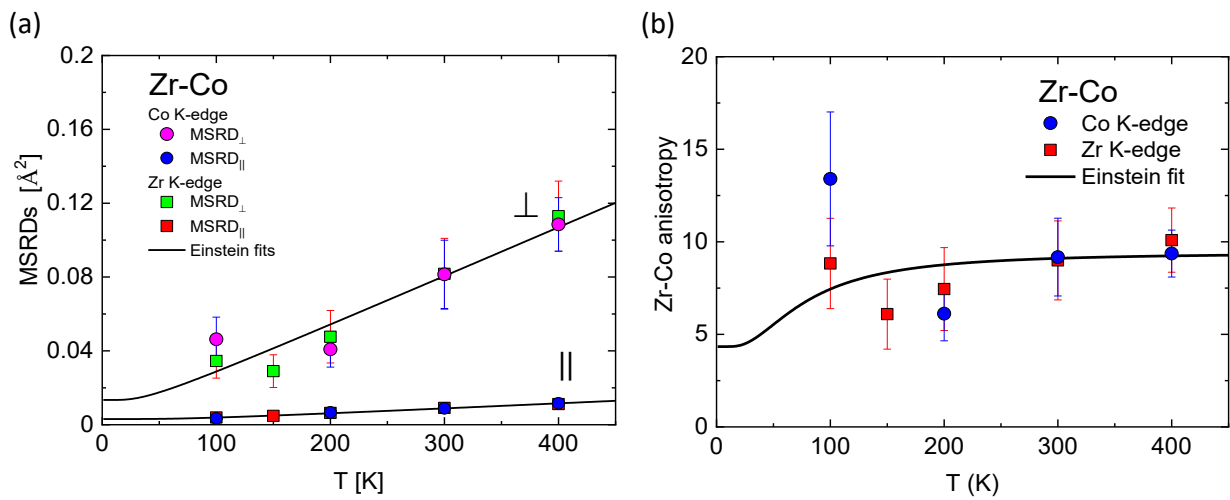


Figure 4.14: (a) MSRDs longitudinal and transverse and (b) anisotropy ratio for the nearest neighbors' Zr-Co atomic pairs

<u>Zr-Co atomic pairs</u>
Stretching $\nu_{\parallel} = (4.56 \pm 0.08)\text{THz}$ $k_{\parallel} = (3.05 \pm 0.10)\text{eV} \cdot \text{\AA}^{-2}$
Bending $\nu_{\perp} = (2.10 \pm 0.13)\text{THz}$ $k_{\perp} = (0.65 \pm 0.08)\text{eV} \cdot \text{\AA}^{-2}$
Anisotropy $2 k_{\perp}/k_{\parallel} = (9.4 \pm 1.2)$

Table 4.6: Transversal and longitudinal vibrational properties (Einstein frequencies ν and effective force constants κ) of the Co-Zr nearest neighbors' atomic pairs in Zr_2Co

4.4 Zr₂Ni

If M=Ni the coefficient of thermal expansion along the *c*-axis is instead positive ($\alpha_c \approx 4 \text{ ppm} \cdot \text{K}^{-1}$). As in the case of Zr₂Co, the XAFS data at Ni and Zr K-edges has been acquired at the BM08 (LISA) beamline of the ESRF synchrotron light facility. The EXAFS spectra have been collected at different temperatures using a variable energy step in the extended range, so to have a constant step in the momentum of $\Delta k \approx 0.035 \text{ \AA}^{-1}$.

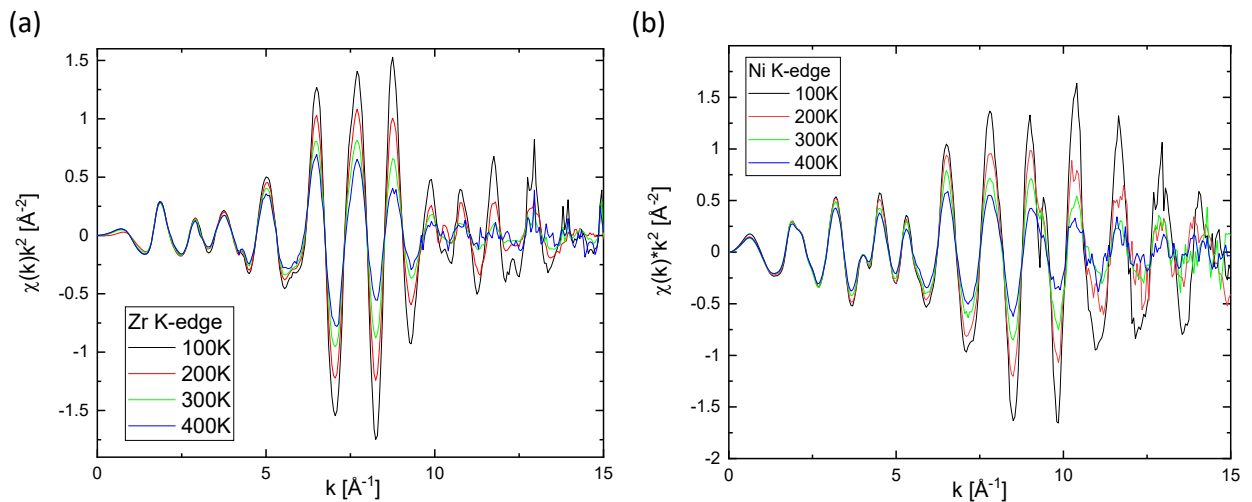


Figure 4.15: $k^2\chi(k)$ XAFS signals for Zr₂Ni at (a) Zr K-edge and (b) Ni K-edge

The extracted XAFS signals are displayed in Figure 4.15 (both Zr and Ni K-edge). As in the case of Zr₂Co, a proper treatment of the noisy high-*k* range of the EXAFS signals has been performed raising the R_{bkg} parameter and lowering the k_{max} for the EXAFS fitting procedure.

Index	Path	Legs	Degeneracy	r_{eff} [Å]	Amplitude	Parameters
1	Ni->Ni->Ni	2	2	2.6335	100	dr_2, C_{22}
2	Ni->Zr->Ni	2	8	2.7611	495.947	dr_1, C_{21}, C_{31}

Table 4.7: Scattering paths for the EXAFS fitting procedure of Zr K-edge data of Zr₂Ni

Index	Path	Legs	Degeneracy	r_{eff} [Å]	Amplitude	Parameters
1	Zr->Ni->Zr	2	4	2.7611	100	C_{11}, C_{21}, C_{31}
2	Zr->Zr->Zr	2	1	2.9889	25.526	C_{12}, C_{22}
3	Zr->Zr->Zr	2	2	3.0790	47.512	
4	Zr->Zr->Zr	2	4	3.3767	75.338	
5	Zr->Zr->Zr	2	4	3.4322	72.210	

Table 4.8: Scattering paths for the EXAFS fitting procedure of Zr K-edge data of Zr₂Ni

FEFF calculations have been performed employing the scattering paths reported in Table 4.8 and

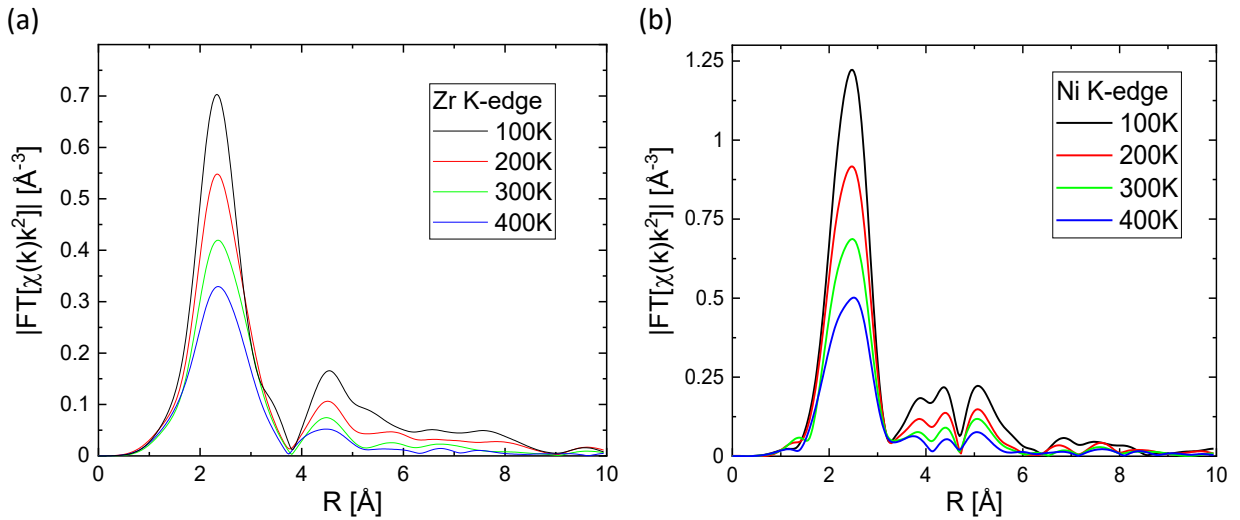


Figure 4.16: Fourier transforms of k^2 -weighted EXAFS data of Zr_2Ni at (a) Zr K-edge and (b) Ni K-edge

Table 4.7: in the case of the Ni K-edge the scattering amplitude due to zirconium atoms is again dominant over that from nickel atoms. The Fourier transform of the XAFS signals are in Figure 4.16 and examples of the resulting fits are presented in Figure 4.17.

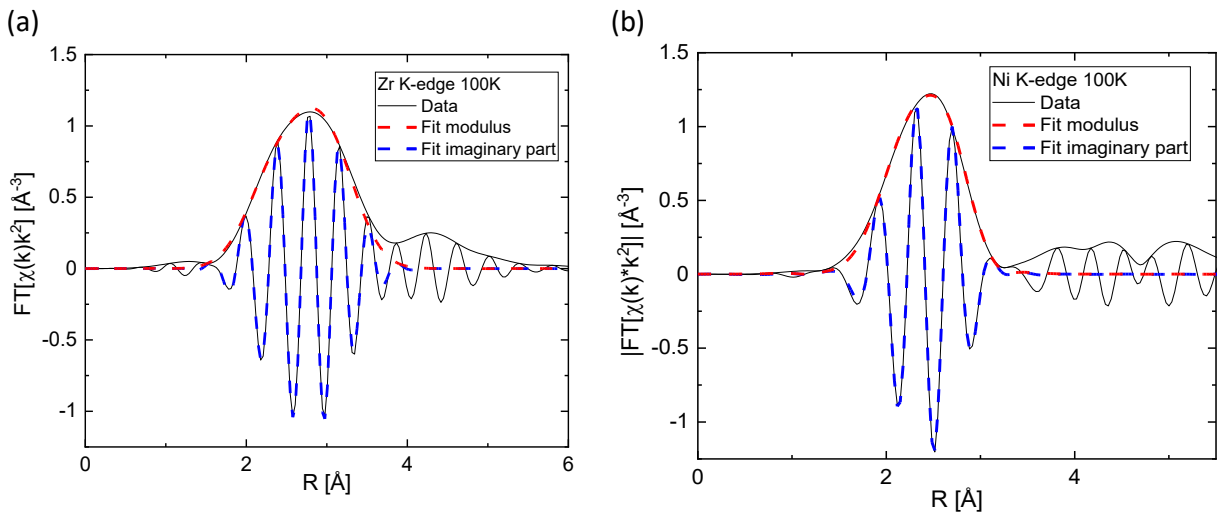


Figure 4.17: Fits of the Fourier transform of the low temperature EXAFS data at (a) Zr K-edge and (b) Ni K-edge

The comparison between temperature variation of the first cumulant and the thermal expansion is in Figure 4.18: it is worth noting that they are well compatible at most of the investigated temperatures, clearly indicating that transverse vibrations of Zr-Ni are significantly smaller than in the case of the other alloys. This is also clear from Figure 4.19, where the MSRDS and the anisotropy

for Zr K-edge and Ni K-edge are reported, considering that the anisotropy is considerably closer to the isotropic value ($\gamma=2$) than the other alloys. Quantities obtained at different edges are compatible.

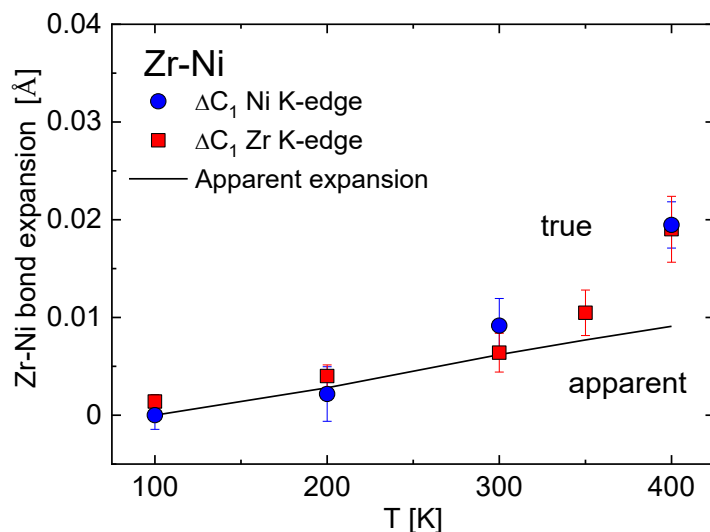


Figure 4.18: Comparison between first cumulant and thermal expansion for the nearest neighbors' (a) Zr-Fe pairs obtained using both the Zr and Ni K-edges data

Vibrational anisotropy properties of the Ni-Zr atomic pairs are reported in Table 4.9; the fact that uncertainties on these quantities are greater than in the two previous cases is mainly due to two factors: the considerable amount of noise present in the EXAFS spectra, but also the transverse vibrations being smaller renders the estimate of the $MSRD_{\perp}$ less accurate.

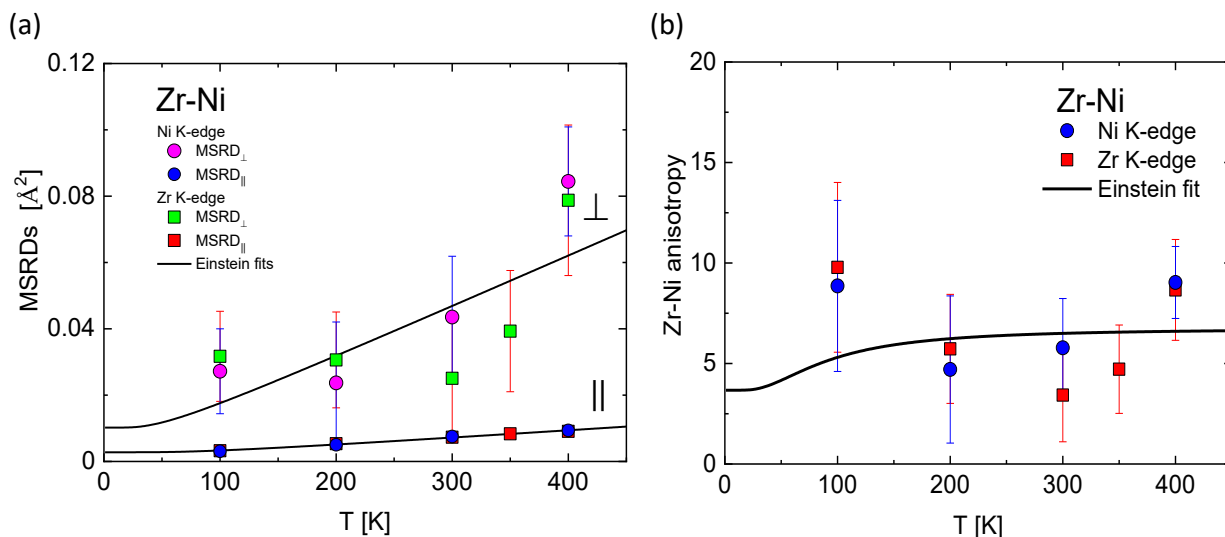


Figure 4.19: (a) MSRDS longitudinal and transverse and (b) anisotropy ratio for the nearest neighbors' Zr-Ni atomic pairs

Zr-Ni atomic pairs
Stretching $\nu_{\parallel} = (5.08 \pm 0.07) \text{THz}$ $k_{\parallel} = (3.78 \pm 0.10) \text{eV} \cdot \text{\AA}^{-2}$
Bending $\nu_{\perp} = (2.77 \pm 0.44) \text{THz}$ $k_{\perp} = (1.12 \pm 0.35) \text{eV} \cdot \text{\AA}^{-2}$
Anisotropy $2 k_{\parallel}/k_{\perp} = (6.7 \pm 2.2)$

Table 4.9: Transversal and longitudinal vibrational properties (Einstein frequencies ν and effective force constants κ) of the Ni-Zr nearest neighbors' atomic pairs in Zr_2Ni

4.5 Discussion and conclusions

The zirconium alloys of stoichiometric composition Zr_2M that have been subjected to EXAFS investigations encompass the various possibilities of coefficient of thermal expansion values from those of large NTE to PTE passing through intermediate values, with the main difference among them being the transition metal, here indicated with M.

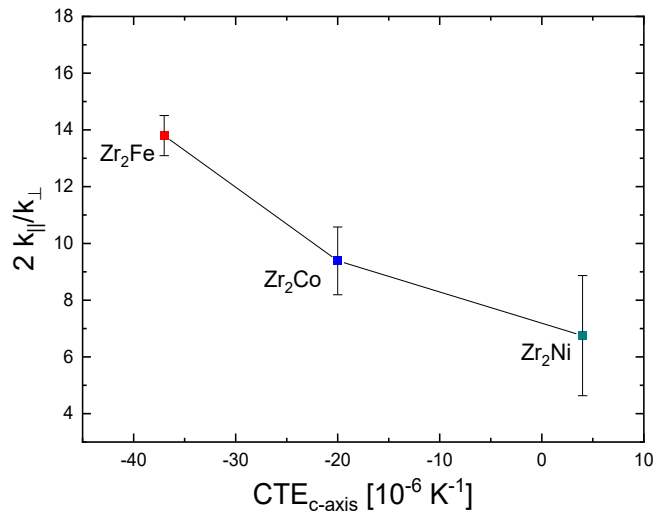


Figure 4.20: Anisotropy for the three alloys compared to the respective thermal expansion coefficient along the c-axis

Since the crystal structure is very similar for the three alloys with $\text{M}=\text{Fe}, \text{Co}, \text{Ni}$, the comparison among them is physically motivated and is relatively simple and clear, allowing to extract important information regarding the relation between vibrational anisotropy, the coefficient of thermal expansion and the crystal structure.

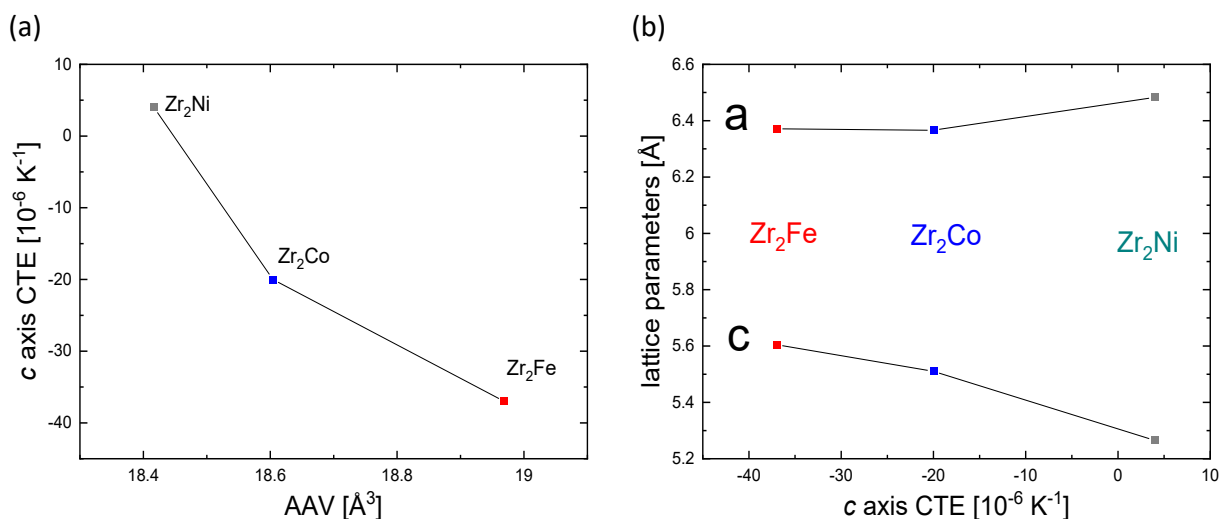


Figure 4.21: Comparison between the CTE and (a) the AAV and (b) the lattice parameters (measured by SXRD at around 0°C by the research group of Prof. Jun Chen)

Thus, in Figure 4.20 the CTE along the c -axis has been plotted against the vibrational anisotropy of thermal vibrations of Zr-M atomic pairs: a negative correlation between the two quantities is observed, consistently with the results obtained for the compound family of Prussian blue analogues and presented in the previous chapter. This suggests a phononic nature of the NTE mechanism, similarly to many other framework structured compounds.

Other factors are worth mentioning: the absence of an ordered magnetic phase in these alloys strengthens the presented results and, together with the presence of breathing modes, further supports the indication of the phononic NTE mechanism in this class of alloys.

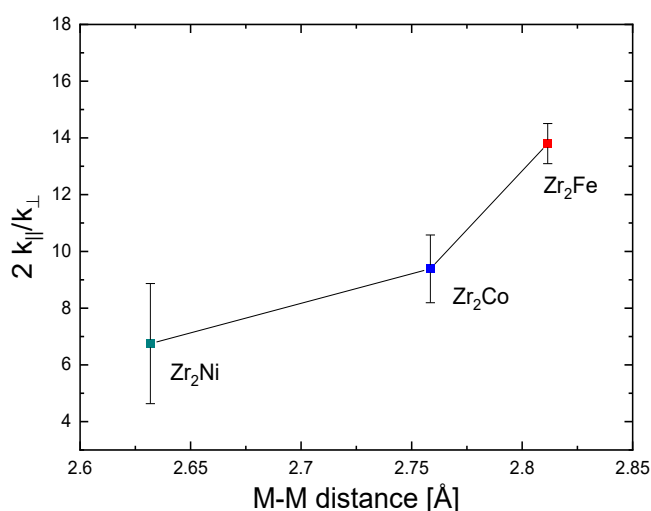


Figure 4.22: The ratio of the effective force constants and the M-M distance (measured by SXRD at around 200K by the research group of Prof. Jun Chen)

Following the investigation conducted in [95], the role of the AAV in materials with anisotropic thermal expansion is of great interest due to the high number of such systems, at least with respect to those with isotropic thermal expansion. These results indicate that, even in this case, the AAV seems to be relevant to NTE; in Figure 4.21, the comparison between the CTE along the c -axis and the average atomic volume (AAV) is presented: it displays a negative correlation between the two quantities, as in the case of PBAs and other classes of compounds [10].

However, we have to mention that while the CTE along the c -axis is strongly dependent on the transition metal M , the volumetric CTE is instead positive for all of the investigated alloys; thus, it seems more natural to compare the c lattice parameter to the CTE along the c -axis. Indeed, as can be also seen in Figure 4.21, where the lattice parameters are plotted, a correlation is indeed found also between the $\text{CTE}_{c\text{-axis}}$ and the c lattice parameter; this, together with the absence of a similar clear trend for the a lattice parameter of the alloys, suggests that even if the concept of AAV may still be applicable to strongly anisotropic materials, an evaluation involving the lattice parameters seems to be in general required.

To further clarify and corroborate the previous considerations, in Figure 4.22 the comparison is made between the anisotropy of thermal vibrations, quantified using the ratio of the effective force constants, and the M-M distances, which is related to the c lattice parameter in these alloys by a proportionality relation: consistently with what has been reported so far, these two quantities are positively correlated.

Bibliography

- [1] D. Arias and J. P. Abriata, "The Fe-Zr (Iron-Zirconium) System," *Bulletin of alloy phase diagrams*, vol. 9, no. 5, pp. 597-604, 1988.
- [2] F. Stein et al., "Experimental Determination of Intermetallic Phases, Phase Equilibria, and Invariant Reaction Temperatures in the Fe-Zr System," *Journal of Phase Equilibria*, vol. 23, no. 6, pp. 480-494, 2002.
- [3] G. Kuri et al., "Micro-focussed XAFS spectroscopy to study Ni-bearing precipitates in the metal of corroded Zircaloy-2," *Appl. Phys. A*, vol. 98, pp. 625-633, 2010.
- [4] M. Hara et al., "Hydrogen-induced disproportionation of Zr₂M (M=Fe, Co, Ni) and reproporationation," *Journal of Alloys and Compounds*, vol. 352, no. 1-2, pp. 218-225, 2003.
- [5] L. Han et al., "Hydrogen storage properties of Zr₂Co crystalline and amorphous alloys," *Int. J. of Hydrogen Energy*, vol. 46, pp. 2312-2321, 2021.
- [6] B. T. Matthias and E. Corenzwit, "Superconductivity of Zirconium Alloys," *Phys. Rev.*, vol. 100, no. 2, p. 626, 1955.
- [7] R. Mittal et al., "Electrons, phonons and superconductivity in C16 structured Zr₂Fe," *Physica C*, vol. 320, pp. 239-244, 1999.
- [8] R. Mittal et al., "Phonon density of states in Zr₂Ni," *Physica B*, vol. 222, pp. 233-237, 1996.
- [9] Q. Gao et al., "The role of average atomic volume in predicting negative thermal expansion: The case of REFe(CN)₆," *Sci. China Mater.*, vol. 65, pp. 553-557, 2022.
- [10] Q. Gao et al., "Discovering Large Isotropic Negative Thermal Expansion in Framework Compound AgB(CN)₄ via the Concept of Average Atomic Volume," *J. Am. Chem. Soc.*, vol. 142, no. 15, p. 6935-6939, 2020.

Chapter 5

Chemical substitution and local dynamics of copper pyrophosphate analogues

In this chapter, the EXAFS analysis of compounds analogous to copper pyrophosphate $\text{Cu}_2\text{P}_2\text{O}_7$ is reported. Their facile and inexpensive production processes opened up avenues for applications. We will report on two interesting examples, $\text{Cu}_2\text{V}_2\text{O}_7$ and $\text{Cu}_{1.25}\text{Zn}_{0.75}\text{P}_2\text{O}_7$: substituting the Cu and the P with respectively Zn and V allows to investigate the difference between the resulting samples, which display moderately or mildly negative thermal expansion, and $\text{Cu}_2\text{P}_2\text{O}_7$, which instead has large negative thermal expansion over a wide temperature range. The crucial role of EXAFS is to highlight the different roles played by the thermal vibrations of Cu/Zn-O and V-O atomic pairs and the effect on the local vibrational dynamics by the chemical substitution.

5.1 Copper pyrophosphate analogues

A number of compounds with the brute formula $\text{A}_2\text{M}_2\text{O}_7$, analogue to copper pyrophosphate ($\text{Cu}_2\text{P}_2\text{O}_7$), have been found to exhibit anomalous thermal expansion properties [1], [2], [3], [4], [5], [6], [7], [8], [9], [10], [11], [12], [13].

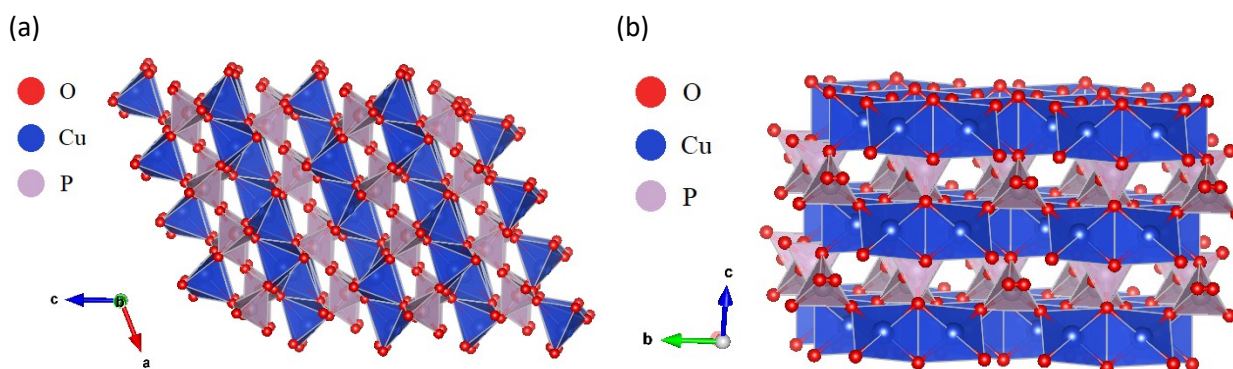


Figure 5.1: Crystal structures of (a) α -phase; (b) β -phase of $\text{Cu}_2\text{P}_2\text{O}_7$

The relevance of $\text{Cu}_2\text{P}_2\text{O}_7$ and its chemical analogues stems from its facile and inexpensive synthesis process, at least when compared to many other large NTE compounds the cost of which is strongly influenced by the heavy metals or rare-earths that they contain and which can also make them toxic.

The availability of these compounds opens opportunities for applications: composite materials have been investigated in this regard [1], making it possible to tame the high thermal expansion of epoxy by mixing it with copper pyrophosphate, obtaining epoxy composites of significantly lower coefficient of thermal expansion (see [14] for a review of composite containing NTE materials).

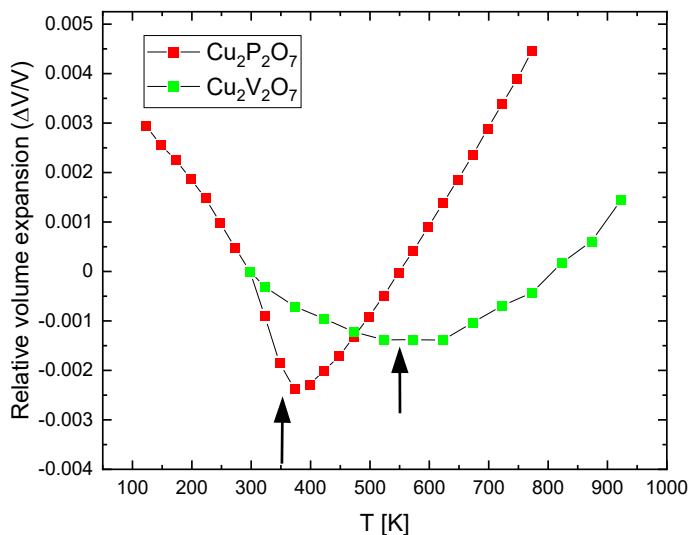


Figure 5.2: Relative thermal expansion of $\text{Cu}_2\text{P}_2\text{O}_7$ and $\text{Cu}_2\text{V}_2\text{O}_7$, highlighting the difference in the polymorphic transition temperatures (indicated approximately by the arrows) and of the thermal expansion itself.

The structure of the two polymorphs of $\text{Cu}_2\text{P}_2\text{O}_7$ is shown in Figure 5.1. Even if quite involved, it can be broken down to fundamental units, the MO_4 tetrahedra, two by two linked by an oxygen atom to form the pyrophosphate units M_2O_7 , and the AO_5 units two by two sharing an O-O edge, forming a layered structure. The rocking modes of these units, mainly involving large vibrations of oxygen linking atoms transverse to their bond directions with metal atoms, are a plausible candidate for the NTE mechanism in $\text{Cu}_2\text{P}_2\text{O}_7$. The low-temperature α -phase (with $\text{C2}/c$ symmetry) is the one displaying the anomalous thermal expansion properties, while the high-temperature β -phase (with $\text{C2}/m$ symmetry) shows normal thermal expansion coefficient.

Some of the analogues of $\text{Cu}_2\text{P}_2\text{O}_7$ display different crystal symmetry, but retain the MO_4 and AO_5 units; thus, it can be expected that those fundamental units partake in the NTE mechanism.

The EXAFS spectroscopy of these compounds is complicated by three factors: it is unfeasible to obtain EXAFS spectroscopy data at the P K-edge due to it being at too low energy, the complicated local atomic neighborhoods around both A and M atomic sites and the presence of the alpha to beta phase transition.

The first point is mitigated by studying copper pyrophosphates in which the phosphorus is partially substituted by a heavier element with the same valence state (in this case vanadium will be

employed), the second will be accounted for in the following sections regarding the EXAFS data analysis and the third one requires a different treatment of the photoelectron scattering processes for each phase.

5.2 $\text{Cu}_2\text{V}_2\text{O}_7$

The $A=\text{Cu}$ and $M=\text{V}$ pyrophosphate analogue, i.e. $\text{Cu}_2\text{V}_2\text{O}_7$, is a compound that shows volumetric NTE and a highly anisotropic linear thermal expansion ($\alpha_a \approx 1.5 \cdot 10^{-6} \text{ K}^{-1}$, $\alpha_b \approx -17.44 \cdot 10^{-6} \text{ K}^{-1}$, $\alpha_c \approx 5.8 \cdot 10^{-6} \text{ K}^{-1}$,

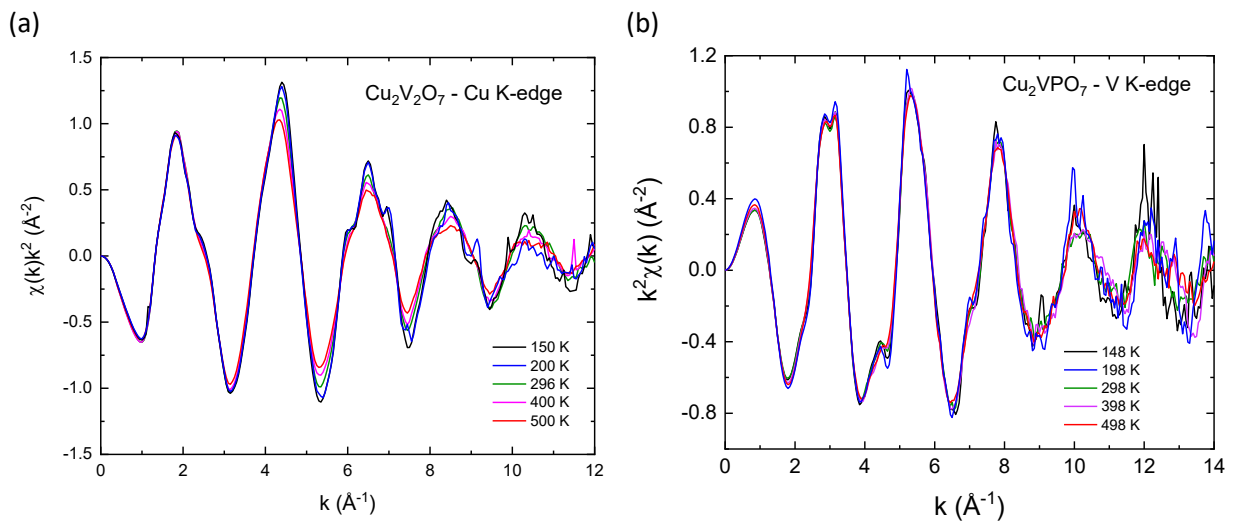


Figure 5.3: Weighted EXAFS signals of $\text{Cu}_2\text{V}_2\text{O}_7$ measured at the (a) Cu K-edge and (b) V K-edge

$\alpha_v \approx -10.19 \cdot 10^{-6} \text{ K}^{-1}$). A comparison with $\text{Cu}_2\text{P}_2\text{O}_7$ regarding the volumetric NTE is drawn in Figure 5.2. There is a difference between the crystal phase transition temperatures (which however are between different crystal symmetries for the two compounds); also, the extent of the thermal expansion itself is considerably different.

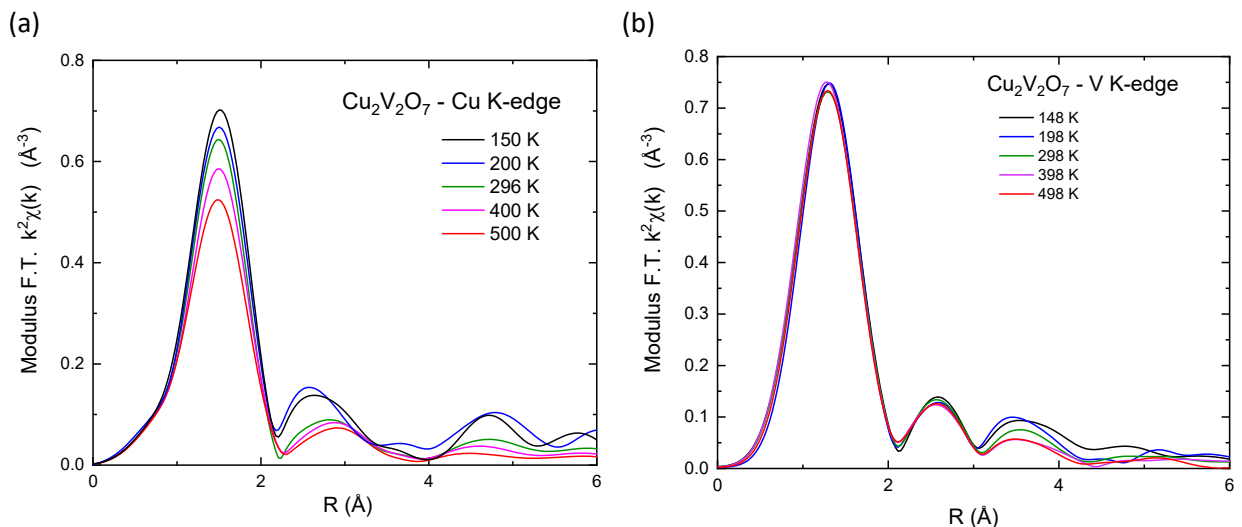


Figure 5.4: Fourier transforms of the weighted EXAFS signals of $\text{Cu}_2\text{V}_2\text{O}_7$ at the (a) Cu K-edge and (b) V K-edge

Index	Path	Legs	Degeneracy	r_{eff} (Å)	Amplitude	Parameters
1	$\text{Cu} - \text{O}_1$	2	1	1.8820	100.00	r_1, σ_1^2, C_3
2	$\text{Cu} - \text{O}_2$	2	1	1.9328	93.68	
3	$\text{Cu} - \text{O}_3$	2	1	1.9515	91.49	
4	$\text{Cu} - \text{O}_4$	2	1	1.9671	89.73	
5	$\text{Cu} - \text{O}_5$	2	1	2.5326	47.880	Neglected

Table 5.1: Shortest scattering paths and amplitudes for $\text{Cu}_2\text{V}_2\text{O}_7$ at Cu K-edge as calculated with the FEFF software

Index	Path	Legs	Degeneracy	r_{eff} (Å)	Amplitude	Parameters
1	$\text{V} - \text{O}_1$	2	1	1.6251	100.00	r_1, σ_1^2, C_3
2	$\text{V} - \text{O}_2$	2	1	1.6899	91.20	
3	$\text{V} - \text{O}_3$	2	1	1.7368	85.49	
4	$\text{V} - \text{O}_4$	2	1	1.8061	77.96	

Table 5.2: Shortest scattering paths and amplitudes for $\text{Cu}_2\text{V}_2\text{O}_7$ at V K-edge as calculated with the FEFF software

Its crystal structure has an orthorhombic (space group $Fdd2$) symmetry in its alpha phase, that presents volumetric NTE up to 500K. Having substituted the phosphorus with vanadium gives the opportunity to investigate both A and M-sites, which would otherwise be unfeasible due to the P K-edge being at too low energy: XAS data has been acquired at the XAFS beamline of the ELETTRA synchrotron light facility at both the Cu and V K-edges.

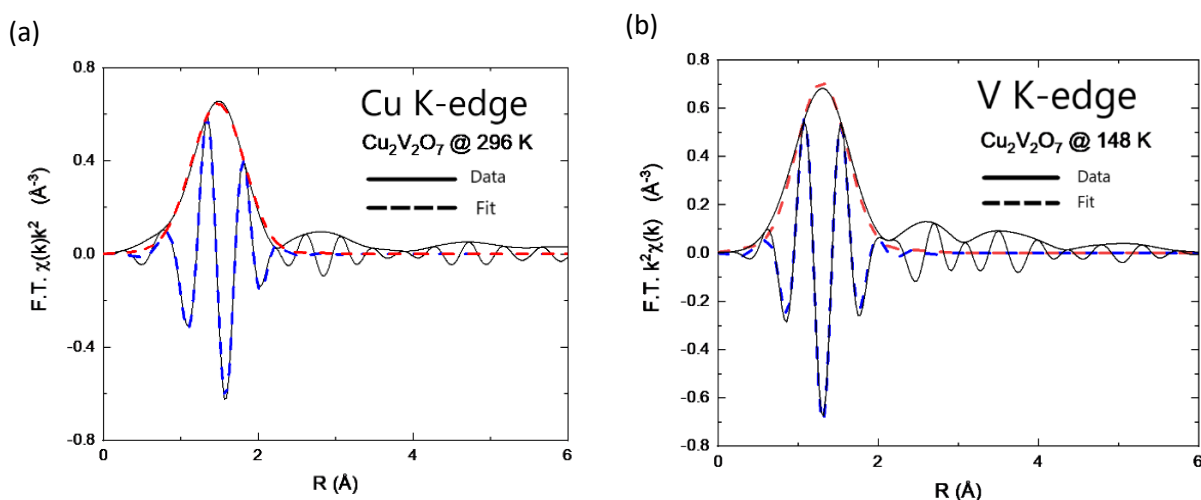


Figure 5.5: Examples of fits of the Fourier transforms of the EXAFS signals at the (a) Cu K-edge and (b) V K-edge. In both graphs the dashed lines represent the fitting curves (blue is the imaginary part, red the modulus), while the continuous lines are the Fourier transform of the k^2 -weighted EXAFS signals data.

Various spectra have been measured at different temperatures in the range 148-498K at regular intervals of 50K; the extracted weighted EXAFS signals are reported in Figure 5.3. The crystal structure information obtained by the research group of Prof. Jun Chen using diffraction techniques has been employed as input for FEFF calculations of the scattering amplitudes, which are reported in Table 5.2 and Table 5.1, together with the paths that have been considered for the EXAFS fitting procedure.

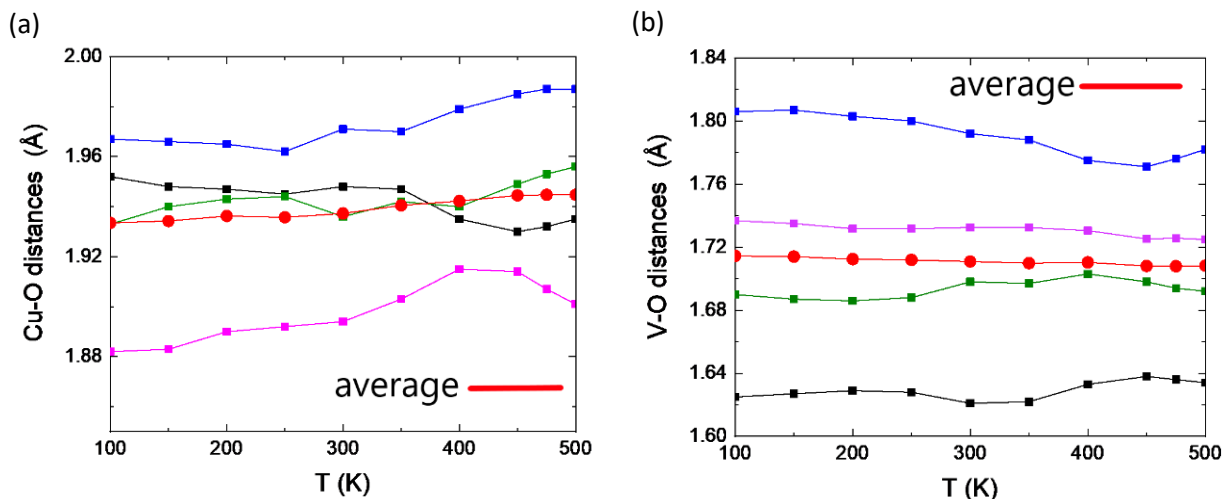


Figure 5.6: Thermal expansion of the (a) Cu-O and (b) V-O bond lengths in $\text{Cu}_2\text{V}_2\text{O}_7$, together with the average employed in the estimation of the MSRD_\perp

The EXAFS fitting model had to consider the complication of the local neighborhood of both Cu and V atoms, consisting of several oxygen atoms at distances that are different, yet not distinguishable in their contribution to the EXAFS signals.

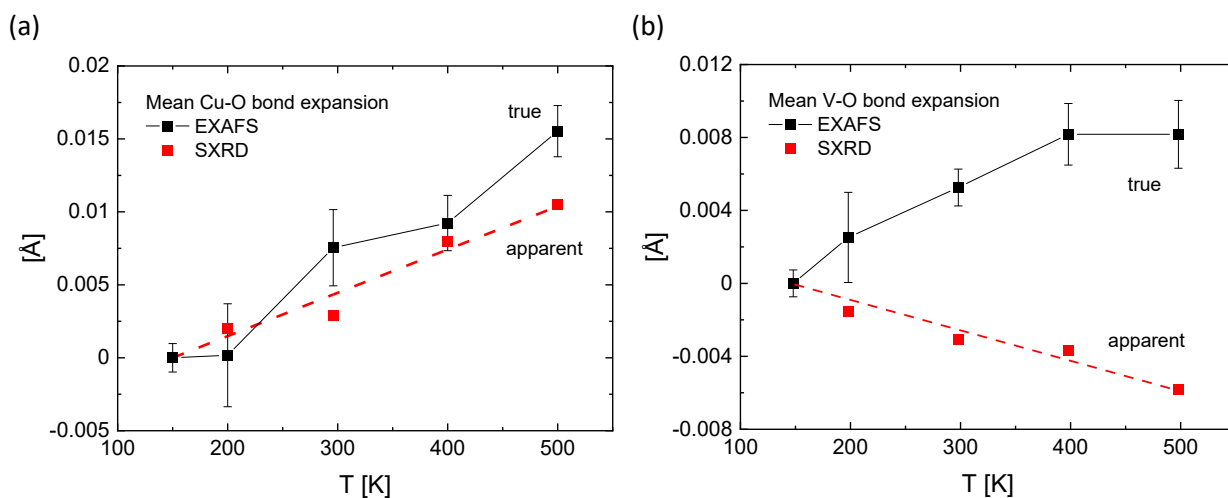


Figure 5.7: Comparison between the variation in temperature of the first cumulant and of the average thermal expansion of the bond lengths of (a) Cu-O and (b) V-O atomic pairs

Thus, the same parameters were assigned to each path, the first cumulant being weighted by the corresponding scattering path length. The first three cumulants have been employed in both cases.

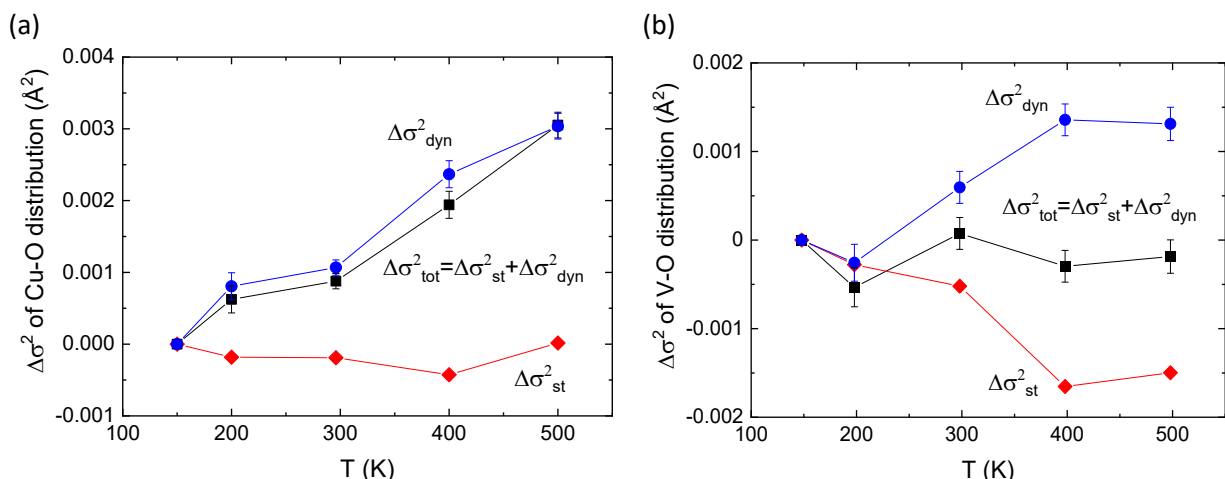


Figure 5.8: Comparison of the total second cumulant variation in temperature and its static and dynamic components of (a) Cu-O and (b) V-O atomic pairs.

A collection of the Fourier transformed signals are reported in Figure 5.4, while examples of fits in Figure 5.5: scattering from the near oxygen atoms give contributions to the first peak, which is considered in this analysis, while the peak structure at higher- R are mainly due to scattering from phosphorus and copper atoms. It can immediately be noted that in the Fourier transforms of the V K-edge EXAFS signals (Figure 5.4) the first peak displays little variation with temperature, contrary to the Cu K-edge case, indicating either very rigid V-O bonds or the presence of a static disorder that is significantly dependent on temperature.

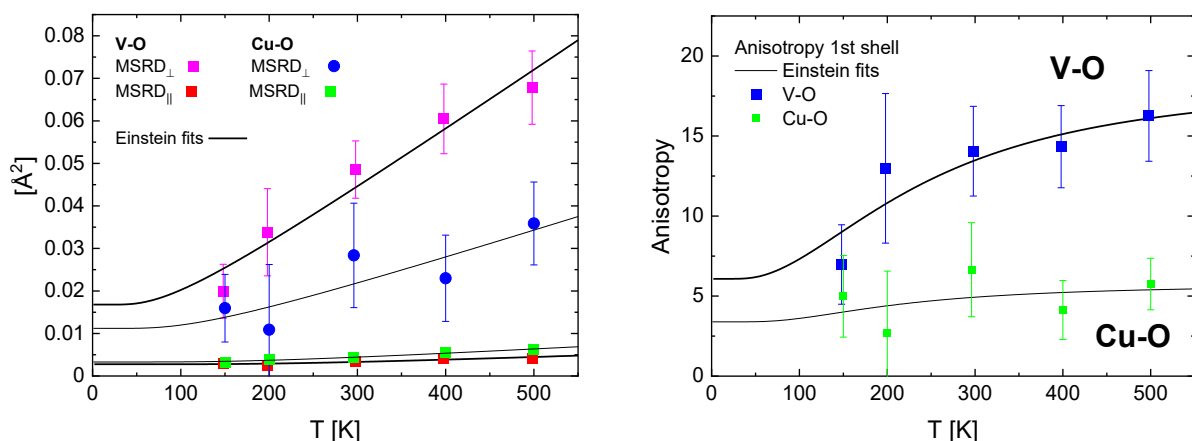


Figure 5.9: (a) Average MSR D transverse and longitudinal for both V-O and Cu-O atomic pairs in $\text{Cu}_2\text{V}_2\text{O}_7$; (b) Vibrational anisotropy ($\text{MSRD}_\perp/\text{MSRD}_\parallel$) for both V-O and Cu-O atomic pairs in $\text{Cu}_2\text{V}_2\text{O}_7$. In both cases the Einstein fits are also reported.

The thermal expansion of Cu-O and V-O bond lengths is shown in Figure 5.6, together with the weighted mean value, which has been employed in the comparison between the true and apparent thermal expansion, shown in Figure 5.7.

While in the case of Cu-O the first cumulant follows the thermal expansion of the bond length, in the case of V-O pairs the first cumulant increases with temperature, while the thermal expansion of the bond decreases, a sign indicating that the transverse vibrations of these pairs are particularly strong. The variation in temperature of the second cumulant, together with its static and dynamic components is reported in Figure 5.8: the static component has been estimated as the standard deviation of the bond lengths.

Cu-O	V-O
Stretching $\nu_{ } = 11.98 \pm 0.55$ THz $k_{ } = 7.50 \pm 0.69$ eV/Å ²	Stretching $\nu_{ } = 15.03 \pm 1.33$ THz $k_{ } = 11.3 \pm 2.0$ eV/Å ²
Bending $\nu_{\perp} = 7.06 \pm 1.13$ THz $k_{\perp} = 2.61 \pm 0.83$ eV/Å ²	Bending $\nu_{\perp} = 4.95 \pm 0.31$ THz $k_{\perp} = 1.22 \pm 0.15$ eV/Å ²
Anisotropy $\gamma \sim 4.9 \pm 2.5$ @300K $2k_{ }/k_{\perp} = 5.8 \pm 1.9$	Anisotropy $\gamma \sim 13.5 \pm 2.8$ @300K $2k_{ }/k_{\perp} = 18.5 \pm 4.0$

Table 5.3: Vibrational anisotropy parameters for Cu₂V₂O₇, comprising transverse and longitudinal Einstein frequencies, the corresponding effective force constants and the vibrational anisotropy

The V-O atomic pairs display a considerable variation in temperature of the static component of the second cumulant, compensating the variation in temperature of the dynamic second cumulant. We have emphasized in Chapter 2 § 2.6 (Results elaboration) that this is an estimation of the static component of the second cumulant and should be considered accordingly as an approximation necessary to tame the crystallographic complication of these compounds from the point of view of EXAFS analysis.

On the contrary, the variation in temperature of the static second cumulant is negligible for Cu-O pairs. The MSRDS transverse and longitudinal and their ratio, quantifying the vibrational anisotropy, are in Figure 5.9: V-O transverse vibrations are significantly more intense than those of Cu-O. A summary of the vibrational properties is given in Table 5.3. Information regarding the synthesis process and further data obtained through other characterization techniques can be found in [3].

5.3 $\text{Cu}_{1.25}\text{Zn}_{0.75}\text{P}_2\text{O}_7$

A series of solid mixtures (in some cases solutions) $\text{Cu}_{2-x}\text{Zn}_x\text{P}_2\text{O}_7$ can be produced if zinc partially replaces copper. In the $x=0.75$, the volumetric CTE is negative ($\alpha_v \approx -6.17 \cdot 10^{-6} \text{ K}^{-1}$, 100-225 K) and as in other cases, no crystalline alpha to beta phase transition is observed in the temperature ranges that have been investigated, while the crystal structure has the symmetry of the beta phase of $\text{Cu}_2\text{P}_2\text{O}_7$

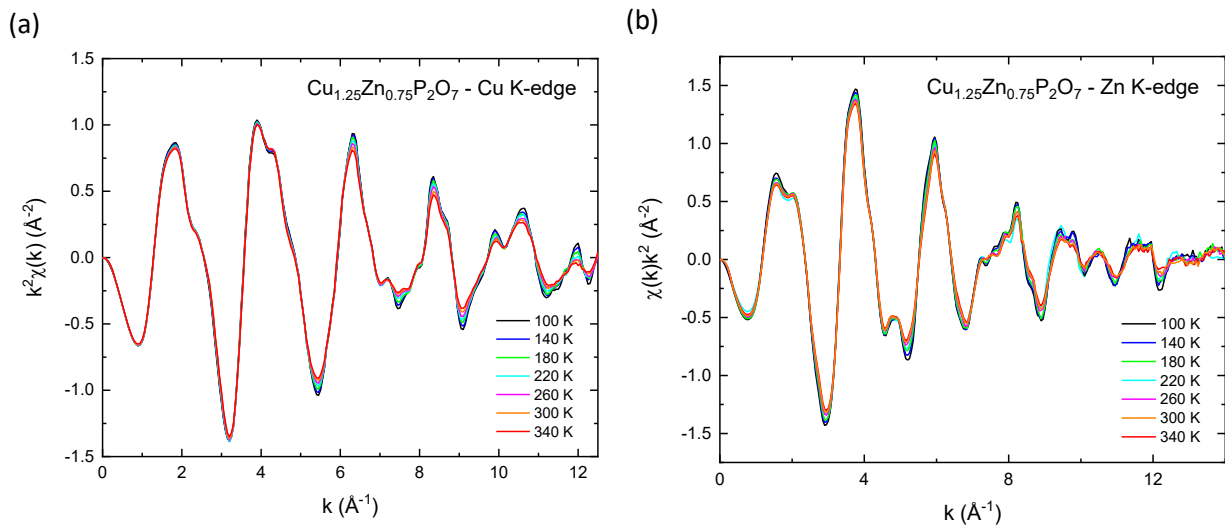


Figure 5.10: Weighted EXAFS signals of $\text{Cu}_{1.25}\text{Zn}_{0.75}\text{P}_2\text{O}_7$ measured at the (a) Cu K-edge and (b) Zn K-edge

(monoclinic with C2/m space group).

XAS data has been acquired at the XAFS beamline of the ELETTRA synchrotron light facility at both Cu and Zn K-edges. Various spectra have been measured in the temperature range 100-340K at regular intervals of 40K. A collection of the resulting k^2 -weighted EXAFS signals can be seen in Figure 5.10.

The crystal structure information obtained by the research group of Prof. Jun Chen using diffraction

Index	Path	Legs	Degeneracy	r_{eff} (Å)	Amplitude	Parameters
1	Cu/Zn-O ₁	2	1	1.9315	100.00	C_1, C_2, C_3, C_4
2	Cu/Zn-O ₂	2	1	1.9851	93.772	
3	Cu/Zn-O ₃	2	1	1.9912	93.099	
4	Cu/Zn-O ₄	2	1	2.0162	90.408	
5	Cu/Zn-O ₅	2	1	2.4948	54.268	Neglected
6	Cu/Zn-O ₆	2	1	2.5664	50.643	Neglected

Table 5.4: Shortest scattering paths and amplitudes for $\text{Cu}_{1.25}\text{Zn}_{0.75}\text{P}_2\text{O}_7$ as calculated using FEFF software and employed to fit the Cu/Zn K-edge EXAFS data

techniques has been employed as input for FEFF calculations of the scattering amplitudes, which are reported in Table 5.4, together with the paths that have been then considered for the EXAFS fitting

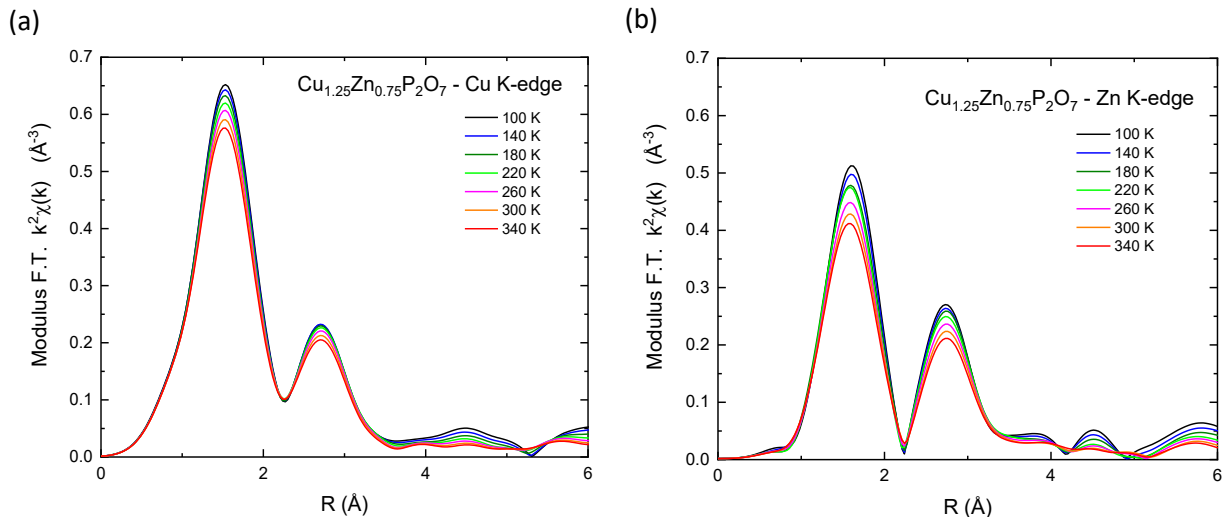


Figure 5.11: Fourier transforms of the weighted EXAFS signals of $\text{Cu}_2\text{V}_2\text{O}_7$ at the (a) Cu K-edge and (b) Zn K-edge

procedure. As in the case of $\text{Cu}_2\text{V}_2\text{O}_7$, the local neighborhoods of Cu and Zn atoms display several oxygen atoms at slightly different distances, whose scattering paths have been assigned the same parameters, the first cumulant being weighted by the scattering path lengths. In this case, though, the addition of the fourth cumulant proved necessary to obtain fits of quality.

A collection of the Fourier transforms is reported in Figure 5.11: the first peak structure has been considered for the fitting procedure and is due to scattering from the near oxygen atoms; the second peak, between 2 and 3 Å^{-1} is mainly due to scattering from copper, zinc and phosphor atoms.

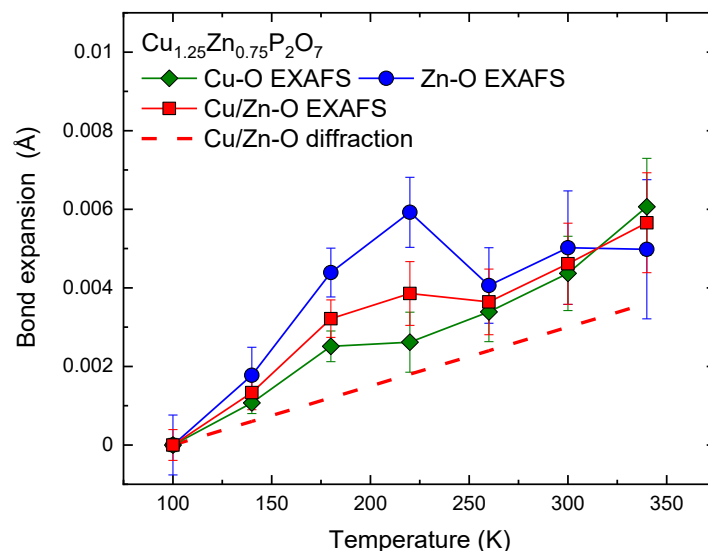


Figure 5.12: Comparison between the variation in temperature of the first cumulant and of the average thermal expansion of the bond lengths of (a) Cu-O and (b) Zn-O atomic pairs, together with their average

Comparison between real and apparent thermal expansion is in Figure 5.12: diffraction techniques are unable to distinguish between Cu-O and Zn-O atomic pairs in $\text{Cu}_{2-x}\text{Zn}_x\text{P}_2\text{O}_7$, but only allow to

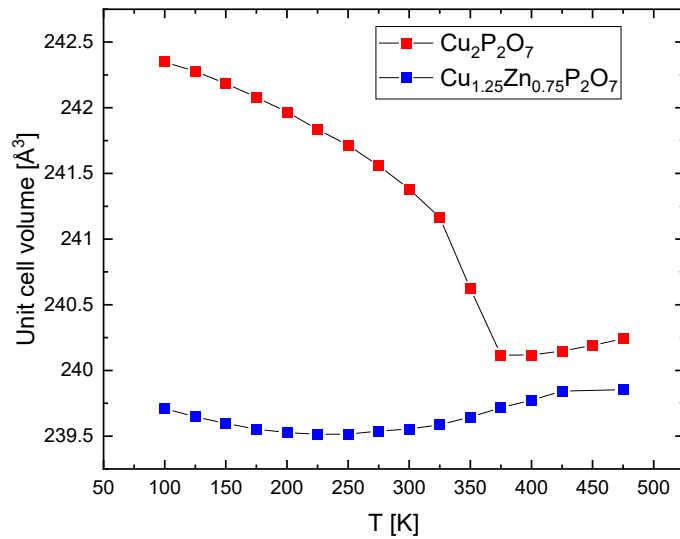


Figure 5.13: Unit cell volume of $\text{Cu}_2\text{P}_2\text{O}_7$ and $\text{Cu}_{1.25}\text{Zn}_{0.75}\text{P}_2\text{O}_7$ versus temperature. While the $\alpha \rightarrow \beta$ transition of $\text{Cu}_2\text{P}_2\text{O}_7$ is visible at around 350 K, no such change is evident for the other curve.

obtain a weighted average of their bond length. Thus, to obtain the MSRD_\perp by the method described in Chapter 2, the mean of the variations of the first cumulants obtained from the two K-edges weighted with the corresponding stoichiometric coefficients was employed using Eq. 2.12.

As in the case of Cu-O atomic pairs in $\text{Cu}_2\text{V}_2\text{O}_7$, the variation in temperature of the static second cumulant was negligible. The average Cu/Zn-O MSRDS transverse and longitudinal and anisotropy are in Figure 5.14. In both transverse MSRDS and anisotropy, a sudden decrease is observed at around 225K, in correspondence to the change of the sign of the volumetric thermal expansion coefficient: it is difficult to interpret this fact given the fact that no crystal phase transition is observed by SXR D (Synchrotron X-Ray Diffraction).

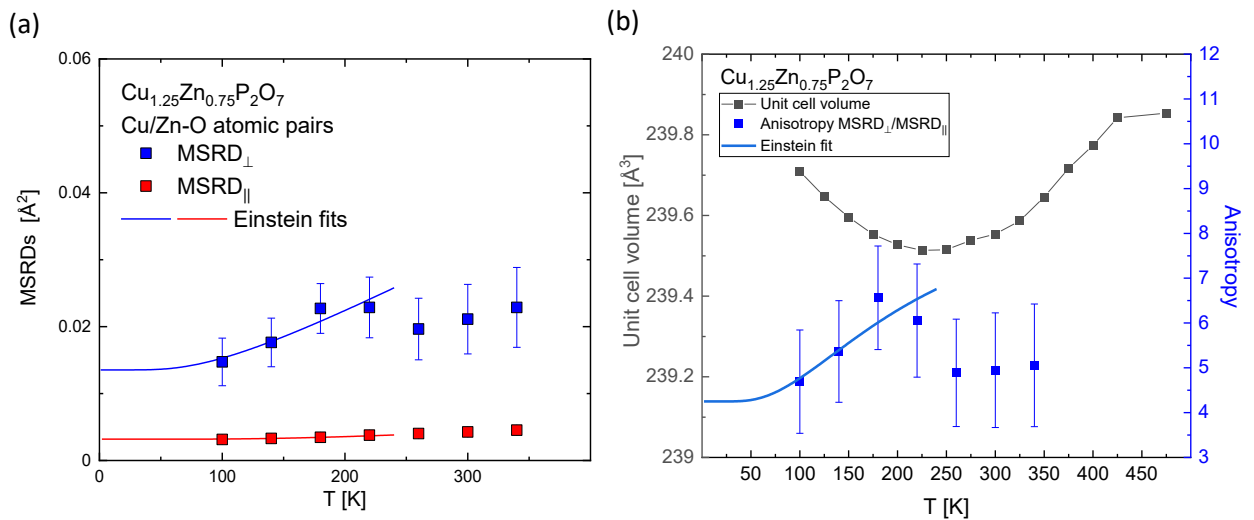


Figure 5.14: (a) Average transverse and longitudinal MSRDS and (b) average vibrational anisotropy of Cu/Zn-O atomic pairs in $\text{Cu}_{1.25}\text{Zn}_{0.75}\text{P}_2\text{O}_7$

This can be seen in Figure 5.13, where the unit cell volume trend with temperature is reported and compared to that of $\text{Cu}_2\text{P}_2\text{O}_7$: the comparison highlights the difference in both the value of the CTE and the value of the unit cell volume. However, it is still worth noting that such a discontinuous behavior doesn't occur for the longitudinal MSR, indicating that transverse vibrations are suppressed in correspondence with the CTE becoming positive, in accordance with observations made in the other chapters of this work.

To fit the average MSR obtained as described above with an Einstein function a weighted reduced mass has been employed: $\mu_{\text{Cu/Zn}} = (1.25 \cdot \mu_{\text{Cu}} + 0.75 \cdot \mu_{\text{Zn}}) / 2$. A summary of the obtained vibrational properties, to be intended as averages for the Cu/Zn-O atomic pairs, can be found in Table 5.5.

Further details regarding the structural characterization and synthesis of the $\text{Cu}_{2-x}\text{Zn}_x\text{P}_2\text{O}_7$ compounds are available in [5].

Cu/Zn-O
Stretching $\nu_{\parallel} = 12.20 \pm 0.23 \text{ THz}$ $k_{\parallel} = 7.80 \pm 0.29 \text{ eV/\AA}^2$
Bending $\nu_{\perp} = 5.83 \pm 0.59 \text{ THz}$ $k_{\perp} = 1.78 \pm 0.36 \text{ eV/\AA}^2$
Anisotropy $\gamma \sim 6.2 \pm 1.2 @300\text{K}$ $2k_{\parallel}/k_{\perp} = 8.8 \pm 1.8$

Table 5.5: Vibrational anisotropy parameters for $\text{Cu}_{1.25}\text{Zn}_{0.75}\text{P}_2\text{O}_7$, comprising transverse and longitudinal Einstein frequencies, the corresponding effective force constants and the vibrational anisotropy

5.4 Discussion and conclusions

The broad context of the copper pyrophosphates analogues gives the opportunity to observe a wide set of interesting thermal expansion properties: apart from strongly changing the CTE, the chemical substitution has an important effect on the polymorphic properties and it surely has on the polymorphic transition temperature, even suppressing the transition. Generically, the effect of P substitution with V is that of widening the temperature range of NTE, while maintaining it to a considerable amount. Cu substitution increases the volumetric CTE from negative to positive in correspondence with a reduction of the AAV; it also strongly changes the polymorphic transition, up to the point of suppressing it completely.

Much can be learnt by investigating of some relevant members of this class of materials, since they display complicating factors that all together take EXAFS spectroscopy to its extreme capabilities: various crystallographically inequivalent atoms with similar distances from the absorber atom, significant static disorder variation with temperature, a crystal phase transition and short bond lengths requiring careful background removal.

But they also present aspects that are difficult to model theoretically: the polyhedral units VO_4 and CuO_5 that perform rocking motions in $\text{Cu}_2\text{V}_2\text{O}_7$ are not rigid, a fact that challenges the theories that require or strongly depends on rigid units; a phase transition and soft phonon modes are both present and can be expected to give crucial contributions to thermal expansion, as pointed out in Chapter 1. Therefore, these materials seem the perfect place to apply EXAFS spectroscopy to extract novel information on the issue; also, the possibility of a common mechanism for NTE in materials with quite different crystal structures is indeed an interesting one.

In this chapter, the EXAFS analysis of two compounds of this family has been presented. From the results regarding $\text{Cu}_2\text{V}_2\text{O}_7$, we can expect that Cu-O and V-O atomic pairs play different roles in determining the thermal expansion properties, given the significant difference between the anisotropy of their thermal vibrations. In particular, V-O atomic pairs, having stronger transverse vibrations, are expected to play a major role in the NTE mechanism.

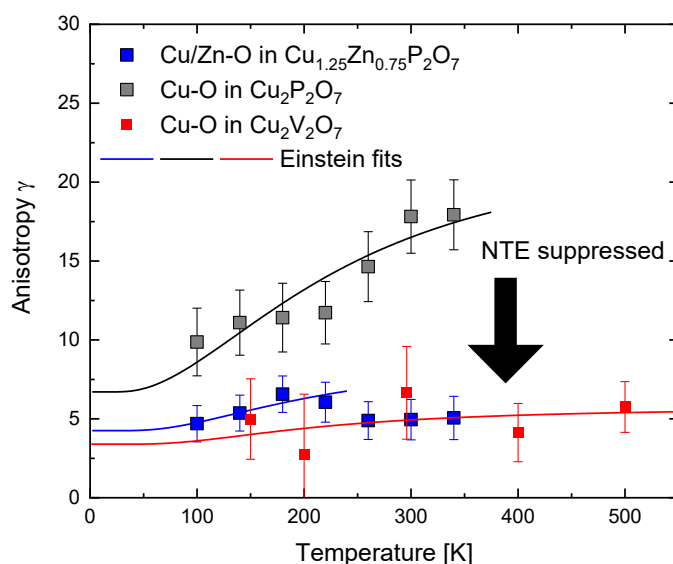


Figure 5.15: Thermal vibrations anisotropy of Cu-O or Cu/Zn-O atomic pairs in $\text{Cu}_2\text{P}_2\text{O}_7$ and its analogues that have been presented in this chapter

Here few words must be spent on the estimation of the static component of the second cumulant: since the total second cumulant shows little variation with temperature and the static second cumulant can be expected to be great, it is difficult to clearly establish the quantitative validity of the

results regarding the V-O atomic pairs. However, the comparison between the anisotropy of thermal vibration of the V-O and Cu-O atomic pairs, together with the fact that the same estimation procedure has been employed for the static second cumulant, allows to be confident in the semiquantitative conclusion that V-O atomic pairs are indeed stiffer to bending than Cu-O. In this complicated picture EXAFS spectroscopy gives simple yet crucial information that sheds light on the microscopic mechanism of NTE: an example can be seen in Figure 5.15, where the anisotropy of Cu/Zn-O or Cu-O atomic pairs is reported to highlight that, once again, the anisotropy of thermal vibrations of linking atoms is suppressed as NTE is diminished. This information, combined with SXRD and total scattering measurements, reported in [5], [1], [3] and [4], allowed to conclude that the NTE is mainly determined by transverse vibrations of linking oxygen atoms.

Bibliography

- [1] N. Shi et al., "Strong Negative Thermal Expansion in a Low-Cost and Facile Oxide of $\text{Cu}_2\text{P}_2\text{O}_7$," *J. Am. Chem. Soc.*, vol. 142, no. 6, pp. 3088-3093, 2020.
- [2] N. Zhang et al., "Negative thermal expansion and electrical properties of $\alpha\text{-Cu}_2\text{V}_2\text{O}_7$," *J. Eur. Cer. Soc.*, vol. 36, no. 11, pp. 2761-2766, 2016.
- [3] N. Shi et al., "Negative and zero thermal expansion in $\alpha\text{-(Cu}_{2-x}\text{Zn}_x\text{)V}_2\text{O}_7$ solid solutions," *Chem. Comm.*, no. 73, pp. 10666-10669, 2020.
- [4] N. Shi et al., "Strong Negative Thermal Expansion of Cu_2PVO_7 in a Wide Temperature Range," *Chem. Mater.*, vol. 33, no. 4, pp. 1321-1329, 2021.
- [5] N. Shi et al., "Tuning thermal expansion from strong negative to zero to positive in $\text{Cu}_2\text{-xZn}_x\text{P}_2\text{O}_7$ solid solutions," *Scripta Materialia*, p. 114289, 2022.
- [6] V. Korthuis et al., "Negative thermal expansion and phase transitions in the $\text{ZrV}_2\text{-xPxO}_7$ series," *Chem. Mater.*, vol. 7, pp. 412-417, 1995.
- [7] H. Wang et al., "Negative thermal expansion properties of $\text{Cu}_{1.5}\text{Mg}_{0.5}\text{V}_2\text{O}_7$," *Ceram. Inter.*, vol. 45, no. 8, pp. 9814-9819, 2019.
- [8] N. Katayama et al., "Microstructural effects on negative thermal expansion extending over a wide temperature range in $\beta\text{-Cu}_{1.8}\text{Zn}_{0.2}\text{V}_2\text{O}_7$," *Appl. Phys. Lett.*, vol. 113, p. 181902, (2018).
- [9] T. I. Krasnenko et al., "Thermal strain in zinc pyrovanadate," *Inorganic Materials*, vol. 36, p. 1032–1035, 2000.
- [10] N. Zhang et al., "Negative thermal expansion and electrical properties of $\alpha\text{-Cu}_2\text{V}_2\text{O}_7$," *Journal of the European Ceramic Society*, vol. 36, no. 11, pp. 2761-2766, 2016.
- [11] L. Chen et al., "Negative thermal expansion properties of $\text{Cu}_{1.8}\text{Co}_{0.2}\text{V}_2\text{O}_7$," *Solid State Communications*, vol. 352, p. 114810, 2022.
- [12] R. Chen et al., "Continuous tailoring thermal expansion from giant negative to positive in $\text{Ni}_2\text{P}_2\text{O}_7$ -based materials," *Scripta Materialia*, vol. 214, p. 114653, 2022.
- [13] M. V. Rotermel and T. Krasnenko, "Mechanism of Thermal Expansion of Structural Modifications of Zinc Pyrovanadate," *Crystallography Reports*, vol. 62, p. 703–709, 2017.
- [14] C. Lind, "Two Decades of Negative Thermal Expansion Research: Where Do We Stand?," *Materials*, vol. 5, pp. 1125-1154, 2012.

Chapter 6

Nanosize effects on thermal expansion: a molecular dynamics study

Nanostructuring has an important effect on thermal expansion coefficient, which can even change sign with respect to the bulk value. It has been proposed that in the case of metallic nanoparticles the electronic excitations play a crucial role, remarkably complicating the description of the phenomenon: to simplify the matter it is interesting to simulate the behavior of vibrations in model nanosystems, spherical gold nanoparticles, neglecting the electronic degrees of freedom. In this chapter molecular dynamics simulations regarding this matter are presented.

6.1 EXAFS spectroscopy and molecular dynamics

After having reported on the experimental investigations regarding NTE materials, theoretical work on systems of interest to the study of NTE is described. In particular, Molecular Dynamics (MD) simulations have been performed to clarify the role of thermal vibrations in gold nanoparticles of various diameters, given their importance as a model system, and the effect of nanostructuring on thermal expansion phononic contributions.

An interesting characteristic of EXAFS spectroscopy is its strong dependence on crystal structure and lattice dynamics rather than electronic structure. This allows to formulate the EXAFS equation in terms of cumulants of the atomic pair distribution function. So, if the cumulants are calculated, it is possible to compare them to EXAFS fits results of the system under scrutiny. This approach can complement the EXAFS analysis by allowing the investigation of quantities that are difficult to directly access by experiment: for example, distances which are not directly accessible due to atoms having too little atomic number or atoms having too similar atomic number to be resolvable in the EXAFS signals. The dependence on temperature of the cumulants of the real distribution can also be calculated if the lattice dynamics is known. In this regard, molecular dynamics is a very useful

computational technique: the fundamental idea behind it is to sample the statistical ensemble describing a system of bodies (atoms or molecules) by solving the equations of motions and saving the resulting coordinates (and velocities). If this process is given enough time, ensemble averages can be appropriately substituted by time averages and the related uncertainties can be estimated. The software GULP [1], [2] has been employed to perform classical molecular dynamics calculations. The Leapfrog-Verlet solution scheme for the equations of motion has been employed: this ensures energy conservation within levels acceptable for this type of calculations.

In this chapter all the cumulants are intended as relative to the real distribution since the molecular dynamics algorithm effectively samples the real distribution of atomic pair distances. Only cumulants up to the fourth are usually employed in EXAFS fitting procedures; their expressions are

$$C_1 = \langle r \rangle, \quad (6.1)$$

$$C_2 = \langle (r - \langle r \rangle)^2 \rangle, \quad (6.2)$$

$$C_3 = \langle (r - \langle r \rangle)^3 \rangle, \quad (6.3)$$

$$C_4 = \langle (r - \langle r \rangle)^4 \rangle - 3C_2^2, \quad (6.4)$$

where r is the atomic pair distance and the angular brackets indicate the ensemble average.

Calculation of other quantities is available with the molecular dynamics results, e.g. the difference between the average real interatomic distance, the first cumulant ($\langle |\vec{r}_1 - \vec{r}_2| \rangle$), where \vec{r}_1 and \vec{r}_2 are the positions of the atoms in the considered pair), and the apparent one ($|\langle \vec{r}_1 \rangle| - |\langle \vec{r}_2 \rangle|$), the modulus of the average difference of positions of two atoms.

To build a theoretical framework in which to interpret the results, it is possible to consider a (rather simplified) potential energy of atomic pair deformation

$$V(r) = V(r_0) + \frac{k}{2}(r - r_0)^2 + k_3(r - r_0)^3 + k_4(r - r_0)^4, \quad (6.5)$$

where r is the distance between the two atoms; the classical expressions for the cumulants of a system with this interatomic potential energy are then obtained as integral averages. So, for example, the cumulants for a system whose dynamics is described by the (classical) potential in Eq.(6.5) at leading order in temperature T :

$$C_1 \approx r_0 - 3k_3k_B T/k^2, \quad (6.6)$$

$$C_2 \approx k_B T/k, \quad (6.7)$$

$$C_3 \approx -6k_B^2 T^2 k_3/k^3. \quad (6.8)$$

These results are obtained in the Quasi-Harmonic Approximation (QHA) and may be compared with the results obtained using the molecular dynamics. While the classical trend in temperature is linear for the second cumulant and quadratic for the third cumulant, quantum expressions for the cumulants are more expressed as more complicated functional forms, which are also available and reduce to the expressions above in the high temperature limit. Quantum effects on EXAFS cumulants are evident at very low temperatures, but the classical results obtained through these numerical simulations may be extrapolated to very low temperatures using simple models, as usually in the EXAFS data analysis the dynamical second cumulant k_2 and the extracted MSRD_\perp are interpolated with an Einstein (like in this work) or Debye model [3], [4], [5], [6].

We will now detail the steps for a complete molecular dynamics simulation. First, the system under investigation must be defined: the atoms or molecules composing it must be specified and assigned initial positions inside a simulation volume with boundary conditions.

After this the equations of atomic/molecular motions must be specified: for this it is usually sufficient to define the interaction potential energy. In this work the Sutton-Chen potential for gold has been employed: it is a particular case of Finnis-Sinclair potentials described by the following formula

$$E_{pot,SC} = \varepsilon \sum_i \left[\sum_{j \neq i} V_{ij} / 2 - c \sqrt{\rho_i} \right], \quad (6.9)$$

where $V_{ij}(r) = \left(\frac{a}{r_{ij}}\right)^n$ and $\rho_i = \sum_{j \neq i} \left(\frac{a}{r_{ij}}\right)^m$, with r_{ij} the distance between the atoms i and j . Thermal properties of noble metals are well described employing these simple potentials, requiring a total of 4 independent parameters. Additionally, a cutoff distance for the repulsive power law interactions (V_{ij}) is set to quicken and simplify calculations (12 Å for all nanoparticles in this work).

ε [eV]	a [Å]	c	m	n
1.2793E-2	4.08	34.408	8	10

Table 6: Parameters for the Sutton-Chen potential employed in the present work, as presented in [7]

The parameters defining the potential are presented in Table 6. This potential correctly predicts an fcc ground state structure for bulk gold. To define the statistical ensemble to sample it is necessary to simulate the effect on the system of a thermostat and/or barostat: their parameters regulate how the dynamics must be changed and ultimately determine the equilibration process (in this case in the Nosé-Hoover scheme). It is also necessary to determine how often the thermostat/barostat intervenes, through the scaling timestep. The timesteps for other important processes must then be decided: the evolution timestep and the sampling timestep. The evolution timestep, which is the timestep by which the time coordinates are discretized, should be significantly smaller than the period of fastest oscillation: usually for atomic systems it is sufficient to set the timestep slightly smaller than 1 fs , considering the typical vibrational frequencies of such systems. The equilibration and simulation time must also be defined: the equilibration time should be set to allow the sampling distribution to converge to the desired one; the simulation time should at least be longer than the period of the slowest oscillations and as long as possible to let the system visit the allowed phase space the most possible. The period of the slowest motions is dictated by the boundary conditions: as the size of the simulation volume increases the minimum simulation time to obtain acceptable results also increases.

6.2 Physical quantities

At last, the physical quantities of interest can be extracted; to do so a subset of atomic pairs is selected: in this work this is obtained by specifying a range of instantaneous distances and eventually also conditions on their distance from the center of the nanoparticles. The main physical quantities of concern here are: the cumulants (both static and dynamic) of the real distribution of atomic pair distances, the average (crystallographic) relative position of the atomic pairs, the longitudinal and transverse MSRD and the anisotropy of the thermal vibrations.

As has been pointed out in the EXAFS spectroscopy analysis section, a physically relevant distinction can be operated between total, dynamic and static cumulant: in the context of molecular dynamics, the first is the average of the individual pair contributions to the cumulant at all times and over all the atomic pairs, while the second is defined as the average over pairs of the time averages of the individual pair contributions to the cumulant. The static cumulant is defined as the difference between total and dynamic cumulant. As a relevant illustrative example:

$$C_{1,tot} = \frac{\sum_i^{N_{pairs}} \sum_j^{N_{times}} r_i(t_j)}{N_{pairs} \cdot N_{times}} \quad (6.10)$$

$$C_{2,tot} := \frac{\sum_i^{N_{pairs}} \sum_j^{N_{times}} (r_i(t_j) - C_{1,tot})^2}{(N_{pairs} \cdot N_{times} - 1)} \quad (6.11)$$

$$C_{2,dyn} := \frac{\sum_i^{N_{pairs}} \sum_j^{N_{times}} (r_i(t_j) - \langle r_i \rangle_{time})^2}{(N_{pairs} - 1) \cdot (N_{times} - 1)} \quad (6.12)$$

$$C_{2,stat} := C_{2,tot} - C_{2,dyn} \quad (6.13)$$

where $\langle r_i \rangle_{time}$ represents the time average of the i -th considered atomic pair. Similar relationships hold for third and fourth cumulants. These results may then be compared with those extracted from EXAFS spectroscopy analysis.

6.3 Test in gold bulk

To give a reference system for the performance of the chosen potential, gold bulk has been investigated. It will also prove useful in illustrating the procedure and the results in a concrete way. Constant volume canonical ensemble calculations have been performed and will be presented. The volume has been fixed using experimental data [8].

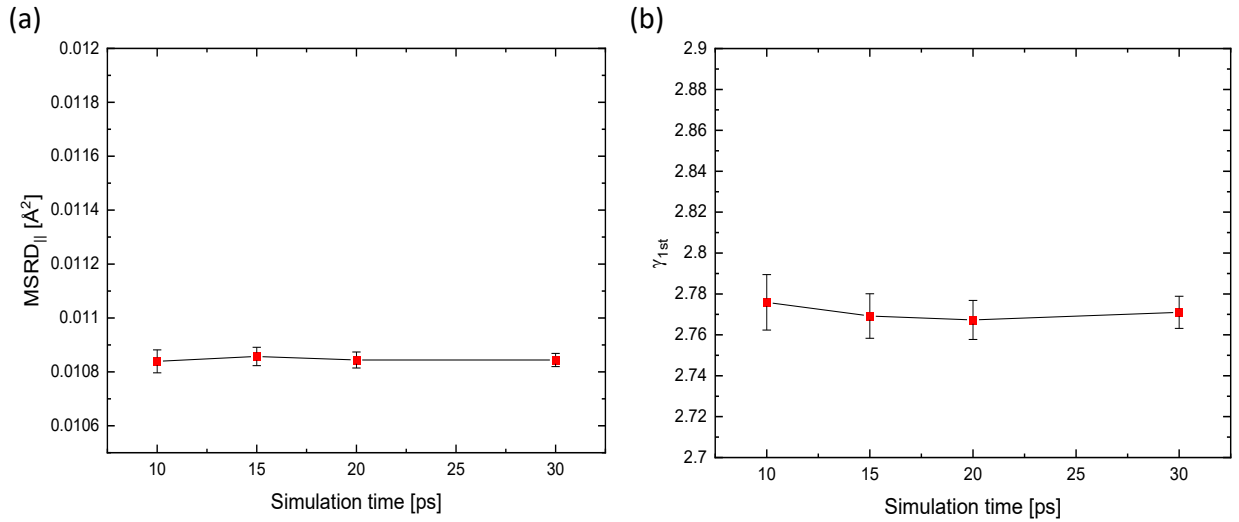


Figure 6.1: Dependence on simulation time of (a) $MSRD_{||}$ and (b) anisotropy ratio γ @ 300K

T [K]	Supercell	Sampling/simulation timestep	NN distances sampling range
100,200,300,413,513	8x8x8 (512 atoms)	0.01/0.0005 ps	[1.5,3.7] Å

Table 7: Simulations parameters for gold bulk

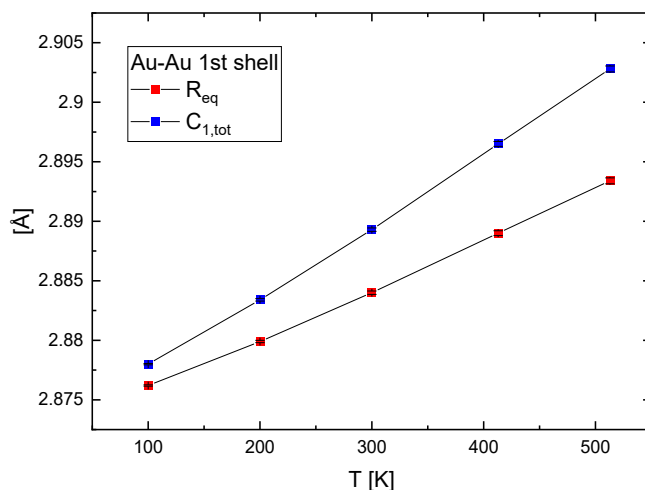


Figure 6.2: Comparison of first shell interatomic “real” and “apparent” distances

The constant volume ensemble has been preferred over the constant pressure one, because the number of atoms introduced in the periodic cell is too small to render those simulations stable. The simulation settings for these simulations are reported in (scaling timestep is the same as simulation timestep). Several quantities of interest to EXAFS spectroscopy are then presented: the comparison between the first cumulant and the “apparent” distance at various temperatures is shown in Figure 6.2, which, as expected, are clearly different. The anisotropy ratio γ at different temperatures and the longitudinal and transverse MSRDS are shown in Figure 6.4: the agreement with experimental values (around 2.78) is remarkable and indicates that, as expected in a fcc crystal, the vibrational properties are quasi-isotropic.

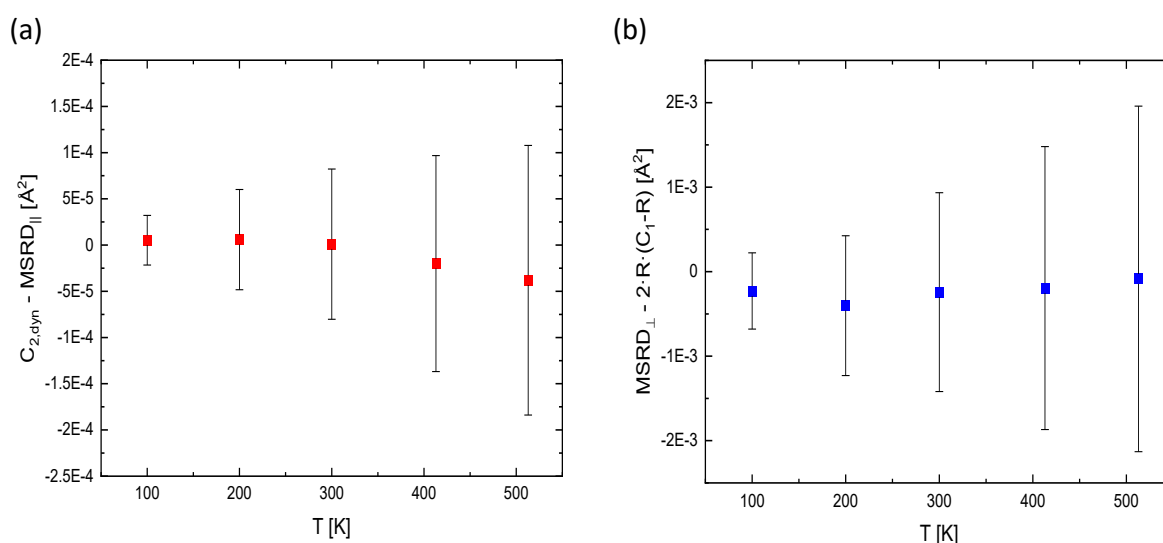


Figure 6.3: (a) Difference between the dynamical second cumulant and its estimated value as the $MSR D_{||}$; (b) difference between the $MSR D_{\perp}$ and its estimated value using the real and apparent distances

A collection of physical quantities is presented in Table 8 and compared to experimental values: in particular the Einstein frequencies longitudinal and transverse is defined respectively as

$$v_{\parallel} = \sqrt{k_{\parallel}/\mu} \quad (6.14)$$

$$v_{\perp} = \sqrt{k_{\perp}/\mu} \quad (6.15)$$

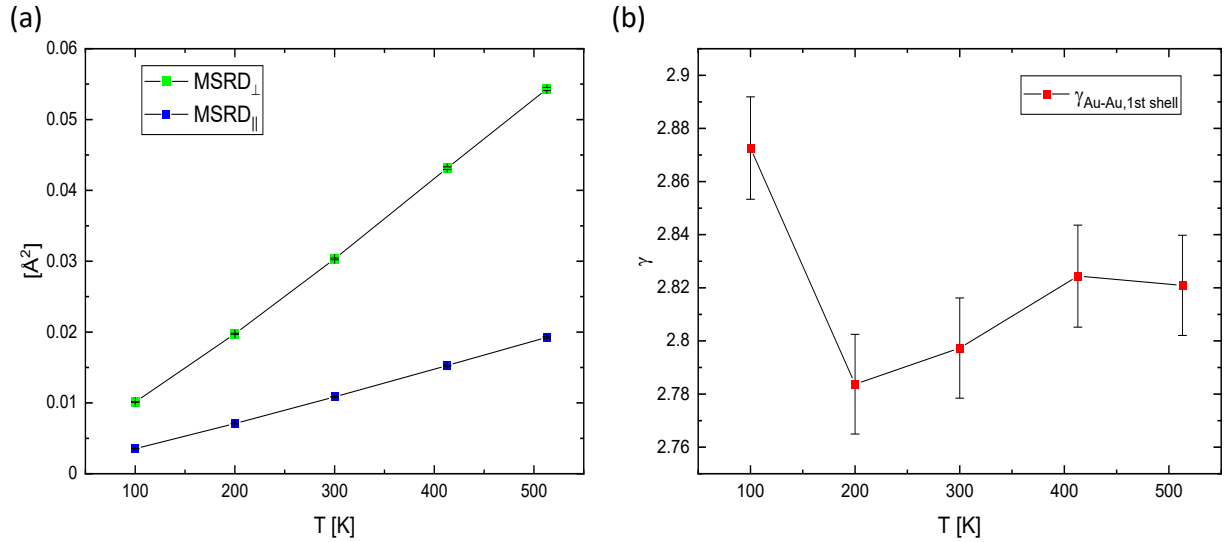


Figure 6.4: (a) Transverse and longitudinal MSRDS; (b) anisotropy ratio γ as a function of temperature

The third order force constant, which is also reported there, is obtained by fitting the dynamical third cumulant using the approximation in Eq. (6.8), that is a quadratic power law in temperature: the discrepancy with the experiment is remarkable, but the strong dependence on the second order force constant in Eq. (6.8) probably plays a role in it.

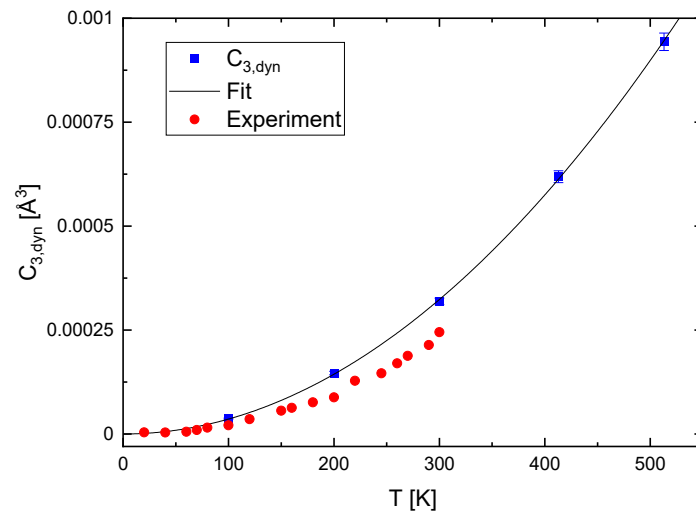


Figure 6.5: Third cumulant dynamic component versus temperature fitted with a quadratic function, compared with the experimental results from [9] (corrected according to the quantum theory)

Quantity	Calculated value	Experimental value
$\nu_{ }$	(2.41±0.01) THz	2.82 THz
ν_{\perp}	(2.03±0.01) THz	2.17 THz
$\nu_{\perp}/\nu_{ }$	(0.842±0.008)	0.77
k_3	(-1.06±0.05) eV Å ⁻³	-1.94 eV Å ⁻³

Table 8: Collection of quantities calculated using molecular dynamics results for gold bulk; experimental values are taken from [9]

The simulated $C_{3,dyn}$ is shown in Figure 6.5 together with the experimental results from [9], increased by a constant so as they tend to the correct value dictated by the quantum theory at 0K, in order to allow comparison with the simulation results: again, although the results of the simulations qualitatively reproduce the experimental ones, a certain degree of discrepancy is evident.

In conclusion, although the employed model is quite simplistic, it can still be expected to be useful in answering questions regarding the effect of nanostructuration on gold, giving semi-quantitative or even quantitative results in accordance with experiment.

6.4 Gold nanoparticles

After having established some simple reference results, we turn to the main subject of this numerical investigation: the effect of nanostructuration on phonons and their contribution to the thermal expansion coefficient. To do so, we explore the vibrational dynamics of model systems, gold nanoparticles of various diameters, ignoring the electronic degrees of freedom. It has been mentioned before that electronic thermal excitations may be relevant to NTE: in the particular case of metallic nanoparticles, following the approach of Kubo [10], electronic excited states with a discrete energy

T [K]	Diameter [nm] (#atoms)	Sampling/Simulation timestep	NN distances sampling range
50,100,200,300	1.3 (80)	0.01 ps/0.0005 ps	[1.5,3.7] Å
	2 (250)		
	3 (888)		
	4 (1986)		
	5 (3926)		
	8 (15947)		

Table 9: Simulation parameters for gold spherical nanoparticles

spectrum with a fixed spacing comparable to the thermal energy at cryogenic temperature appear above the Fermi surface:

$$\Delta E_n \approx \frac{4nE_F}{3N} \quad (6.16)$$

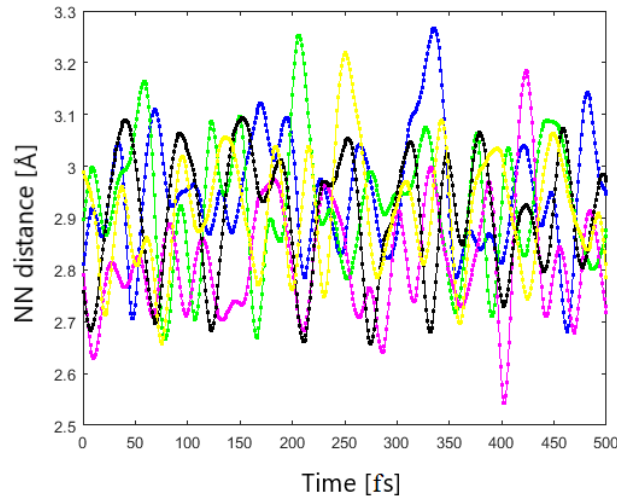


Figure 6.6: Example of sampling processes for a 4 nm diameter gold nanoparticle at 300K: instantaneous nearest neighbors' distance of 5 randomly chosen atomic pairs

where n is the excitation level index, N is the number of atoms in the nanoparticle and E_F is the Fermi energy of the bulk metal [11].

The relative thermal excitation energy of electrons, while negligible for bulk materials, becomes relevant for nanoparticles and can negatively contribute to thermal expansion [121].

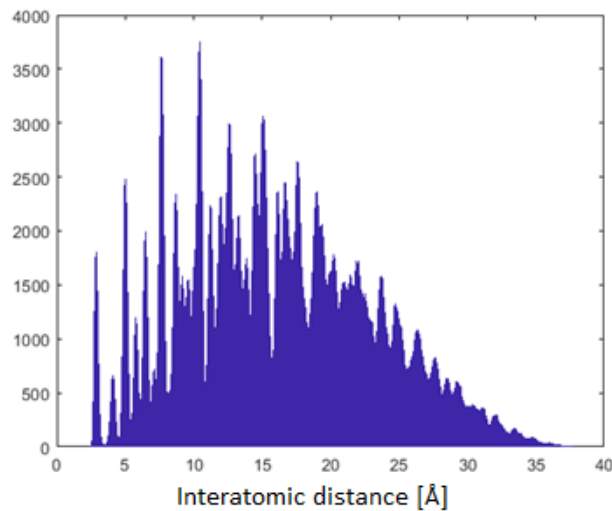


Figure 6.7: Radial distribution function in a 4nm diameter nanoparticle at 300K

The phonon contributions to the thermal expansion though, which are taken in consideration in this chapter, constitute the basis to understand physical anomalies (especially in the thermal expansion) in metallic and non-metallic nanoparticles, also considering that they are also more thoroughly theoretically understood. That is what we will try to accomplish with these simulations.

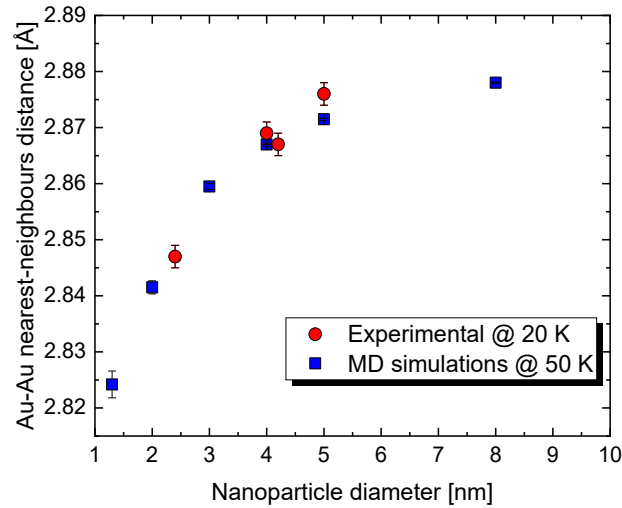


Figure 6.8: Comparison between experimental results of apparent NN distances [13] and the numerical simulations on gold nanoparticles at low temperatures

The setting parameters for these simulations are reported in Table 9 (scaling timestep is the same as simulation timestep). Gold spherical nanoparticles are built starting as a spherical fcc gold cluster; the system then undergoes through a phase of thermal and mechanical equilibration and then the sampling of states is performed [11]. An example of the equilibration and sampling processes for a nanoparticle is given in Figure 6.6, regarding a 4nm diameter at 300K. The resulting distribution of distances is reported in Figure 6.7: as is expected, and in accordance with experimental results [121] which report a fcc structure in gold nanoparticles, peaks related to a “crystalline” fcc structure are visible, even if they are significantly smeared. Using the sampled positions of the atoms constituting the nanoparticles, physical quantities may be extracted to check the quality of the performed calculations. For example, the first neighbors’ distance in nanoparticles can be successfully compared to experiment (see Figure 6.8).

The NN distance in nanoparticles is shorter than in the bulk, in particular

$$\Delta R_{eq} = -\frac{4f \cdot K_{bulk} \cdot R_{bulk}}{3D} \quad (6.17)$$

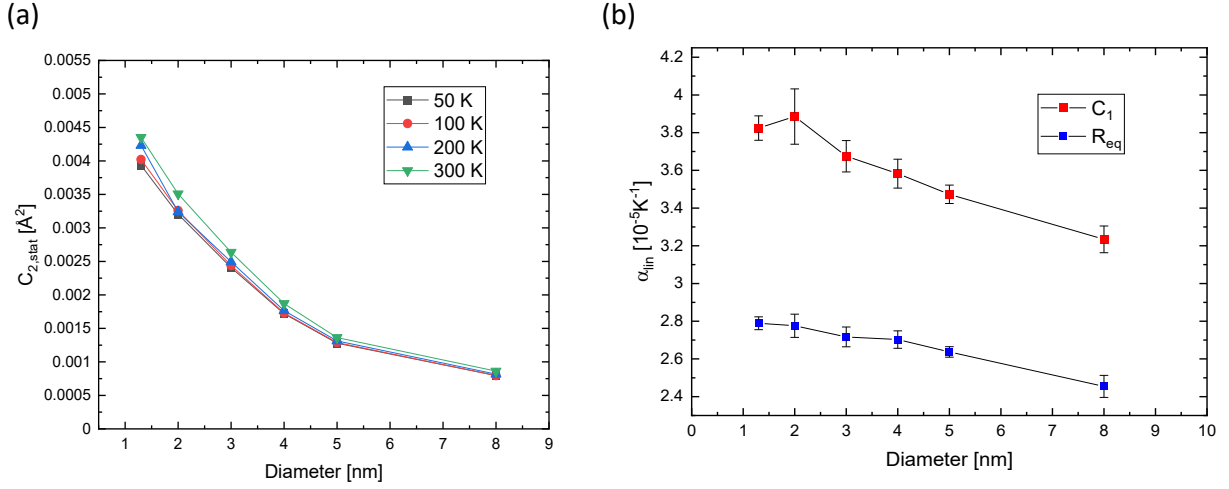


Figure 6.9: (a) Static second cumulant for gold nanoparticles at various temperatures and (b) thermal expansion versus diameter

where ΔR_{Eq} is the contraction of the nearest neighbors' distance, K_{bulk} is the bulk compressibility (taken as 180 GPa^{-1}), R_{bulk} is the nearest neighbors' distance in the bulk (taken as 2.87792 \AA), D is the diameter of the nanoparticle.

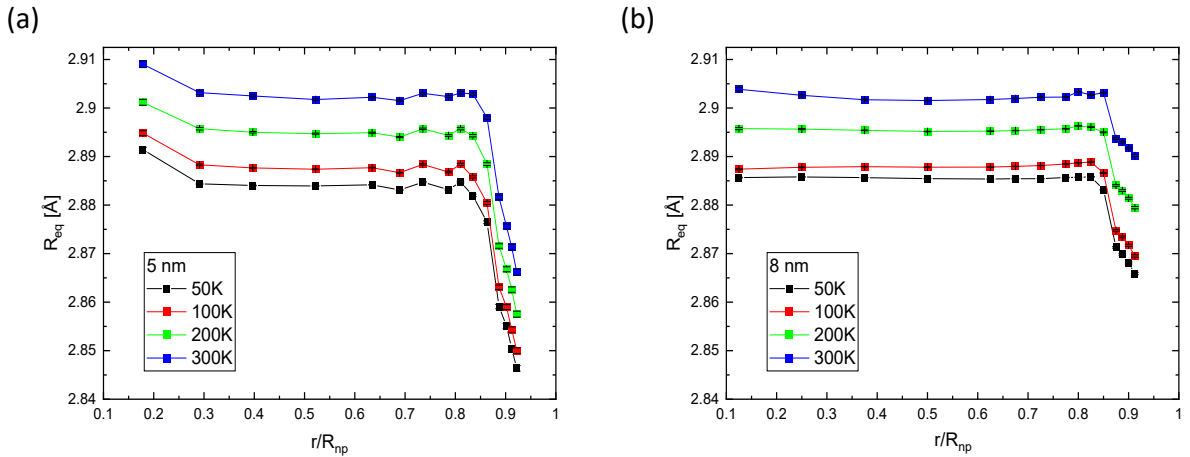


Figure 6.10: Nearest neighbors' "apparent" distance at different distances from the center (normalized by the nanoparticle radius R_{np}) in nanoparticles of diameter (a) 5 nm and (b) 8 nm

Thus, the surface tension can be extracted, giving $f = (3.9 \pm 0.2) \text{ Jm}^{-2}$, to be compared to the experimental value $(3.8 \pm 0.3) \text{ Jm}^{-2}$ [13], while the bulk value is 2.7 Jm^{-2} [14]. In Figure 6.9 the static second cumulant and the thermal expansion coefficients (calculated using both the "apparent" and "real" NN distances) are reported: the thermal expansion coefficient (only due to phonons) is significantly higher than the corresponding experimental bulk value ($\alpha_{lin} \approx 1.4 \times 10^{-5} \text{ K}^{-1}$) and is

dependent on the nanoparticle diameter; also, nanoparticles with greater diameter display less

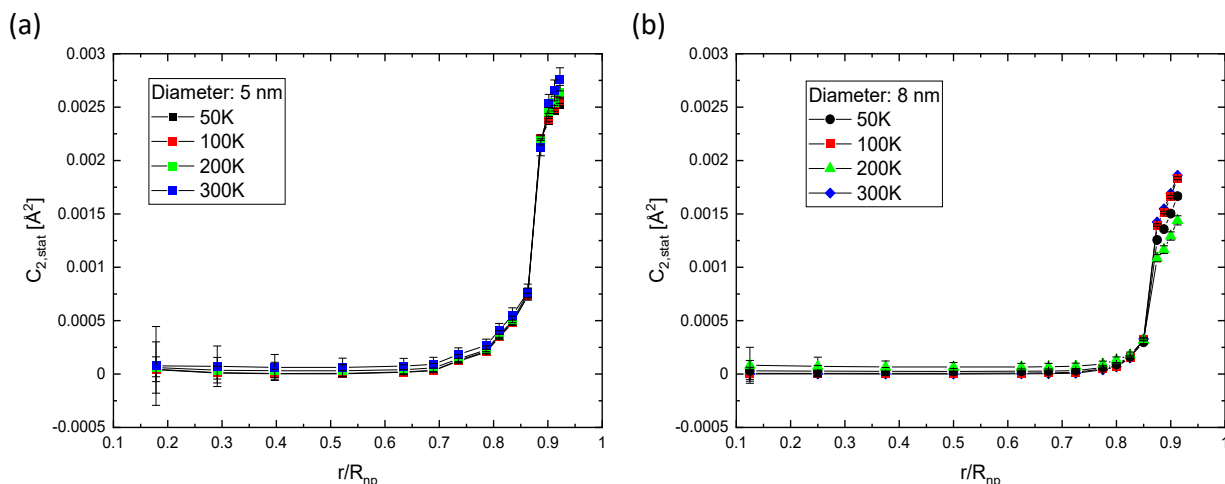


Figure 6.11: Static second cumulant at different distances from the center (normalized by the nanoparticle radius R_{np}) in nanoparticles of diameter (a) 5nm and (b) 8nm

static disorder, which is expected as the surface area over bulk volume is lower. To see if this is indeed the case and as an interesting example of calculation of quantities that are usually inaccessible to direct analysis, we present here the quantities at different radial distances from the center for the largest nanoparticles. The quantities are estimated in layers that are 1 nm thick. The nearest

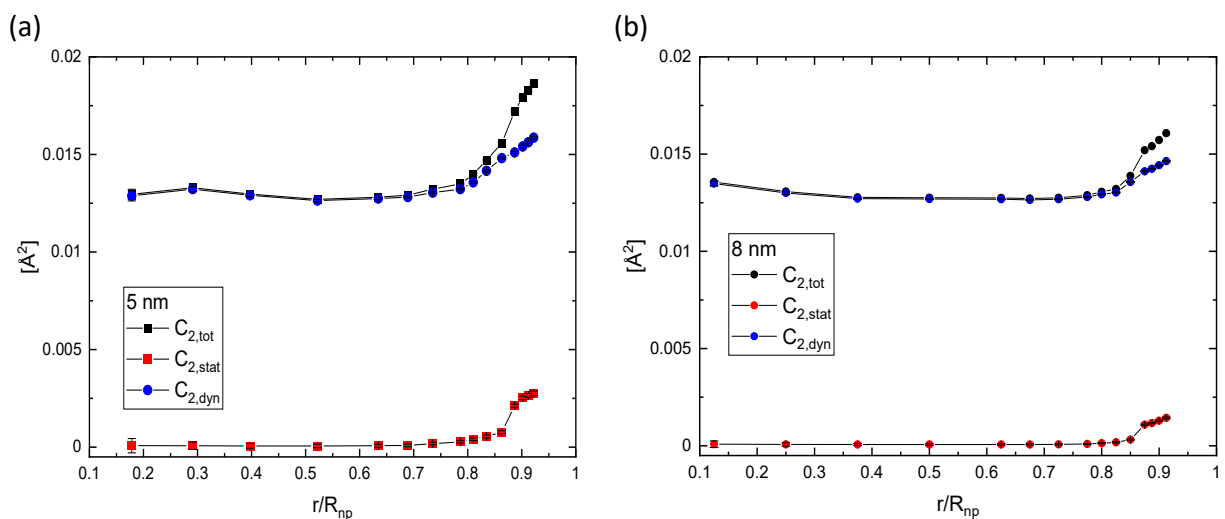


Figure 6.12: Comparison between the static, dynamic and total second cumulants at different distances from the center (normalized by the nanoparticle radius R_{np}) in nanoparticles of diameter (c) 5nm and (d) 8nm

neighbors' "apparent" distances in these layers at different distances from the center are reported in Figure 6.10 for nanoparticles of diameter 5 and 8 nm. In Figure 6.11 the static second cumulant contributions from the different layers are disaggregated in the nanoparticles of greater size: as

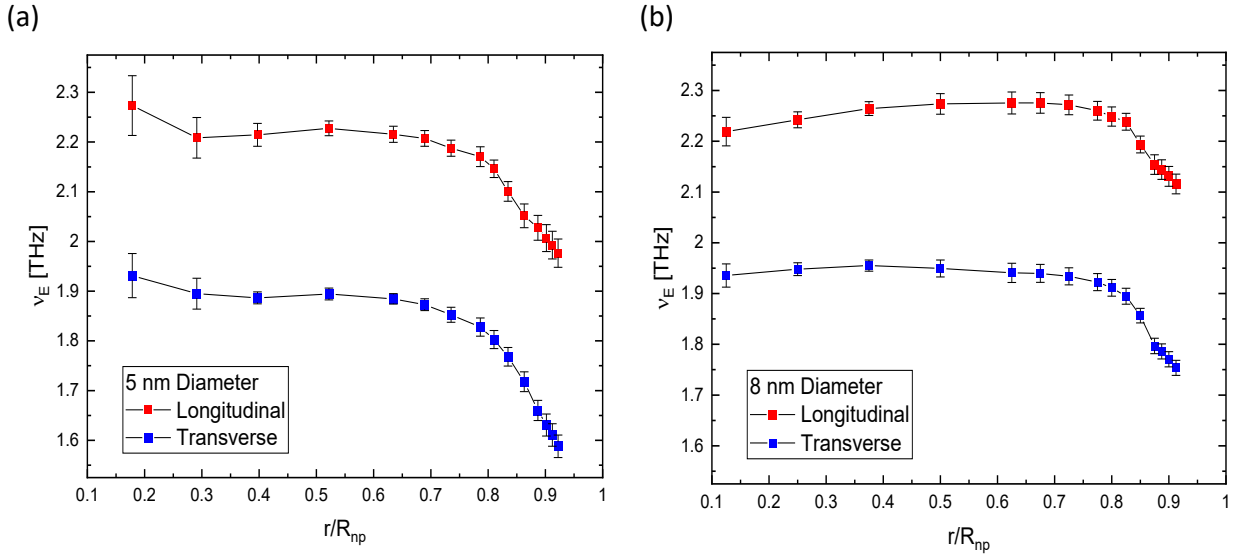


Figure 6.13: Einstein frequencies at different distances from the center (normalized by the nanoparticle radius R_{np}) in nanoparticles of diameter (a) 5nm and (b) 8nm

expected, the static disorder is mainly due to near-surface regions of the nanoparticles. However, also the $C_{2,dyn}$ displays a variation near the surface (Figure 6.12), which is a less trivial fact. Thus, the dynamical disorder quantities (MSRDs) was also investigated in this regard: the radial distributions of the Einstein frequencies (longitudinal and transverse), reported in Figure 6.13, indeed shows a variation near the surface of both the transversal and longitudinal MSRDs.

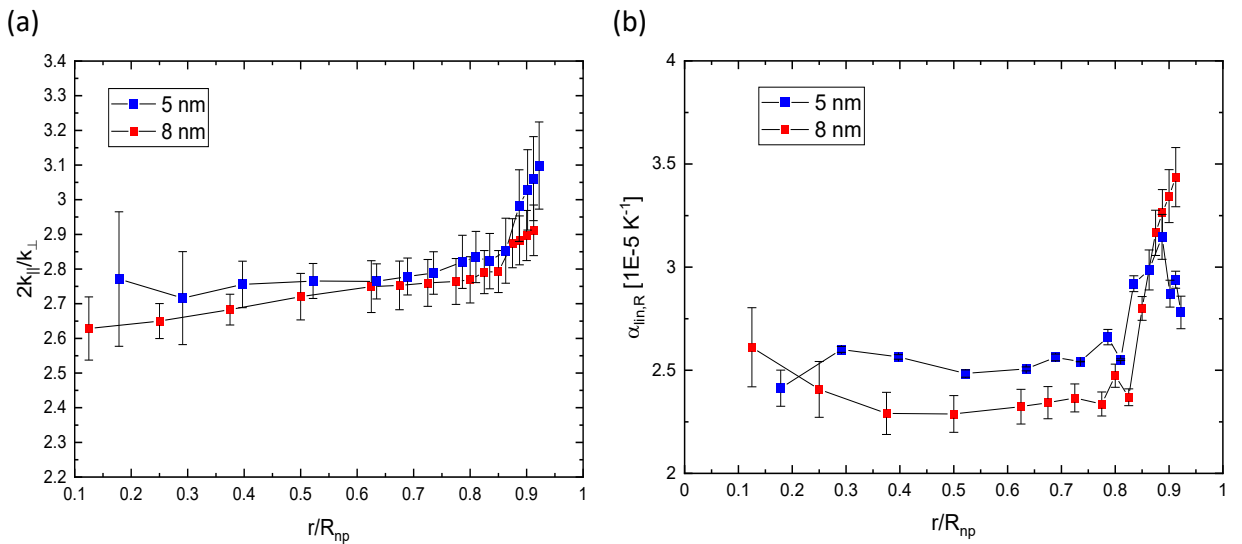


Figure 6.14: a) Anisotropy of thermal vibrations (estimated as double the ratio of longitudinal to transverse force constants) and b) thermal expansion linear coefficient as a function of distance from the center (normalized by the nanoparticle radius R_{np})

What is unclear at this point is if the vibrational anisotropy changes near the surface: as visible in Figure 6.14, where the radial dependence of the ratio of the longitudinal over transverse effective force constant is reported, the anisotropy increases near the surface with respect to the center.

6.5 Conclusions

Molecular dynamics simulations have been performed that, employing a simple embedded atom potential, give a semiquantitative description of the vibrational dynamics of spherical gold nanoparticles: being able to correctly understand how nanostructuring affects phonons is a crucial first step towards the description of anomalous thermal expansion in gold nanoparticles, which is complicated by the relevance of electronic thermal excitations (cf. Kubo gap in metallic nanoparticles).

The radial disaggregation of physical quantities offers a rich perspective on the interplay of phonon confinement, vibrational anisotropy and static disorder occurring in nanostructured materials: this powerful point of view, very hard to experimentally access, gives precious insights on the dynamics at the nanoscale. These numerical simulations indicate greater phononic contributions to the positive thermal expansion (CTE) in spherical gold nanoparticles than in the bulk form, especially in the regions near the surface.

Bibliography

- [1] J. G. Gale and A. L. Rohl, "The General Utility Lattice Program (GULP)," *Molecular Simulation*, vol. 29:5, pp. 291-341, 2003.
- [2] J. D. Gale, "GULP: A computer program for the symmetry-adapted simulation of solids," *J. Chem. Soc., Faraday Trans.*, vol. 93, pp. 629-637, 1997.
- [3] T. Yokoyama, "Path-integral effective-potential theory for EXAFS cumulants compared with the second-order perturbation," *J. Synchrotron Rad.*, vol. 6, pp. 323-325, 1999.
- [4] N. Abd el All and e. al., "Accuracy evaluation in temperature-dependent EXAFS measurements of CdTe," *J. Synchrotron Rad.*, vol. 20, pp. 603-613, 2012.
- [5] E. A. Stern and e. al., "Thermal vibration and melting from a local perspective," *Phys. Rev. B*, vol. 43, no. 11, 1991.
- [6] "J. Chem. Phys.," no. 81, p. 511, 1984.
- [7] A. Sutton and J. Chen, "Long-range Finnis-Sinclair potentials," *Phil. Mag. Lett.*, vol. 61:3, pp. 139-146, 1990.
- [8] M. G. Pamato and e. al., "The thermal expansion of gold: point defect concentrations and pre-melting in a face-centered cubic metal," *J. Appl. Cryst.*, vol. 51, pp. 470-480, 2018.
- [9] T. Comaschi and e. al., "Thermal dependent anharmonicity effects on gold bulk studied by extended x-ray-absorption fine structure," *J. Phys. Condens. Matter*, vol. 21, p. 325404, 2009.
- [10] R. Kubo, "Electronic Properties of Metallic Fine Particles. I.," *J. Phys. Soc. Jpn.*, vol. 17, pp. 975-986, 1962.
- [11] W. P. Halperin, "Quantum size effects in metal particles," *Reviews of Modern Physics*, vol. 58, no. 3, 1986.
- [12] W.-H. Li and e. al., "Thermal contraction of Au nanoparticles," *Phys. Rev. Lett.*, vol. 89, p. 135504, 2002.
- [13] T. Comaschi and e. al., "Temperature dependence of the structural parameters of gold nanoparticles investigated with EXAFS," *Phys. Rev. B*, vol. 77, p. 075432, 2008.
- [14] R. J. Needs and M. Mansfield, "Calculations of the surface stress tensor and surface energy of the (111) surfaces of iridium, platinum and gold," *J. Phys.: Condens. Matter*, vol. 1, p. 7555, 1989.
- [15] O. M. Roscioni and e. al., "Computational prediction of L₃ EXAFS spectra of gold nanoparticles from classical molecular dynamics simulations," *Phys. Rev. B*, vol. 83, p. 115409, 2011.
- [16] N. Van Hung and e. al., "Anharmonic correlated Debye model Debye–Waller factors," *Physica B: Condensed Matter*, vol. 405, no. 11, pp. 2519-2525, 2010.

- [17] A. I. Frenkel and J. J. Rehr, "Thermal expansion and x-ray-absorption fine-structure cumulants," *Phys. Rev. B*, vol. 48, no. 1, pp. 585-588, 1993.
- [18] F. D. Vila and e. al., "Theoretical x-ray absorption Debye-Waller factors," *Phys. Rev. B*, vol. 76, p. 014301, 2007.
- [19] O. L. Anderson and e. al., "Anharmonicity and the equation of state for gold," *J. Appl. Phys.*, vol. 65, p. 1534, 1989.
- [20] P. Fornasini and R. Grisenti, "On EXAFS Debye-Waller factor and recent advances," *J. Synchrotron Rad.*, vol. 22, pp. 1242-1257, 2015.
- [21] A. Quong, "First-principles determination of the interatomic-force-constant tensor of Au," *Phys. Rev. B*, vol. 49, no. 5, 1994.
- [22] N. Shi and e. al., "Negative thermal expansion in cubic FeFe(CN)₆ Prussian blue analogues," *Dalton Trans.*, vol. 48, pp. 3658-3663, 2019.
- [23] Q. Gao and e. al., "Effect of H₂O Molecules on Thermal Expansion of TiCo(CN)₆," *Inorg. Chem.*, vol. 59, no. 20, p. 14852–14855, 2020.
- [24] J. Chen, Q. Gao, A. Sanson and e. al., "Tunable thermal expansion in framework materials through redox intercalation," *Nat. Commun.*, vol. 8, p. 14441, 2017.

Conclusions

In this work the opportunities to tune the vibrational contribution to thermal expansion have been reviewed and explored from both the experimental and theoretical point of view.

The recent discovery of several classes of materials with widely varying coefficients of thermal expansion, from largely negative to positive encompassing the intermediate values, has sparked great interest. Technological applications could imply the reduction of shocks in components undergoing thermal processes and of the detrimental effect of temperature fluctuations on high precision instrumentation. The theoretical description of the microscopic mechanisms underlying anomalous thermal expansion is also challenging, due to the wide array of materials displaying it.

In light of these enticing premises, we proposed to establish experimental facts clarifying the phonon contributions to anomalous thermal expansion properties, particularly relevant in the case of framework structured materials, where it usually is the determining factor. We have presented the state-of-the-art of the matter and the classifications of anomalous thermal expansion materials, together with the corresponding (at least tentative) theories.

On the experimental side, the anisotropy of thermal vibrations of specific atomic pair has been measured combining EXAFS spectroscopy and diffraction techniques. The investigated samples have been prepared and provided by the research group of Prof. Jun Chen from the Department of Physical Chemistry, University of Science and Technology Beijing, which also studied the samples by diffraction techniques. The data collection was performed at the synchrotron light facilities ELETTRA (Italy), ESRF (France) and in minor part APS (United States of America, data acquired by the research group of Prof. Jun Chen).

EXAFS spectroscopy analysis has been presented for Prussian blue analogues (PBAs), zirconium-transition metals alloys and copper pyrophosphate analogues.

Intercalation of small chemical species into PBAs with brute formula $MM'(CN)_6$ has been shown to strongly hinder the negative thermal expansion, even turning it positive. In this work we studied the effect of water intercalation in $TiCo(CN)_6$.

The EXAFS sensitivity to atomic species allowed to independently study the dynamics in the local neighborhood of M and M' atoms, revealing that the intercalation strongly hinders the transverse thermal vibrations of M-N atomic pairs, while leaving those of the M'-C atomic pairs practically unscathed. This fact has an impact on the synthesis and search for new NTE materials in this class of

materials, which is now simplified by focusing on the choice of the M atomic specie, while the M' specie can be chosen to minimize costs or optimize other desirable properties. A wider perspective has also been elaborated on the PBAs, finding a negative correlation between the volumetric coefficient of thermal expansion and the ratio of effective force constants transverse and longitudinal, a quantity characterizing thermal vibrations of atomic pairs in a temperature independent manner. In this sense, $\text{LuFe}(\text{CN})_6$ has been investigated as an important member of the rare earths containing PBAs (with $M'=\text{Fe}$ and $M=\text{Lu, Ho, Y, Sm, La}$), the study of which has taken further the knowledge on the dependence of the NTE on the M atomic specie, bound to nitrogen.

Zirconium alloys with brute formula Zr_2M ($M=\text{Fe, Co, Ni}$) display a common body centered tetragonal crystal structure, allowing a meaningful and clear comparison among them. Thus, studying them has been the occasion to put to test emergent patterns in an unusual context of anisotropic thermal expansion. The main findings are the observation of negative correlation between anisotropy of Zr-M atomic pairs and the CTE along the c-axis, the validity of the average atomic volume even in this extreme case and the possibility to extend it as a relation between the value of the lattice parameter and the corresponding CTE to materials with highly anisotropic thermal expansion.

Large negative thermal expansion in a wide temperature range has been discovered in copper pyrophosphate ($\text{Cu}_2\text{P}_2\text{O}_7$), a compound facile and inexpensive to synthesize, thus very promising for applications. These substances display a rich variety of behaviors, which complicate the quest to unravel the underlying mechanism of their NTE. Thermal expansion and the crystal structure are strongly changed by substitution of copper with zinc and of phosphorus with vanadium; the latter allowed to study both Cu-O and V-O atomic pairs, revealing that the latter have a much higher vibrational anisotropy than the former, suggesting that they are more relevant in the determination of the NTE magnitude. The comparison of Cu-O pairs anisotropy with those of $\text{Cu}_2\text{P}_2\text{O}_7$ confirms once again the role of transverse thermal vibrations in NTE: transverse vibrations of Cu-O pairs are suppressed upon substitution of the phosphorus and/or the copper.

On the theoretical side, with the hope of clarifying the effect of nanostructuration on the phonon contribution to thermal expansion, classical molecular dynamics simulations of spherical gold nanoparticles of various diameters have been performed. The accuracy of the simulations was assessed by comparing their predictions to EXAFS and diffraction experimental data, finding an agreement level sufficient to ensure the correctness of the results at the semi-quantitative level. The thermal expansion coefficient was found to increase with decreasing nanoparticle size. To further investigate the matter, we have studied how the local dynamics of gold atomic pairs varies at

different distances from the center of the nanoparticle: the near surface section represents the source of the increased thermal expansion, also displaying a change in the dynamical thermal disorder and the anisotropy of thermal vibrations.

We can now look at the obtained results with a wider breadth of view. Consistently with early observations, negative correlation between anisotropy of thermal vibrations and the thermal expansion is established. However, it has also been clearly pointed out that different types of atomic pairs play a significantly different role in the NTE mechanism, some of them being practically inert. The average atomic volume has been confirmed as an important factor in determining the NTE, even if, in cases of strongly anisotropic thermal expansion, an evaluation also involving the lattice parameters yields valuable information.

Yet, several issues remain unclear and deserve future attention, for example a satisfactory theoretical justification for the observed relations between the average atomic volume (or more in general the lattice parameters or bond length), the coefficient of thermal expansion and anisotropy of thermal vibrations. More in general, the great interest and effort up to now seem to have opened a vast scientific field, since the variety and quantity of NTE materials, which not long ago seemed just a curiosity, grow rapidly as more is known about them and their promising applications. Having established important results on the phonon contribution to NTE and its control, this work finds its place in the quest for the smart search for new materials with tuned thermal expansion and their production.